A Computationally Efficient Online Optimal Charging Algorithm to Minimise Solid Electrolyte Interface Layer Growth in Lithium-ion Battery

Submitted in partial fulfillment of the requirements of the

Doctor of Philosophy

Muhammad Sajjad Sabir Malik

School of Engineering and Materials Science

Queen Mary University of London

United Kingdom

Statement of originality

I, Muhammad Sajjad Sabir Malik, confirm that the research included within this thesis is my own work or that where it has been carried out in collaboration with, or supported by others, that this is duly acknowledged below and my contribution indicated. Previously published material is also acknowledged below.
I attest that I have exercised reasonable care to ensure that the work is original, and does not to the best of my knowledge break any UK law, infringe any third party's copyright or other Intellectual Property Right, or contain any confidential material. I accept that the College has the right to use plagiarism detection software to check the electronic version of the thesis. I confirm that this thesis has not been previously submitted for the award of a degree by this or any other university. The copyright of this thesis rests with the author and no quotation from it or information derived from it may be published without the prior written consent of the author.

Signature:

Date: 27-07-2021

List of Publications

- Malik, M.S.S., Guang Li, and Zheng Chen. "An optimal charging algorithm to minimise solid electrolyte interface layer in lithium-ion battery." Journal of Power Sources 482 (2021): 228895.

Abstract

Lithium-ion batteries have emerged as major energy storage devices over the last few decades. For enhanced battery life, understanding the relevant degradation mechanisms and their control has been a significant area of research interest. The dissertation explores the state of health in lithium-ion batteries in terms of solid electrolyte interface layer growth. The proposed optimal strategy gives a quantitative approach to measure the interface layer. A novel non-linear model predictive control algorithm is devised for online optimal charging by explicitly incorporating degradation mechanisms into control to reduce the degradation process. Chemical and mechanical degradation mechanisms have been considered separately for the growth of the interface layer. The work addresses the challenge of minimising layer growth during charging using the first-order model in chemical degradation. However, the interface layer is modelled based on the break and repair effect in mechanical degradation. A single particle model is used for optimal charging using orthogonal projection-based model reformulation. Gauss pseudo-spectral method is used for the optimisation of charging trajectories. Results of the optimal algorithm are compared with the traditional constant current constant voltage approach without considering the interface layer growth. The aim of using different degradation concepts is to find similarities in charging patterns in lithium-ion batteries. Moreover, it is ensured that overpotential caused by lithium plating remains in a healthy regime considering chemical degradation, i.e. it must be positive during charging. Simulation results have been presented to demonstrate the advantages of the proposed charging method dealing with two side reactions simultaneously. The dissertation extends the results of the proposed non-linear model predictive control strategy considering chemical degradation in two ways. First, the single particle model with temperature dynamics was adopted to examine the thermal behaviour of lithium-ion batteries and temperature control. Second, the differential flatness method is applied to examine its computational benefits over pseudo-spectral methods. A brief discussion on implementing the proposed algorithm in a battery management system of electric vehicles is presented.

Contents

Dedicated to my father (M Sabir Malik), mother (Naseem Akhtar), sisters (Asma Sabir, Saba Sabir and Ayesha Sabir) and brother (M Ijaz Sabir Malik)

Acknowledgements

The completion of this study could not have been possible without the expertise of Dr Guang Li, my PhD advisor. He has been very patient throughout my journey.

I am also very thankful to my colleagues, Zhijing Liao, Qin Guo, Hudair Samad, Awais Yousuf and Dr Zheng Chen, for helping me whenever I faced pressure emotionally or theoretically.

I am forever grateful to my parents and siblings for truly believing in me. You are always available in the ups and downs of my PhD journey and never mind the long distance.

I would also like to thank the Queen Mary University of London to give me a platform for quality research to enhance my skills. Additionally, I am thankful to the Doctoral College team for their support and arranging events throughout the course, which has helped me develop my personality.

Last but not least, I would like to thank the Higher Education Commission (HEC), Pakistan, to sponsor me for my PhD studies. I try my best to be a valuable member of the academic society of Pakistan. My primary goal would be to transfer my knowledge and skills to young students of the country.

List of Figures

List of Tables

Nomenclature

List of Symbols

c	concentration ($mol\ m^{-3}$)
r	radius of electrode (m)
t	time (s)
J	molar flux ($A\ m^{-2}$)
F	Faraday's constant ($C\ mol^{-1}$)
D	Diffusion constant ($m^2 s^{-1}$)
a	interfacial surface area (m^{-1})
I	current (A)
S	area of electrode (m^2)
L	length of electrode (m)
T	temperature (°C)
i	current density (Am^{-2})
U	equilibrium potential (V)
V	voltage of cell (V)
M	molecular weight ($kg\ mol^{-1}$)
E	Young's Modulus
N	number of cycles
Cap	capacity
e	stress energy
EaD	activation energy of diffusion
Eak	activation energy of reaction rate
mC_p	thermal mass
T_r	relaxation voltage

Greek

ϵ porosity of electrode

α transfer coefficient

η overpotential

ϕ potential, Legendre polynomial

β time coefficient

δ thickness

ρ density of products

κ conductivity of electrolyte

ϵ_j strain (radial or tangential)

ν poisson's ratio

σ stress

Ω partial volume of solute

u displacement tensor

Subscripts/Superscripts

s	solid state
p	positive electrode
n	negative electrode
avg	average
max	maximum
$surf$	surface
a	anode
c	cathode
g	gas
1	solid
2	solution
$film$	SEI film
sr	side reaction
SEI	solid electrolyte interface
eq	equivalent
ref	reference
$ampl$	amplitude
min	minimum
$yield$	yield stress
cal	calendar
cyc	cyclic

Acronyms

NMPC	non-linear model predictive control
EV	electric vehicle
CCCV	constant current constant voltage
SOH	state of health
BMS	battery management system
NLP	non-linear programming
SPM	single particle model
SOC	state of charge
MPC	model predictive control
IAM	integration approximation matrix
DIS	diffusion-induced stress
SPM-T	single particle model with thermal dynamics
GPM	Gauss pseudo-spectral method
DOD	depth of discharge
EOCV	end of charge voltage
COV	cut-off voltage

Chapter 1

Introduction

1.1 Motivation of the work

The dissertation explores the estimations of the state of health of lithium-ion batteries using an online model-based control considering degradation mechanisms. The degradation mechanisms in lithium-ion batteries can be chemical or mechanical and should be accounted for while modelling the battery system [1]. Lithium-ion batteries are commonly used in a wide range of applications, such as electric vehicles, cheap and expensive electronic devices, and the smart grid [2]. These batteries are chosen over their competitors, lead-acid and nickel-metal hydride batteries, due to their high power and energy densities, low memory effects, and low self-discharge rates [3, 4]. However, capacity fade can be expected in lithium-ion batteries from inaccurate use and if proper safety procedures are not applied [5].

Moreover, a significant amount of work has done to understand capacity fade using experimental and numerical studies [6]-[14]. A comprehensive capacity fade analysis is carried out on Sony 18650 cells for hundred of cycles [6]. The proposed model divides the fade behaviour into primary and secondary material losses to better understand the concept [6]. However, the model lacks the quantification of capacity under different mechanisms. [7] presents a capacity fade model suggesting different stages in a lithium-ion battery, but the model lacks the degradation process. A prediction model based on a life test can easily estimate the capacity loss [8]. However, these models can be coupled with factors that influence the battery's ageing [9]. Researchers

have established a relationship of the capacity with one or a combination of factors, such as discharge rate and temperature versus capacity [10], the effect of current rates, working temperature, and depth of discharge (DOD) on capacity [11]. Also, the quantification of the battery capacity fade model has been done using capacity degradation in dynamic processes. However, researchers do not account for all factors that can influence a battery's life [6]-[11].

In contrast, at higher discharge rates, the effect of the depth of discharge (DOD) is more significant [12]. Battery life is estimated using the fatigue approach by taking a complex current profile and considering the growth of the SEI at the anode [13]. Many authors have formulated the capacity fade models using mechanical degradation alone, but a coupled chemical and mechanical degradation model has been developed by [7, 14] to predict the battery's life. In these models, the authors have considered all the possible effects that might influence the battery life [7, 14]. Moreover, batteries can undergo thermal runaway under abnormal environmental conditions. The Chevy Volt caught fire [15], and the Boeing 787 Dreamliner explosion [16] are two popular examples of thermal runaway accidents. It can initiate by localised heating and by overcharging the batteries [17]. The uncontrolled release of potential energy can easily cause a fire in the lithium-ion batteries [18]. One of the most common examples of unwanted initial energy release is short circuits inside a cell [19]. The components of batteries are toxic, so overheating can cause thermal runaway problems due to auto-catalytic reaction with the electrolytes [20, 21]. Therefore, battery manufacturers must take safety considerations to prevent high internal temperatures because of the low melting point of lithium [22].

A battery management system (BMS) is an integral part of lithium-ion battery applications to estimate and control internal states [23]. According to battery university, the purpose of a BMS is to "provide battery safety and longevity, reveal state-of-function in the form of state-of-charge and state-of-health, prompt caution and service and indicate end-of-life when the capacity falls below the user-set target threshold" [23]. The control part of a BMS is crucial as it is responsible for optimised charging without violating protocols of safety [24]. Control is a trade-off between minimising degradation mechanisms (optimised charging) and user demand (fast charging) [25].

The estimation of the state of charge (SOC) and other internal variables is the main functions of a BMS [24, 25]. A proper estimation algorithm (observer) is needed to accurately estimate the states of the battery as no internal states can be measured directly through the sensors [25].

A traditional BMS uses model-free control methodologies, which can not incorporate variables responsible for ageing [26]. The algorithm is unable to constrain the side reaction overpotentials of lithium-ion batteries, resulting in low performance. Overall, traditional BMSs restrict the battery's performance, cause safety risk, and unnecessarily increase the cost of the system [26]. However, it does not mean that traditional BMSs have no mechanism to avoid battery degradation, usually performed by imposing constraints on external variables such as voltage, current, and temperature [27]. All of these battery variables are externally measured and can not control the battery degradation solely [27]. Conventional control strategies are easy to use as they do not need a battery model or constraints, and the safety of battery application establishes the use of measured signals [28]. However, the literature shows that these conventional control methodologies are under-par for fresh batteries and over-par for used batteries [29]. A fresh battery can reach the voltage limit early during constant cell voltage bounds, but there is still a margin for safe operation. However, it is dangerous to use the same voltage bounds when the battery ages [29].

The primary reason is the inability of the aged electrodes to cope with dangerous side reactions within those bounds [28]. Apart from control, the estimation of states is another challenging issue for BMS engineers [31]. Coulomb counting is the most popular method for estimating the SOC in traditional BMSs [30]. Although it is simple to use and has a model-free algorithm, this method has serious disadvantages, which can lead to estimation errors [31]. An incorrect initial SOC, current sensor bias, and inaccurate capacity estimates are sources of estimation errors [32].

To overcome these challenges in traditional BMSs, battery packs are typically oversized to ensure optimal battery safety and life [33]. The battery packs' size directly links to the thermal management system (TMS) or cooling system for battery electrified vehicles [33]. The primary aim of cooling systems is to keep the batteries temperature in the prescribed range, but their size increases the cost of battery packs

[34]. Lithium-ion batteries perform in an operating range that dictates the size depending on the power and energy fade rate [33]. In modern electric vehicles, active and passive cooling systems are employed [34]. The traditional thermal management systems include Air cooling [35, 36], Liquid cooling [37, 38], Refrigerant cooling [39, 40], PCM cooling [41, 42], Heat pipe TMS [43, 44], and Thermo-electric coolers [45, 46]. Liquid cooling has the highest cooling efficiency than air cooling but increases the size of the battery pack [37, 38]. However, modern cooling system such as Hybrid cooling [47, 48], improved air cooling [49, 50], improved liquid cooling [51, 52] help to minimise the size of overall battery packs.

Model-based control is always preferred to the traditional model-free techniques due to the battery's performance, life longevity, and price [53]-[55]. It is possible to estimate internal battery variables that directly link to battery ageing mechanisms [53]. Two of the most crucial battery ageing mechanisms are solid electrolyte interface (SEI) layer growth and lithium plating, stifling the ion transfer between electrodes and electrolyte [53]. Battery life can be easily extended by 20-40% by using model-based control [54, 55]. It improves safety and energy storage capacity and decreases the degradation of batteries [54].

Moreover, batteries can easily be charged more quickly and safely by using model-based control because of their capability to adapt to variations [55]. An online BMS monitors, controls and optimises the performance of battery modules' performance [56]. The battery function does not limit to providing power to the wheels but also manages on-board power requirements such as sensing and communication [57]. The most important component of BMS is the power module [58]. The basic task of the module is to charge the battery and controls the battery charging [58, 59]. The battery pack is a part of BMS for energy storage and to power electric vehicles [57]-[66]. BMS should approach various battery systems differently using specialised charging algorithms [60, 61]. The DC/DC converter is needed to power the various system parts in high or low battery voltage [62, 63]. The load such as supply voltages, power consumption of system parts and other portable products need the power from the battery [57, 64]. The communication channel in a BMS monitors and controls the intra-processing of signals [65, 66]. The communication in BMS mostly works in a

master-slave architecture form where one central processing unit serves as a master control module, while every battery module is connected to a slave control module [67]. All slave control modules are connected to the main module, which makes decision considering all variables [67].

1.2 Aims and objectives

1.2.1 Aims of the thesis

The main aim of the thesis is to develop novel control algorithms for online charging of lithium-ion batteries by explicitly incorporating degradation mechanisms. Both chemical and mechanical degradation theories are considered separately to optimise the charging trajectory. The proposed algorithm is designed to charge the battery in electric vehicles. For this purpose, lithium iron phosphate (LFP) and lithium cobalt oxide (LCO) has been used. Both battery types are extensively used in electric vehicles. The following key items as learning objectives are studied from the literature and incorporated in the dissertation to achieve the goal.

1.2.2 Objective I: Dynamics of the battery

The dissertation uses a Legendre polynomial-based orthogonal projection technique to estimate the state of each electrode of the battery [68]. This model-order reformulation uses a smaller number of state equations [68]. The concentration of lithium ions in an electrode is represented as the sum of the Legendre spatial basis functions [69]. The dynamics of the battery electrode influenced by temperature are modelled by Chebyshev polynomials [70]. In both reformulation models, three state variables represent the dynamics of an electrode. Note that the mentioned reformulation models are not the only candidates to estimate battery dynamics; authors came up with other proposed methods, which will be discussed further.

1.2.3 Objective II: Pseudo-spectral methods

Pseudo-spectral methods are used to optimise the charging trajectory due to their high convergence rates [71]. Also, these methods are computationally efficient and can quickly solve non-linear, and non-convex optimisation problems [72, 73]. Pseudo-spectral methods are widely used to solve complex differential equations, but control engineers also adopted these to solve optimal control problems [73]. These methods rebuild an optimisation problem into non-linear programming (NLP) problem, which can further be solved using different algorithms [74].

1.2.4 Objective III: Chemical/Mechanical degradation

Chemical and mechanical degradation effects are studied in this work [75]. Irrespective of the type of degradation (chemical or mechanical), the work aims to minimise the growth of the SEI layer. Two schools of thought formulated SEI layer growth in their respective ways: (i) the SEI layer passively forms on the negative electrode due to the side reaction [75]. Due to the intercalation in a battery, volume of the anode increases. This volume change causes the surface film to break and exposes more carbon to the electrolyte solution [76]. This will act as a barrier for lithium-ion intercalation, leading to the capacity fade [76] and (ii) diffusion-induced stresses (DISs) that are produced during the charging/discharging of lithium-ion batteries due to the graphite expansion [77]. It is assumed that active material is not the weakest material (does not go in to plastic range in charging/discharging loads), but it is the SEI that breaks and repairs during cycling [78].

1.2.5 Objective IV: Differential flatness

The computational benefits of the differential flatness method are compared with the proposed non-linear model predictive control (NMPC) strategy [80]. A dynamic system is differentially flat if a state can be interpreted as a flat output [84]. Consequently, all remaining states and inputs are expressed in terms of flat output derivatives. Flatness is a form of controllability from linear to non-linear systems [84]. The differential flatness technique can easily solve optimisation, trajectory planning, and control de-

sign problems [85, 86].

A non-linear framework constitutes all of the above key items to solve an optimisation problem. It has two agendas: (i) to minimise the growth of the SEI layer considering the mechanical or chemical degradation mechanism and (ii) to run the lithium-ion batteries in a healthy regime (chemical degradation only). A non-linear model predictive control (MPC) algorithm is presented using an online receding-horizon approach.

1.3 Challenges

There are obvious benefits of model-based control and state estimation, but the computational cost and estimation accuracy are the critical challenges [54, 55]. MPC is used to improve the above mentioned problems [87]-[104]. MPC is not a specific algorithm, but an intuitive approach [87]. However, MPC stands alone among all of the constrained optimal control strategies due to two reason. 1) It can easily handle hard constraints [88]-[92]. 2) It can optimise various objectives functions based on different charging algorithms [93]-[98]. The former reason dictates that MPC can easily deal with constraints directly linked to the health of the batteries [88]-[98]. The later reason implies the inclusion of non-linear systems while optimisation [99]-[101]. At every sampling interval in an MPC-based algorithm, the optimisation process runs for a new charging trajectory, thus introducing some degree of robustness [102]. MPC takes the lead among different approaches due to its computational efficiency, particularly in model-based control methodologies [103, 104]. The designed/proposed MPC controller must guarantee the optimal solution without violating any constraints [104]. Moreover, it is recommended that optimisation must be completed in less time. This is quite challenging, due to the non-linearity of physics-based battery models and inaccurate state estimation.

Physics-based battery models are difficult to handle in real-time applications [118]. Model-based control might not be a computationally viable solution due to the high computational cost of physics-based battery models [121]. Model-based control must fulfil two criteria: (i) it can represent battery dynamics, and (ii) accurately estimates ageing in the battery [118]-[127]. There is a broad range of lithium-ion battery models

in the existing literature with different levels of veracity and complexity [105]-[112]. Equivalent circuit models (ECMs) are the first kind of battery models, which represent battery dynamics using resistors and capacitors [105]. The simple circuit models with different variations based on the number of elements deal with externally measured variables without any insight into diffusion dynamics [105]. These electrical models are computationally fast, but researchers aimed for electrochemical alternatives that depict a battery's internal configuration [106]-[109]. This leads to a well-known Doyle-Fuller-Newman (DFN) model [106, 107], which represents battery dynamics in full detail. The DFN model deals with each aspect of dynamics occurring in a particular electrode, across two electrodes, and between an electrolyte and an electrode [107].

One of the significant drawbacks of the DFN model is the low computational efficiency for implementation in control applications [108]. A pseudo-two dimensional (P2D) is another candidate with reasonable computational efficiency, accounted for solid-phase and solution-phase diffusion dynamics in the batteries [108]. Unlike the DFN model, the P2D model has two dimensions; diffusion is assumed to occur through the thickness of the electrode and the radius of each particle [109]. One-dimensional partial differential equations (PDEs) represent these diffusion processes. The P2D model is used widely by the control community, but it is not yet applicable for modern BMS [109], mainly due to computational issues.

Researchers came up with a battery model which does not consider electrolyte dynamics [110]-[112]. The model is known as the single particle model (SPM), which assumes that a battery electrode can be represented as a single spherical particle [110]. Electrolyte dynamics is a significant feature, which is an important parameter to estimate ageing in a battery [110, 111]. The SPM is further developed to extended single particle models (ESPMs) with a reasonable representation of electrolytic diffusion between two electrodes [111]. Both SPM and ESPM can be extended to consider the thermal aspects of battery dynamics, leading to the temperature-enhanced single particle model (SPM-T)[112].

All of the above battery models can be used for optimal control problems with some advantages and disadvantages. However, ECMs rule out because of their inability to

cope with internal variables of batteries [107]. The controller needs a physics-based model to explicitly incorporate the SEI layer growth and lithium plating effects by imposing constraints on the side reaction overpotentials. All of the mentioned electrochemical battery models represent diffusion dynamics via PDEs [106]-[112]. These equations make the models dimensionally infinite, leading to challenging model-based control in computation and complexity.

Model reformulation or discretising involves converting non-linear models to linear approximations with reasonable accuracy [113]. Likewise, lithium-ion battery models based on PDEs can be reformulated to the finite number of state variables [114]-[117]. In SPM, concentrations are dependent on time and spatial dimensions [110]. A finite difference or finite element methods can be used to discretise spatial dimensions, having a drawback of higher-order reformulated models [114]. Researchers also try to approximate lithium-ion concentration profiles using polynomials, e.g., parabolic and quadratic, but these are battery specific [115]. A finite volume approach works well even when model order is high; however, an orthogonal collocation of finite elements with reduced battery model states has shown better results with equal discretisation points [116]. An excellent spatial resolution approximation is recorded at low-order models using the residue grouping method [117].

Any of the mentioned model-reformulation techniques [113]-[117] can be an essential part of the optimal control problem because an accurate model with reasonable state estimation accuracy is necessary to optimise the charging process. These techniques convert the complex PDEs to known differential equations, reducing the overall computation time [114]-[117]. Model reformulation is a vital aspect of the work in the dissertation, as SPM and SPM-T do not give satisfactory results using the same polynomial. An accurate battery state model is the main pillar for optimisation and control applications, so model validation is also an important feature of this work.

Another reason why battery-related optimisation problems are challenging is that battery dynamics are non-linear [106]-[112]. In the SPM, molar flux rates in two electrodes are governed by the non-linear Butler-Volmer equation [118]. The electrodes reference potentials and overpotential equations relate non-linear solid and solution phases [118]. If temperature effects are considered (SPM-T), this adds to non-linearity

in terms of the battery's internal states and inputs [119]. The overall non-linearity and non-convexity of the control problems related to battery applications can make optimisation challenging even for low-order battery models [118, 119].

Battery charge/discharge trajectory problems are solved by researchers using different algorithms [120]-[127]. Dynamic programming is used for non-convex optimisation, but high computation time limits its use in online control problems [120]. A Genetic algorithm [121, 122], the reference governor method [123], and direct transcription [124, 125] are either computationally inefficient or have flaws when dealing with an online model-based control problem. For instance, the computational cost restricts the use of these algorithms in online control applications [97, 179]. Researchers also proposed pseudo-spectral methods [126] using orthogonal collocation to optimise battery charging trajectory [127]. A key feature of the dissertation is to extend already published works on optimal charging with ageing effects. This work does not give any information about stability or global control optimality. However, it explores the limitations of the different key items used in finding the optimal solution.

Inaccurate state estimation of battery models is another reason which makes model-based optimisation more challenging [128]-[145]. Battery life decreases due to the inaccurate estimation of internal states caused by accidental damage [128]. State estimation is crucial in the battery pack, where improper cell balancing violates safety protocols [129]. The internal state variables in a battery can not be measured directly, so an observer is needed to estimate it [137]. For instance, the accumulation of charge, an algebraic output of internal state variables, is a critical parameter in a battery [130]. SOC gives the information of charge accumulation in any battery at a specific time and is defined as the amount of charge available in the battery divided by maximum charge capacity [129, 130]. SOC, by far, is the most critical functional variable which needs to be estimated accurately [130]-[145]. Literature shows a significant amount of work done on estimating SOC [130]. Researchers pinpoint some of the factors that can affect SOC estimation accuracies like sensor noise, model mismatch, and inaccurate parameter estimation [131]. Open-loop and closed-loop algorithms are used to estimate SOC [132, 134]. Open-loop SOC estimation is not an appropriate candidate because of incorrect initial SOC, current sensor bias, and problems

in estimating the charging capacity of a cell [132]. Closed-loop algorithms typically deal with these sources of errors [133]-[145]. Luenberger filtering [133, 134], backstepping [135], recursive least squares estimation [136], Kalman filtering [137]-[143], and optimisation-based estimation [144, 145] are some examples of closed-loop estimation algorithms.

Although the literature on SOC estimation is quite mature for control problems, it is essential to validate the model with experimental data. The Legendre-based orthogonal projection technique is used to approximate the concentration of lithium ions. However, no analysis has been done on sensor noise, which can add disturbance to the system. The next goal is to validate the resulting optimal charging profiles experimentally. However, in this work, the use of the non-linear MPC framework gives insight into the growth of the SEI layer both in chemical and mechanical forms. Also, some works reported an empirical solution to estimate the SOC [146]. These results are fine for a specific battery but can not handle other battery dynamics.

1.4 Contributions

The main contribution is to develop a novel control algorithm for online optimal charging of lithium-ion batteries by explicitly incorporating degradation mechanisms into control, to reduce the degradation process. This work can be seen as an extension of published works on health-conscious NMPC of lithium-ion batteries [80, 283]. Moreover, a computational efficient approach has been used to compare the optimal algorithm with the pseudo-spectral method solely [86]. Following are the key contributions compared to already published research articles.

- This work minimises the SEI layer growth during charging.
- A quantitative approach to measure the growth of the SEI layer has been conducted.
- The proposed optimal framework deals with two side reactions simultaneously, i.e. SEI layer growth and lithium plating considering chemical degradation.

- To find similarities in charging patterns considering chemical and mechanical degradation concepts
- Computational complexity of the system has been analysed and minimised via the proposed algorithm.

1.5 Organisation of the dissertation

The dissertation uses the proposed NMPC framework to minimise the degradation effects (chemical and mechanical), incorporating a model-based control. The main contributions to the literature are as follows:

- Chapter 2 explains the modelling of battery dynamics in terms of a single particle. Model reformulation technique is also employed to reduce the number of states in the battery model. The SEI layer growth model has been discussed and modelled using chemical and mechanical degradation concepts separately. The purpose to considering separate degradation concepts is to find similarities in optimised charging scenario.
- Chapter 3 proposes a non-linear optimisation strategy for an optimal charging profile to minimise the growth of the SEI layer. This chapter uses Gauss pseudo-spectral optimisation and model reformulation for diffusion. The control problems are formulated for charging trajectory considering chemical and mechanical degradation theories.
- Chapter 4 presents results of the optimisation problems explained in Chapter 3. The optimal charging scenario considering chemical degradation are discussed in terms of the SEI layer growth, charging time, and maximum current upper bound. Computational efficiency is also recorded for proposed and benchmark methodologies. However, in mechanical degradation, it is assumed that battery life affects the SEI repair/break phenomenon rather than the failure of an active material of graphite at room temperature. The results are compared with already published data.

- Chapter 5 extends the results of the optimisation problem considering chemical degradation. The thermal SPM is used, considering the SEI layer growth and lithium plating. The NMPC strategy is the same as in Chapter 3 with additional temperature constraints and a temperature-controlled battery model. An optimal charging profile is proposed, which successfully minimises the SEI layer growth and operates the battery in a healthy regime. The differential flatness method is compared with the proposed NMPC strategy to examine the computational burden.

A summary is presented in Chapter 6, which concludes the dissertation.

Chapter 2

Physics-based Modelling for LiBs

2.1 Introduction

The control target of the dissertation is to reach the reference state of charge (SOC) with minimum SEI layer resistance. The battery operation in a healthy regime is another aspect of this chapter, i.e., to avoid lithium plating during the charging process. Physics-based constraints are employed on internal variables such as overpotential, along with voltage and current upper limits. This chapter presents the physics-based modelling for lithium-ion batteries (LiBs) and solid electrolyte interface (SEI) layer considering chemical and mechanical degradation concepts separately. As the work employees model-based charging method, the correct models for batteries and associated degradation mechanisms are necessary to optimise the charging trajectory.

Model-based charging algorithms are the first choice of BMS engineers nowadays to incorporate an equivalent circuit model (ECM) or electrochemical model [105]-[112]. The main objective is to optimise the battery's charging trajectory by controlling the polarisation voltage [147]. A suitable ECM method can be chosen for battery dynamics using a certain number of circuit elements [147, 148]. Temperature effects can be incorporated into ECM using the Fourier thermodynamics formula (ECM-T model) [148]. Researchers tried various optimisation problems with a range of objective functions [149]-[151]. The optimisation results show significant improvements in charging time and temperature rise with the objective function defined as the sum of these two variables [149]. Another optimisation problem is solved based on the ECM-T with an

objective function that minimises energy loss along with constraining charging time and other external variables [150]. Results show a significant increase in energy and power densities of lithium-ion batteries [150]. The researchers also tried to optimise the ageing of a battery with ECM-T models [151]. The objective function is the sum of charging time and capacity loss [151]. These optimisation results are not trustworthy as circuit models give no information about the internal variables of batteries. Regarding ECMs, there is no information about lithium intercalation/de-intercalation, potential change between electrodes, and other chemical reactions [152]-[155].

Due to the inability of ECMs to estimate internal variables, electrochemical models (EMs) are an obvious choice to deal with the ageing of lithium-ion batteries [149]-[151]. The single particle model (SPM)[152], extended single particle model (ESPM) [153], temperature-based SPM (SPM-T) [107], pseudo-two dimensional (P2D)[154], and Doyle-Fuller-Newman (DFN) [155] are some electrochemical models used for optimisation purposes. The choice of a particular EM is based solely on the computation time and accuracy of the estimated states [144, 145]. These EMs can differentiate internal chemical and physical parameters influenced by side reactions due to the fast charging [156, 157]. The heat generation during fast charging impacts the battery life due to charge transfer reactions, diffusion and migration of lithium ions in the electrolyte interfaces and electrodes [156]-[161]. Moreover, lithium plating [162]-[166] and mechanical pulverisation [167]-[174] can also increase degradation at fast charging. The main objective of an EM-based optimised charging method is to impose constraints on side reactions so that it effectively restricts the loss of lithium ions during battery cycling [175]. Different optimal charging strategies are presented with various objective functions. Charging time minimisation, along with imposing constraints on voltage, current, temperature, and side reaction overpotential, is one of the many optimisation problems used by researchers [176]. Non-linear model predictive control (NMPC) [177] and control vector parametrisation (CVP) [125] are used to optimise the charging trajectory. All of these EM-based optimisation strategies are ideal for the depiction of ageing of the lithium-ion batteries [178], but computational time is a real issue [179]. The differential flatness-based pseudo-spectral control method is also used to reduce the computational time [86].

There are many side reactions responsible for the degradation of batteries. The formation of the SEI layer [180] is by far the most influential factor in battery chemistry. A fresh battery undergoes the first charging cycle, forming an initial layer of SEI on the graphite (anode) surface [180]. The initially formed surface is mainly due to organic and inorganic decomposed products resulting from solvent reduction processes [180, 181]. The thickness of the SEI layer is an important parameter, though it can not be easily measured [180]-[190]. There are many theories on the composition of the SEI, which highly varies depending on the type of batteries. The thickness of the SEI increases during cycling at elevated temperatures [181]. The SEI behaves differently at lower or higher potentials, but more noticeable changes happen at elevated temperatures [182]. The transformation of the SEI and the reaction of active material or electrolyte with the SEI occurs at high temperatures [183]. Battery performance is profoundly affected by composition, thickness, morphology, and compactness of the SEI layer [184]. When the SEI layer successfully passivates the active material surface, self-discharge can occur [185]. It means one can easily link the shelf life of the battery to the SEI layer [185]. Although during cycling, a stable SEI layer is necessary to provide kinetic stability [188]. However, exfoliation of the graphite is a common feature that damages the formation of the SEI layer [186]. One of the main reasons for this desquamation of graphite is the intercalation of solvent molecules with lithium-ion, leading to the graphite's order [187]. However, apart from stable graphite electrode [188], the overpotential due to SEI layer formation influences the graphite exfoliation [189]. The passivation process of graphite electrodes in mixed electrolytes is affected due to local current density caused by these overpotentials [190].

The SEI layer is influenced by many factors which contribute to its properties [191]-[196]. Unfortunately, none of the factors independently identify the SEI layer's properties, quality, and efficiency [247]. It is always a functional approach to understand the formation of the SEI layer [191]-[193]. The SEI layer dominates the area between the active material and the electrolyte, acquiring the properties of both phases [191]. It is usually formed on the surface of negative active material influenced by the type of carbon [192]. Authors proved that irreversible charge loss due to SEI formation is directly proportional to the Brunauer–Emmett–Teller (BET) specific surface area of

the carbon [193]. Apart from the BET surface area, crystallographic structure and particle morphology also influence the SEI formation [194]. Surface defects and active sites can act as sources of solvent reduction [194, 195]. In general, the SEI is composed of both inorganic and organic products [195]. Inorganic products are mostly found on the edges of graphite particles, while organic products are deposited on the surface of graphene sheets [195]. Another critical factor, the crystallographic structure of carbon, should not be obliterated as exfoliation increases in the presence of highly ordered carbons [196]. Pretreatment of carbon in the form of reduction, oxidation, electroless plating, and thermal treatment is done to enhance the surface properties [196, 197]. Electrolyte composition is another factor that affects the formation of the SEI due to thermodynamic instability, and kinetic reactivity [197]. Various techniques are used to analyse the SEI, ranging from spectroscopy to microscopy, diffraction, and thermo-analysis [198]-[209]. X-ray photoelectron spectroscopy (XFS) [198], Auger electron microscopy(AES) [199], atomic force microscopy (AFM) [200], and scanning tunnelling microscopy (STM) [201] are used for SEI layer surface analysis. Scanning electron microscopy (SEM) [202] and transmission electron microscopy (TEM) [203] are used for image analysis of the SEI film. Fourier transform infrared spectroscopy (FTIR) [204], infrared absorption spectroscopy (IRAS) [205], and Raman [206] are some examples of vibration spectroscopies used to understand the composition of the SEI film. Differential scanning calorimetry (DSC) [207], accelerated rate calorimetry (ARC) [208], and temperature-programmed desorption (TPD) [209] are popular examples of thermo-analysis. However, in this work, we focus on modelling the SEI layer formation, which will be discussed further.

Another side reaction incorporated in this work is lithium plating. In a normal battery cyclic condition, lithium ions are reversible [210]-[213]. A part of the intercalated lithium ions is lost, mainly due to the reaction with the electrolyte [214]-[217]. Lithium plating is the side reaction that occurs on the surface of a negative electrode [210]. It affects the electrode by forming the metallic lithium pigments and mostly occurs at low temperatures, high charging currents, and a high SOC during charging [210, 211]. Lithium plating should be avoided because dendrites growing at the surface of the electrode penetrate into the separator, causing a short circuit [211]. Lithium plating

may cause the exothermic reactions of lithium metal with the electrolyte, which affects the thermal balance of the battery [211]. It can occur after prolonged cycling in the porous electrode due to clogging [210]-[212]. Physio-chemical models are useful to predict the behaviour of lithium plating [212]-[215]. Arora et al. [212] studied the lithium plating effect during overcharge and also extended the well-known DFN model with the side reaction on the negative electrode. This side reaction is incorporated in the Butler-Volmer equation [212]. One can easily investigate the lithium plating effects under different operating conditions and charging protocols [213]-[216]. Perkins et al. [213] used their reduced-order model to show the degradation effect in lithium-ion batteries. Hein and Latz [214] proved via simulations that lithium plating depends on the distribution of lithium particles in the electrode. Ge et al. added temperature effects in Aroroa's model [215]. Yang et al. [216] predicted the behaviour of the ageing model after prolonged cycling. The authors also presented the mathematical depiction of lithium plating and stripping by introducing the concentration-dependent Butler-Volmer equation [217]. The common aspect in the mentioned references [210]-[217] is that side reaction overpotential must be greater than zero to avoid lithium plating. In this work, lithium plating must be avoided during charging along with minimising the thickness of the SEI layer.

Chemical and mechanical approaches separately give insight into the degradation of lithium-ion batteries, resulting in the capacity fade [75]. In contrast to chemical degradation, mechanical degradation mechanisms are linked to the changes in volumes and generation of stresses due to the repetitive intercalation of lithium ions in the active material [218]-[226]. In the thesis, the control problem employs the SEI layer growth from the mechanical degradation concept, considering the SEI layer as a weaker material (can go into the plastic region) compared to an active material [78]. Thus, the SEI layer breaks and repairs during the intercalation/de-intercalation of lithium ions [78]. The main aim of introducing mechanical degradation is to investigate the optimisation of the charging trajectory of the lithium-ion batteries separately from chemical degradation and find the similarities.

The oxidation of metals, hydrogen transport, and lithium diffusion are reasons for compositional non-uniformity in different mediums, ultimately generating diffusion-

induced stresses (DISs) [218]. Several authors have introduced modelling strategies to depict the behaviour of DISs [219]-[226]. During the mass transfer, the relationship between thermal stress and DIS is discussed by Prussin et al. [219]. Li [220] presents the analytical solution of the DIS phenomenon considering different geometries. A detailed study on the behaviour of DIS in thin plates, hollow cylinders, and composites is presented by Lee et al. [221]. Yang and Li [222] investigate the effect of DISs on the beam bending in sensing applications. Many researchers published articles addressing the modelling of lithium-ion batteries regarding electrochemical energy storage [223, 224]. The main areas of focus are kinetics and transport phenomena that govern the electrochemical behaviour of the system [225, 226]. Garcia et al. examine the generation of stresses during the diffusion of lithium under constant current control [223]. The same authors also explore linear sweep voltammetry along with heat generation effect on the single particle model (SPM) [224]. Most of these investigations are carried out on spherical and ellipsoidal particles [225]. Zhang et al. present the analysis of lithium-ion intercalation in the SPM [226].

It is believed in the battery research community that mechanical degradation can be chosen as a critical element to depict the insight of cyclic ageing of lithium-ion batteries [227, 228]. The DISs principle gives some information about cyclic ageing and factors affecting the battery's parameters [229, 230]. Christensen derive a formulation for particle fracture in anode and cathode particles [227]. According to the author's investigation, there is a direct relationship between maximum stress and c-rate [229]. Later on, researchers also investigated DIS phenomena in porous electrodes [228]-[230]. The DISs can be affected by the particle size [228], phase changes [229], and variable Young modulus [230]. Apart from DIS phenomena alone, several works have been carried out that merge the DIS with the fatigue theory [231]. The new modelling approach, which links DIS and fatigue, is a better depiction of the capacity fade during cycling [232]. This model does not consider the fracture of the SEI layer [232]. However, particle fracture has not happened quickly unless the battery operates at severe temperatures, i.e., below zero [232]. Hence, in normal conditions, it might be the SEI which fractures during intercalation/de-intercalation [232]. The electrolyte solution penetrates through the cracks of a particle, reproducing the SEI

layer and increasing the thickness [231, 232]. Due to the non-homogeneous nature of the SEI layer, it is safe to assume that the chances of fracture in the SEI layer are far higher than in graphite [228][232]. Purewal et al. [233] present the model showing the effects of the SEI layer with slightly different mechanical properties than of the graphite material. However, stresses on active material and the SEI layer must be investigated separately [78].

The remainder of this chapter is structured as follows. Section 2.2 presents the governing equations and model reformulation for the SPM. Section 2.3 gives the mathematical description of the formation and growth of the SEI layer considering chemical degradation. Section 2.4 presents the modelling of mechanical degradation concept, in which Subsection 2.4.1 demonstrates the analytical model of SEI and active particle. Subsections 2.4.2 and 2.4.3 discuss the fatigue and capacity loss as a result of SEI propagation.

2.2 Single particle model

Model-based control needs a model which represents the dynamics of lithium-ion batteries [53]-[67]. ECM, SPM, ESPM, P2D and DFN are commonly used lithium-ion battery models in the literature [105]-[112]. In the dissertation, SPM is used primarily to accomplish a trade-off between accuracy and computational efficiency [110]-[112]. In this section, the governing equations and assumptions of the SPM are briefly described [234]. The conversion of partial differential equations (PDEs) into ordinary differential equations using model order reduction techniques is also part of this section [69]. The battery used in this chapter is the A123 LFP 26650 2.3 Ah cell, where battery parameters and reference potential curve are obtained from [235]. It is assumed that the concentration of electrolyte c_e is constant, both in space and time domains [234]. A single lumped resistance can be represented for ohmic losses in both solid and electrolyte phases. Moreover, charge across the thickness of each electrode is distributed uniformly, which justifies the approximation of an electrode as a single spherical particle [234].

2.2.1 Governing equations

SPM's central equation is solid-phase diffusion dynamics, represented by Fick's second law of diffusion. The governing differential equation, considering time and radius as an independent variable, with boundary conditions at centre and particle surface are as follows:

$$\frac{\partial c_{s,i}(r,t)}{\partial r} = \frac{D_{s,i}}{r^2}\frac{\partial}{\partial r}\left(r^2\frac{\partial c_{s,i}(r,t)}{\partial r}\right) \tag{2.1}$$

$$\frac{\partial c_i(r,t)}{\partial r}|_{r=0} = 0 \tag{2.2}$$

$$\frac{\partial c_i(r,t)}{\partial r}|_{r=R} = \pm\frac{J_i(t)}{FD_{s,i}a_i} \tag{2.3}$$

where $c_{s,i}$, $D_{s,i}$, a_i and J_i are the solid state concentration, diffusion constant, inter-facial surface area and molar flux of lithium ions of corresponding electrode (negative or positive) respectively. F is Faraday constant, $i = p$ and $i = n$ correspond to positive and negative electrodes respectively. Inter-facial area of electrode can be defined as:

$$a_i = \frac{3\epsilon_i}{R_i} \tag{2.4}$$

R_i is the particle radius and ϵ_i is active volume fraction of material. The molar flux of lithium ions J_i is defined as:

$$J_n(t) = -\frac{I(t)}{S_n L_n} \tag{2.5}$$

$$J_p(t) = \frac{I(t)}{S_p L_p} \tag{2.6}$$

where I is the input current , + for charging, S_i is the sheet area of electrode i and L_i is the thickness of the corresponding electrode respectively. The bulk SOC is defined as:

$$SOC_i(t) = \frac{c_{s,i,avg}(t)}{c_{s,i,max}} \tag{2.7}$$

where $c_{s,i,avg}(t)$ is the average lithium-ion concentration of the electrode and $c_{s,max}$ is the maximum concentration of lithium ions of electrode. Average lithium ions

concentration of the electrode is represented as:

$$c_{s,i,avg}(t) = \int_0^{R_i} c_{s,i}\ dr \tag{2.8}$$

The surface SOC is defined as:

$$SOC_i^{surf}(t) = \frac{c_{s,i}^{surf}(t)}{c_{s,i,max}} \tag{2.9}$$

where $c_{s,i}^{surf}(t) = c_{s,i}(R_i, t)$ is the surface lithium-ion concentration of electrode. Battery SOC, SOC_{cell}, is defined as:

$$SOC_{cell} = \frac{SOC_n(t) - \theta_{n,0}}{\theta_{n,100} - \theta_{n,0}} \tag{2.10}$$

$$SOC_{cell} = \frac{\theta_{p,0} - SOC_p(t)}{\theta_{p,100} - \theta_{p,0}} \tag{2.11}$$

where the stoichiometry values $\theta_{i,0}$ and $\theta_{i,100}$ are defined as follow

$$\theta_{i,0} = \frac{c_{s,i,avg,0\%}(t)}{c_{s,i,max}} \tag{2.12}$$

$$\theta_{i,100} = \frac{c_{s,i,avg,100\%}(t)}{c_{s,i,max}} \tag{2.13}$$

where $c_{s,i,avg,0\%}(t)$, $c_{s,i,avg,100\%}(t)$ are the minimum and maximum average concentration of electrode i respectively. The relationship between molar flux of lithium ions and the potential difference between the solid and solution phases using Butler-Volmer equation.

$$J_i(t) = i_{0,i}(t)\left[exp\left(\frac{\alpha_a F}{RT}\eta_i(t)\right) - exp\left(\frac{\alpha_c F}{RT}\eta_i(t)\right)\right] \tag{2.14}$$

$$i_{0,i}(t) = a_i k_i (c_{s,i,max} - c_{s,i}^{surf})^{\alpha_a}\ (c_{s,i}^{surf(t)})^{\alpha_c}\ c_e^{\alpha_a} \tag{2.15}$$

k_i is reaction rate constant and $i_{0,i}$ is current density of the respective electrode. α_a and α_c are electrode transfer coefficients in anode and cathode respectively. $c_{s,max}$ and c_s^{surf} are maximum and surface concentrations in electrode. R is gas constant,

while T is temperature which is 298 K unless otherwise stated. The overpotential η_i is defined as difference between solid and electrolyte potential and it can be expressed for negative electrode as follows:

$$\eta_i(t) = \phi_{1,i}(t) - \phi_{2,i}(t) - U_i(t) \tag{2.16}$$

where $\phi_{1,i}$ is the solid phase potential, $\phi_{2,i}$ is the solution phase potential, and U_i is open circuit potential of the electrode. The potential drop in the solution phase between two electrodes is

$$\phi_{2,p}(t) - \phi_{2,n}(t) = I(t)R_{cell} \tag{2.17}$$

where R_{cell} is a lumped parameter to define resistance in the cell. The potential difference between positive and negative electrodes is defined as cell voltage. It can be expressed as:

$$V_{cell}(t) = \eta_p - \eta_n + U_p - U_n + I(t)R_{cell} \tag{2.18}$$

In this chapter, while optimisation of charging, side reaction is considered which represents lithium plating. This side reaction affects the negative electrode while charging. The overpotential due to side reaction can be written as follows [212] :

$$\eta_{sr} = \eta_n + U_n \tag{2.19}$$

where η_{sr} is the side reaction overpotential and it must be greater than or equal to zero for healthy operation of lithium-ion batteries [236, 237].

2.2.2 Model reformulation

Time-scale separation of SPM is employed in the dissertation for efficient optimisation. The dynamics of a negative electrode, which has slower dynamics, is represented by Fick's law, while a pure integrator is used to define the dynamics of the positive electrode. In this regard, differential equation (2.1) and boundary conditions (2.2) are considered only for the negative electrode. The law of conservation of lithium

ions is used to recover the concentration of the positive electrode. The total number of state variables reduces to half without lacking accuracy .

Fick's law of diffusion (2.1) is a PDE and difficult to solve mathematically. A model-reformulation process is needed to convert it into an ordinary differential equation. This model-reduction is achieved by using the Galerkin method, as presented by Kehs et al. [69]. Legendre polynomials are used as basis functions to represent spatial dynamics. Diffusion dynamics are computed by using only three state variables. The detail on the implementation of Legendre polynomials and orthogonal projection can be found in [238].

The lithium-ion concentration in the negative electrode $c_n(r,t)$ can be approximated by a linear combination of Legendre polynomials, separately defines the time and spatial dynamics:

$$c_n(r,t) \approx \phi_0(r)\beta_{0,n}(t) + \phi_2(r)\beta_{2,n}(t) + \phi_4(r)\beta_{4,n}(t) + \phi_6(r)\beta_{6,n}(t) \tag{2.20}$$

where $\phi_i(r)$ are even Legendre polynomials and $\beta_{i,n}(t)$ represents the time dynamics of negative electrode. The differential of even polynomials at collocation point is zero, thus satisfying the boundary condition at center of particle. The Legendre polynomials can be normalised [74]

$$\int_0^{R_n} \phi_i(r)\phi_j(r)dr = \begin{cases} 0 & \text{if} \quad i \neq j \\ 1 & \text{if} \quad i = j \end{cases}$$

where R_n is the radius of particle. Substituting (2.20) into eq. (2.1), gives

$$\sum_{i=0}^{4} \phi_i(r)\dot{\beta_{i,n}} = D_s \left[\frac{2}{r} \sum_{i=0}^{4} \frac{d\phi_i(r)}{dr} \beta_{i,n}(t) + \sum_{i=0}^{4} \frac{d^2\phi_i(r)}{dr^2} \beta_{i,n}((t) \right] \tag{2.21}$$

where $\dot{\beta}_i$ is differentiation of β_i with respect to time. Orthogonal projection techniques is used further by multiplying both sides of (2.21) by $[\phi_0, \phi_2, \phi_4, \phi_6]^T$ and then integrating both sides from 0 to R. The diffusion dynamics (2.1) can then be expressed

as the following:

$$\begin{bmatrix} \dot{\beta_0}(t) \\ \dot{\beta_2}(t) \\ \dot{\beta_4}(t) \\ \dot{\beta_6}(t) \end{bmatrix} = \frac{D_{s,n}}{R_n^2} \begin{bmatrix} 0 & 9\sqrt{5} & 20 & 29.4\sqrt{13} \\ 0 & 0 & 35\sqrt{5} & 16.8\sqrt{65} \\ 0 & 0 & 0 & 46.2\sqrt{13} \\ 0 & 0 & 0 & 0 \end{bmatrix} \begin{bmatrix} \beta_0(t) \\ \beta_2(t) \\ \beta_4(t) \\ \beta_6(t) \end{bmatrix} \tag{2.22}$$

Similarly the boundary condition in (2.2) can be expressed as:

$$\frac{3}{R}\sqrt{\frac{5}{R}}\beta_2 + \frac{10}{R}\sqrt{\frac{9}{R}}\beta_4 + \frac{21}{R}\sqrt{\frac{13}{R}}\beta_6 = -\frac{J_n(t)}{D_s a F} \tag{2.23}$$

Putting the value of J_n in (2.23), we get

$$\frac{3}{R}\sqrt{\frac{5}{R}}\beta_2 + \frac{10}{R}\sqrt{\frac{9}{R}}\beta_4 + \frac{21}{R}\sqrt{\frac{13}{R}}\beta_6 = -\frac{I(t)}{S_n L_n D_s a F} \tag{2.24}$$

β_6 does not have dynamics (2.22), and thus can be discarded. Hence, dynamics of a negative electrode can be expressed as a function of $\beta_{0,n}$, $\beta_{2,n}$ and $\beta_{4,n}$. The final dynamics of negative electrode is derived in the form of state space model using (2.22) and (2.24).

$$\dot{x}_n = A_n x_n + B_n u \tag{2.25}$$

where $x = [\beta_{0_n}, \beta_{2_n}, \beta_{4,n}]^T$ and input u is the current I. Any other variables like $\beta_{6,n}$, the electrode surface concentration $c_n^{surf}(r,t)$, can be computed algebraically from the solution of state space model (2.25).

2.3 Modelling of the SEI layer in chemical degradation

In the chemical degradation concept, the first-principles capacity fade model for lithium-ion batteries has been used [239]. Darling et al. were the first researchers who modelled the parasitic reactions by considering the solvent oxidation side reaction [239]. An analytical approach to quantify reversible and irreversible capacity loss

was developed by Spotnitz et al. [240] though the model does not handle the temperature changes successfully. Any side reaction in lithium-ion batteries leads to capacity loss [239, 240]. Researchers also model side reactions considering the composition of the electrolyte solution [241], the semi-empirical capacity fade model [242], and the solvent diffusion model under storage [243].

The model used in this chapter has some assumptions [244]: (i) ethylene carbonate is assumed to be an electrolyte; (ii) it is assumed that a solvent reduction reaction occurs only in charging; (iii) due to the side reaction on the surface of the active material, the product can be of any form, organic and inorganic or both; (iv) an irreversible side reaction is assumed with an open-circuit voltage of 0.4 V [244]; (v) the initial SEI layer resistance is taken as 100 $\Omega\ cm^2$; and (vi) any other side reaction such as lithium deposition is not considered. In contrast to the SPM model described in Section 2.2, certain changes in the negative electrode are proposed. Firstly equivalent molar flux at the negative electrode is equal to intercalation (J_n) plus side reaction (J_s).

$$J_{eq,n} = J_n + J_s \tag{2.26}$$

Moreover the equation of overpotential (2.16) is expressed by

$$\eta_n = \phi_{1,n} - \phi_{2,n} - U_n - \frac{J_{eq,n}}{a_n} R_{film} \tag{2.27}$$

where R_{film} is the resistance of the SEI film. Side reaction molar flux can be expressed as

$$J_s = -i_{o,s} a_n e^{-\frac{R_g T \eta_s}{2F}} \tag{2.28}$$

where $i_{o,s}$ is exchange current density for side reaction and η_s is side reaction overpotential which is represented as

$$\eta_s = \phi_{1,n} - \phi_{2,n} - U_{ref,s} - \frac{J_{eq,n}}{a_n} R_{film} \tag{2.29}$$

where $U_{ref,s}$ is open circuit potential for side reaction and is equal to 0.4 V [245]. For the first cycle, film resistance, R_{film}, is defined as

$$R_{film} = R_{SEI} + R_p(t) \tag{2.30}$$

where R_{SEI} is initial film resistance, 0.01 Ωm^2 in this work, while $R_p(t)$ is the resistance of the products formed during charging and is defined as

$$R_p(t) = \frac{\delta_{film}}{\kappa_p} \tag{2.31}$$

where κ_p is the conductivity of electrolyte. The mathematical expression of rate of SEI film resistance (δ_{film}) is written as

$$\frac{\partial \delta_{film}}{\partial t} = -\frac{J_s M_p}{a_n \rho_p F} \tag{2.32}$$

where M_p, ρ_p are molecular weight and density of products formed during side reaction respectively. From (2.30)-(2.32), time rate change of SEI film resistance is written as

$$\frac{\partial R_{film}}{\partial t} = \frac{i_{o,s} M_p}{\kappa_p \rho_p F} e^{-\frac{R_g T \eta_s}{2F}} \tag{2.33}$$

The equation (2.33) represents the dynamics of SEI film growth.

2.4 Mechanical degradation modelling

2.4.1 Analytical model of SEI and active particle

The SEI layer is a porous material formed due to the irreversible dissolution of the electrolyte with active materials of the electrode [246, 247]. However, the exact configuration of the SEI layer is not entirely explicable agreement on non-homogeneous nature [246]. During intercalation and de-intercalation of the lithium ions, the active material particle is surrounded by a thick layer of SEI due to a volume change [247]. The cycle life of the lithium-ion batteries can be reduced due to continuous expansion and compression of the material [247, 248]. The stresses generated due to charg-

ing/discharging are known as diffusion-induced stresses (DISs), which are thoroughly explained in [248]. The stress and strain for an elastic spherical body can be related by following mathematical expressions [249].

$$\epsilon_r = \frac{1}{E}\Big[(1+\nu)\sigma_r - \nu\sigma_t\Big] + \frac{c\Omega}{3} \tag{2.34}$$

$$\epsilon_t = \frac{1}{E}\Big[(1+\nu)\sigma_t - \nu\sigma_r\Big] + \frac{c\Omega}{3} \tag{2.35}$$

where ϵ_r and σ_r are the stress and strain in radial direction, while ϵ_t and σ_t are tangential strain and stress, respectively, E is the young modulus, ν is the poisson's ratio, c denotes active material particle concentration and Ω is the partial volume of solute in the solid material. It is assumed that elastic properties do not change with lithium concentration and also no external forces act on the particle. It means stress tensor can be defined by evaluating the following equilibrium equation [250].

$$\frac{d\sigma}{dr} + \frac{2(\sigma_r - \sigma_t}{r} = 0 \tag{2.36}$$

Both stress and displacement tensor is related by the following equations.

$$\epsilon_r = \frac{du}{dr}, \quad \epsilon_t = \frac{u}{r} \tag{2.37}$$

Substituting (2.37) in to (2.34) and (2.35) and replacing σ_r, σ_t in (2.36), gives the following second order differential equation [224].

$$\frac{d^2u}{dr^2} + \frac{2}{r} - 2\frac{u}{r^2} = \frac{1+\nu}{1-\nu}\frac{\Omega}{3}\frac{dc}{dr} \tag{2.38}$$

The analytical solutions for the above differential equation in particle and SEI are as follows [78]:

$$u_P(r) = \frac{(1+\nu_P)}{(1-\nu_P)}\frac{\Omega_P}{3}\frac{1}{r^2}\int_0^r C_P\, r^2 dr + a_P\, r + \frac{b_P}{r^2} \tag{2.39}$$

$$u_{SEI}(r) = \frac{(1+\nu_{SEI})}{(1-\nu_{SEI})}\frac{\Omega_{SEI}}{3}\frac{1}{r^2}\int_0^r C_{SEI}\, r^2 dr + a_{SEI}\, r + \frac{b_{SEI}}{r^2} \tag{2.40}$$

where sub-index P stands for active particle. Integration constants a_P, b_P, a_{SEI} and b_{SEI} are computed using boundary conditions. The final mathematical expressions for stresses in active material and SEI layer are as follows [78]

$$\sigma_{rP}(r) = -\frac{2\Omega_P E_P}{3(1-\nu_P))}\frac{1}{r^3}\int_0^r C_P\, r^2 dr + \frac{E_P}{(1-2\nu_P)}a_P - \frac{2}{r^3}\frac{E_P}{(1+\nu_P)}b_P \tag{2.41}$$

$$\sigma_{tP}(r) = -\frac{\Omega_P E_P}{3(1-\nu_P))}\frac{1}{r^3}\int_0^r C_P\, r^2 dr + \frac{E_P}{(1-2\nu_P)}a_P - \frac{1}{r^3}\frac{E_P}{(1+\nu_P)}b_P - \frac{\Omega_P E_P C_P}{3(1-\nu_P)} \tag{2.42}$$

where σ_{rP} and σ_{tP} are radial and tangential stresses in the active particle respectively. it is assumed that there is no expansion in the SEI layer due to charging and discharging. It means the first terms of (2.41) and (2.42) are zero, formulating the final form of stress in SEI as follows.

$$\sigma_{r,SEI}(r) = \frac{E_{SEI}}{(1-2\nu_{SEI})}a_{SEI} - \frac{2}{r^3}\frac{E_{SEI}}{(1+\nu_{SEI})}b_{SEI} \tag{2.43}$$

$$\sigma_{t,SEI}(r) = \frac{E_{SEI}}{(1-2\nu_{SEI})}a_{SEI} - \frac{1}{r^3}\frac{E_{SEI}}{(1+\nu_{SEI})}b_{SEI} - \frac{\Omega_{SEI}E_{SEI}C_P}{3(1-\nu_{SEI})} \tag{2.44}$$

The boundary conditions must be applied to find the integration constants. These are as under:

$$u_P(r=0) = 0, \;\; \sigma_{r,SEI}(r=R_{SEI}) = 0, \tag{2.45}$$

$$u_P(r=R_P) = u_{SEI}(r=R_P), \;\; \sigma_{rP}(r=R_P) = \sigma_{r,SEI}(r=R_P) \tag{2.46}$$

Putting $u_P(r=0)=0$ in (2.39)gives $b_P = 0$. For $\sigma_{r,SEI}(r=R_{SEI})=0$, (2.43) becomes:

$$\frac{a_{SEI}}{1-2\nu_{SEI}} - \frac{2}{R_{SEI}^3}\frac{b_{SEI}}{(1+\nu_{SEI})} = 0 \tag{2.47}$$

The displacement must be continuous for active and SEI materials. Applying boundary condition gives:

$$u_P(r = R_P) = u_{SEI}(r = R_P) \tag{2.48}$$

$$a_P\ R_P - a_{SEI}\ R_P - \frac{b_{SEI}}{R_P^2} = -\frac{(1+\nu_P)}{(1-\nu_P)}\frac{\Omega_P}{3}\frac{1}{R_P^2}\int_0^{R_P} C_P\ r^2 dr \tag{2.49}$$

Finally radial stresses in active particle and SEI must be continuous throughout the boundary. It means equating $\sigma_{rP}(r = R_P) = \sigma_{r,SEI}(r = R_P)$, gives:

$$\frac{E_{SEI}}{1-2\nu_{SEI}}a_{SEI} - \frac{2}{R_P^3}\frac{E_{SEI}}{(1+\nu_{SEI})}b_{SEI} = -\frac{2\Omega_P E_P}{3(1-\nu_P))}\frac{1}{R_P^3}\int_0^{R_P} C_P\ r^2 dr + \frac{E_P}{(1-2\nu_P)}a_P \tag{2.50}$$

A set of linear equations are formulated comprising of (2.47)-(2.50). Introducing constants $a_1 = \frac{1}{(1-2\nu_{SEI})}$, $a_2 = \frac{E_p}{(1-2\nu_P)}$, $a_3 = \frac{E_{SEI}}{(1-2\nu_{SEI})}$, $a_4 = \frac{2E_{SEI}}{R_P^3(1+\nu_{SEI})}$, $a_5 = -\frac{(1+\nu_P)}{(1-\nu_P)}\frac{\Omega_P}{3}\frac{1}{R_P^2}$, $a_6 = -\frac{2\Omega_P E_P}{3(1-\nu_P))}\frac{1}{R_P^3}$ and $b_1 = \frac{2}{R_{SEI}^3(1+\nu_{SEI})}$. Using given constants, integration constants can be computed as:

$$b_{SEI} = \frac{C_2}{C_1}\int_0^{R_P} C_P\ r^2 dr \tag{2.51}$$

$$a_{SEI} = C_3\int_0^{R_P} C_P\ r^2 dr \tag{2.52}$$

$$a_P = C_4\int_0^{R_P} C_P\ r^2 dr \tag{2.53}$$

whereas $C_1 = \frac{a_3 b_1 R_P^3 - a_1 a_4 R_P^3 - a_2 b_1 R_P^3 - a_2}{a_1 R_P^3}$, $C_2 = a_6 + a_2 a_5$, $C_3 = \frac{b_1 C_2}{a_1 C_1}$ and $C_4 = \frac{C_2}{C_1}\big(\frac{b_1}{a_1} + \frac{1}{R_P^3}\big) + a_5$. Putting all constants in (2.41)-(2.44), we get

$$\sigma_{rP}(r) = d_1\int_0^{r} C_P\ r^2 dr + a_2 C_4\int_0^{R_P} C_P\ r^2 dr \tag{2.54}$$

$$\sigma_{tP}(r) = d_2\int_0^{r} C_P\ r^2 dr + a_2 C_4\int_0^{R_P} C_P\ r^2 dr + d_3 \tag{2.55}$$

Stresses in SEI are:

$$\sigma_{r,SEI}(r) = \left(\frac{a_3 C_1 C_3 - d_4 C_2}{C_1}\right) \int_0^{R_P} C_P \, r^2 dr \tag{2.56}$$

$$\sigma_{t,SEI}(r) = \left(\frac{a_3 C_1 C_3 + d_5 C_2}{C_1}\right) \int_0^{R_P} C_P \, r^2 dr \tag{2.57}$$

where $d_1 = -\frac{2\Omega_P E_P}{3(1-\nu_P))}\frac{1}{r^3}$, $d_2 = -\frac{\Omega_P E_P}{3(1-\nu_P))}\frac{1}{r^3}$, $d_3 = -\frac{\Omega_P E_P C_P}{3(1-\nu_P)}$, $d_4 = \frac{2}{r^3}\frac{E_{SEI}}{1+\nu_{SEI}}$ and $d_5 = \frac{2}{r^3}\frac{E_{SEI}}{1+\nu_{SEI}}$ are constants. Strain energy can be calculated from the stresses stored as a result of elastic deformation [218].

$$e(r,t) = \frac{\sigma_r^2(r,t) + 2\sigma_t^2(r,t) - 2\nu\sigma_t(r,t)[2\sigma_r(r,t) + \sigma_t(r,t)]}{2E} \tag{2.58}$$

2.4.2 Fatigue approach

It has been observed that volume expansion due to intercalation does not usually cross the limit of the yield point [251]. The yield point is defined as the barrier, after which solid material attain permanent deformation. It is also known as elastic limit [252]. However, this does not exclude the possibility of damage to the battery during cycling. The fracture can occur even if the cyclic loads are lower than the critical point due to the continuous loading, causing microscopic structural damage to the battery. The Wohler curves [253] are empirical results of specific materials which relate the number of life cycles to the amplitude of the cycle stress. The mathematical expression of the amplitude of cycle stress is as follows:

$$\sigma_{ampl} = \frac{\sigma_{max} - \sigma_{min}}{2} \tag{2.59}$$

To calculate the maximum number of cycles to failure (N_{max}), Basquin power law is used [253],

$$N_{max} = \left(\frac{\sigma_{yield}}{\sigma_{ampl}}\right)^{\frac{1}{m}} \tag{2.60}$$

where σ_{yield} is the critical stress for static failure and m the slope of σ_{ampl} vs N curve in the bi-logarithmic diagram. One of the limitations of S-N curves is its availability

for known materials, so we need to take the best approximate for graphite or SEI. The parameters of battery and SEI are taken from [78]. If the material is subjected to varying cyclic stresses, this means every charging event is independent [254]. The cumulative damage D_g relates to load and number of cycles by:

$$D_g = \sum_{i=1}^{k} \frac{n_i(\sigma_{ampl\ i})}{N_{max\ i}} \tag{2.61}$$

where $n_i(\sigma_{ampl\ i})$ is the number of applied cycles due to amplitude stress and $N_{max\ i}$ is the number of cycles to failure at amplitude stress. Thus each term after a cycle, contributes to degradation. Substituting (2.60) in (2.61):

$$D_g = \sum_{i=1}^{k} \left(\frac{\sigma_{ampl\ i}}{\sigma_{yield}}\right)^{\frac{1}{m}} n_i(\sigma_{ampl\ i}) \tag{2.62}$$

Ageing tests can be performed by assuming uniform stress conditions, means amplitude stress remain constant throughout the cycling. This simplifies (2.62) to the following form:

$$\frac{D_g}{cycle} = \left(\frac{\sigma_{ampl}}{\sigma_{yield}}\right)^{\frac{1}{m}} \tag{2.63}$$

Thus, any damage to the battery in a cycle is independent to number of applied cycles.

2.4.3 Capacity loss

In normal cyclic conditions, battery's resistance increases slowly. It means capacity loss can be the only variable to predict lifetime of battery. Due to this fact, damage is directly proportional to the capacity loss and can be written as:

$$\frac{D_g}{cycle} = \left(\frac{\sigma_{ampl}}{\sigma_{yield}}\right)^{\frac{1}{m}} \propto \frac{Cap_{loss}(\%)}{cycle} \tag{2.64}$$

The capacity fade does not occur only due to cycling but it happens only in storage conditions (calendar ageing). Total capacity loss can be expressed as :

$$\frac{Cap_{loss}(\%)}{cycle} = \frac{Cap^{cal}_{loss}(\%)}{cycle(hrs)} + \frac{Cap^{cyc}_{loss}(\%)}{cycle} \tag{2.65}$$

where *cal*, *cyc* refer to calendar and cyclic ageing respectively. In this chapter, calender ageing can be neglected due to continuous cyclic pattern. Thus total capacity can be approximated as:

$$\frac{Cap_{loss}(\%)}{cycle} \approx \frac{Cap_{loss}^{cyc}(\%)}{cycle} \tag{2.66}$$

Capacity loss relates to the stress amplitude by using (2.63):

$$\frac{Cap_{loss}(\%)}{cycle} \approx \frac{Cap_{loss}^{cycle}(\%)}{cycle} = A_I \left(\frac{\sigma_{yield}}{\sigma_{ampl}} \right)^{\frac{1}{m}} \tag{2.67}$$

where A_I is a quantification factor of capacity loss and it's value can be determined from [78]. It is worth noting here that if stress amplitude σ_{ampl} becomes zero, assumption of no calendar ageing effect does not valid any more.

The presented model has been integrated to SPM discussed in Section 2.2. Both anode and cathode are assumed to be a single spherical particles, without considering the dynamics of electrolyte.

Chapter 3

Optimisation and Model Predictive Control to reduce Degradation

3.1 Introduction

The dissertation addresses the challenge of optimising the charging trajectory of a lithium-ion battery cell to meet the desired target while avoiding the side reactions responsible for ageing. The work aims to propose an optimal charging profile that decreases the SEI layer's growth and operates the battery in a healthy regime. This chapter presents the non-linear model predictive control (NMPC) strategy to optimise the charging trajectory. The proposed strategy can be a feasible solution in modern battery management systems (BMSs) to reduce degradation.

Conventional BMSs usually impose constraints on externally measured variables such as voltage and current [26]-[29]. The main objective of a BMS is to charge the battery as fast as possible [23]. This leads to the design of a popular constant current constant voltage (CCCV) strategy, which is easy to implement [255]. One of the so-called advantages of CCCV is that it does not have a battery model to operate, which makes charging circuit design easy [255]. This easy-to-use policy affects the battery's health in subsequent cycles of charging/discharging due to higher polarisation voltage [256]. The constant voltage phase is highly time-consuming, and the constant current phase increases the side reactions, ultimately enhancing the degradation processes [257]. The CCCV strategy is independent of the battery model, so it can not differentiate

individual cells of a battery [256, 257]. Charging efficiency tends to drop in CCCV due to neglecting internal resistance [258].

Researchers presented many possible solutions to improve the effectiveness of the CCCV methodology [259]-[266]. Trickle charge constant current constant voltage (TC-CCCV) involves the addition of two trickle charging stages [259]. One is activated before the CC phase in case of a deep discharge level, and the second occurs after the CV phase to complete charging at a reduced current level [259]. It certainly prolongs the battery cycle-life, but charging time is considerably increased. The multi-stage constant current (CC) charging strategy is proposed to reduce the charging time in the CV phas [260]. The battery is charged in different stages at different current values. The current in the next stage is always lower than in the previous stage [260]. At every stage, the current is lowered to a predefined limit, even after achieving the maximum voltage [261].

Although a multi-stage CC enhances the battery life, an incorrect initial SOC estimation can increase the degradation [262]. The accumulation of errors at each step of the estimation process can cause rapid battery ageing [263]. Pulse charging is proposed to reduce the polarisation voltage that occurs in CCCV [264]. It can be discontinuous CC or CV pulses of a higher-order current, reducing the charging time significantly [264]. Pulse charging, however, has some advantages, but higher current rates lead to a thicker SEI layer, which acts as a barrier for intercalated lithium particles [24]. Battery temperature is quite high in the case of pulse charging as compared to CCCV. The boost charging [265] concept is also used to charge the battery, approximately one-third of a discharged battery in five minutes. It operates on a higher current which severely impacts the battery life [55]. Apart from the mentioned traditional charging methods, other strategies reported in the literature on externally measured variables. Constant power constant voltage (CPCV) and constant voltage constant current constant voltage (CV-CCCV) [266] are some popular charging strategies. These charging approaches are model-free, operating only with predefined limits on current, voltage, and power without considering the battery dynamics [266]. All of these approaches are easy to implement, but the corresponding charging trajectory may not be suitable for the health of a battery.

The remainder of this chapter is organised as follows. Section 3.2 briefly introduces Gauss pseudo-spectral method. Section 3.3 demonstrates the proposed NMPC strategy. Sections 3.4 and 3.5 formulate the optimisation problem in chemical and mechanical degradations respectively, along with the definition of benchmark methodology.

3.2 Gauss pseudo-spectral method (GPM)

Implementation of online optimal charging strategies based on electrochemical battery models can be challenging due to two reasons: 1) online method can be computationally expensive, 2) problem is non-linear, particularly due to constraints [95]-[103]. This section describes briefly about Gauss pseudo-spectral method (GPM) which is employed as an efficient optimization method to resolve the online optimization problem. The first requirement in GPM is to change the time interval from arbitrary bounds $t \in [t_0, t_f]$ to the interval $\tau \in [-1, 1]$ by

$$t = \frac{(t_f - t_0)\tau + (t_f + t_0)}{2} \tag{3.1}$$

The Legendre-Gauss (LG) collocation points used in GPM are all interior to the interval $[-1, 1]$ [267]. The initial point $\tau_0 = 0$ and final point $\tau_f = 1$ are also taken into account. The Lagrange interpolating polynomials at a set of collocation points are building blocks for the integration approximation matrix in (3.6). These polynomials can be expressed as [268].

$$L_k(t) = \frac{w(t)}{(t - t_k)\ w'(t_k)}, \tag{3.2}$$

where $t_1, t_2, ...$ are the roots of polynomial while $w(t)$ is a Gauss weight and defined as

$$w(t) = \prod_{i=1}^{N} (t - t_i) \tag{3.3}$$

A function can be approximated using Lagrange interpolation formula as

$$f(t) \approx \sum_{k=1}^{N} f(t_k)\ L_k(t) \tag{3.4}$$

The dynamic constraints are discretised using an integration approximation matrix:

$$X(t_i) = X(t_0) + \frac{t_f - t_0}{2} \sum_{k=1}^{N} A_{ik}\ f\big(X(t_k), t_k\big), \qquad i = 1, ..., N \tag{3.5}$$

where $t_i(s)$ are set of collocation points, A_{ik} is the integral approximation matrix and $X(t_0) = x_0$ is the initial value. The approximation of function (3.4) is simplified due to a unique property of Lagrange polynomials, expressed as [267]:

$$L_j(\tau_i) = \begin{cases} 0 & \text{if} \quad i \neq j \\ 1 & \text{if} \quad i = j \end{cases}$$

The elements in the integral approximation matrix for Gauss points can be approximated by using Axelsson's algorithm [269].

$$A_{ik} = \frac{w_i}{2}\left(1 + t_i + \sum_{v=1}^{n-2} P_v(t_k)\big[P_{v+1}(t_i) - P_{v-1}(t_i)\big] + P_{N-1}(t_k)\big[P_N(t_i) - P_{N-2(t_i)}\big]\right) \tag{3.6}$$

where w_i is the i_{th} Gauss weight and P_j is the j_{th} Legendre polynomial. Finally, cost J can be approximated using pseudo-spectral transcription [74]:

$$J = \Phi(X(t_f), t_f) + \frac{t_f - t_0}{2} \sum_{k=1}^{N} g(X_k, U_k, t_k) w_k \tag{3.7}$$

where Φ relates to terminal condition and $g(.)$ is a function of state, input and time at k_{th} collocation point. The non-linear boundary constraints can be approximated as

$$\phi\big(X(t_0), t_0, X(t_f), t_f\big) = 0 \tag{3.8}$$

The final state $X(t_f)$ is defined as

$$X(t_f) = X(t_0) + \frac{t_f - t_0}{2} \sum_{k=1}^{N} w_k\ f(X_k, U_k, \tau_k), \tag{3.9}$$

The above equation is a Gauss quadrature approximation to the continuous definition of final states. The cost function can be discretised using the quadrature rule, written

as

$$\int_a^b f(t)dt \approx \sum_{i=1}^{N} \alpha_i \, f(t_i) \tag{3.10}$$

where α_i and t_i are i_{th} quadrature weight and point (or node) respectively. The cost (3.7) and non-linear boundary constraints (3.8) form the NLP problem which can be solved by mature optimisation routines.

3.3 Non-linear model predictive control strategy

In this section, we address how to formulate and implement the NMPC control algorithm based on the optimization problem set up in Sections 3.4 and 3.5.

3.3.1 Prediction

A dynamic model predicts future responses of the controlled plant. The system can be represented as a discrete state-space representation form as

$$\mathbf{x}(k+1) = A\,\mathbf{x}(k) + B\,\mathbf{u}(k) \tag{3.11}$$

where $\mathbf{x}(k)$ and $\mathbf{u}(k)$ are prediction model state and input vectors at k_{th} sampling instant respectively. A and B are system matrices. The prediction of states is generated by solving the model over N sampling intervals (prediction horizon), generating an optimal control sequence. Define the state and input sequences for N steps as

$$\mathbf{u}(k) = \begin{bmatrix} u(k|k) \\ u(k+1|k) \\ u(k+2|k) \\ . \\ . \\ u(k+N-1|k) \end{bmatrix}, \quad \mathbf{x}(k) = \begin{bmatrix} x(k+1|k) \\ x(k+2|k) \\ x(k+3|k) \\ . \\ . \\ x(k+N|k) \end{bmatrix} \tag{3.12}$$

where $u(k+j|k)$ and $x(k+j|k)$ denote input and state at time $k+j$, predicted at time k respectively. It means that $x(k+j|k)$ evolves according to the prediction model as

$$x(k+j+1|k) = A\,x(k+j|k) + B\,u(k+j|k), \qquad j = 0, 1, 2, ... \tag{3.13}$$

with initial condition defined as $x(k|k) = x(k)$. In this particular work, there are three states and one input, as discussed in subsection 2.2.2. The final dynamic prediction model in the form of state space is shown below

$$\begin{bmatrix} \dot{\beta}_0(t) \\ \dot{\beta}_2(t) \\ \dot{\beta}_4(t) \end{bmatrix} = \begin{bmatrix} 0 & 10.15 & -20.80 \\ 0 & -11.35 & 23.26 \\ 0 & -13.96 & -62.42 \end{bmatrix} \begin{bmatrix} \beta_0(t) \\ \beta_2(t) \\ \beta_4(t) \end{bmatrix} + 10^{-3} \times \begin{bmatrix} 0.22 \\ 0.28 \\ 0.35 \end{bmatrix} I(t) \tag{3.14}$$

whereas time coefficient $\beta_6(t)$ is redundant because of zero dynamics, but must be known to find the SOC of battery. It can be algebraically calculated using the following output equation.

$$\begin{bmatrix} \beta_6(t) \end{bmatrix} = \begin{bmatrix} 0 & -0.088 & -0.39 \end{bmatrix} \begin{bmatrix} \beta_0(t) \\ \beta_2(t) \\ \beta_4(t) \end{bmatrix} + \begin{bmatrix} 0.22 \end{bmatrix} I(t) \tag{3.15}$$

Finally, from section 3.2 we know that, the output of the system is approximated by

$$\beta_j(\tau) \approx \boldsymbol{\beta_j}(\tau) = \sum_{k=0}^{N} L_k(\tau)\beta_j(\tau_k) \tag{3.16}$$

where β_j is the corresponding output in any electrode and $L_k(\tau)$ is the Lagrange polynomial.

3.3.2 Optimisation

The future predictions are computed by minimising predicted performance cost, defined in terms of states and inputs sequences. Cost function $J(k)$ as defined in (3.7), is a function of $\mathbf{u}(k)$ and optimal input sequence for the problem denoted as $u^*(k)$.

It can be written as

$$\mathbf{u}^*(k) = arg\ min_{\mathbf{u}}\ J(k) \tag{3.17}$$

In this work, the cost function as defined in (3.25), is discretised using Legendre Gauss quadrature rule (3.10). It can be written as

$$J = \int_{t_o}^{t_f} \Big[\big(SOC_n(t) - SOC_{ref}\big)^2 + q\ R'_{film}(t) \Big] dt$$
$$J \approx \frac{t_f - t_0}{2} \sum_{i=1}^{N} \Big[w_i \big(SOC_n(\tau_i) - SOC_{ref}\big)^2 + q\ R'_{film}(\tau_i) \Big] \tag{3.18}$$

where w_i is Gauss weight and computed using (3.3). $R'_{film}(\tau_i)$ can be solved using (3.30). SOC at Legendre Gauss point is written as

$$SOC_n(\tau_i) = \frac{\phi_0(r)\beta_0(\tau_i) + \phi_2(r)\beta_2(\tau_i) + \phi_4(r)\beta_4(\tau_i) + \phi_6(r)\beta_6(\tau_i)}{c_{max,n}} \tag{3.19}$$

3.3.3 Receding horizon implementation

In all of the future optimal input sequence $\mathbf{u}^*(k)$, only the first value is taken as a input to the plant:

$$u(k) = u^*(k|k) \tag{3.20}$$

The process of evaluating $\mathbf{u}^*(k)$ and implementing the first element of $\mathbf{u}^*$ is then repeated at each sampling instance $k = 0, 1, 2, ...$ Due to this repetition of prediction at every instance, it is known as an online optimisation. The prediction horizon keeps its constant length throughout the optimisation process, and therefore the approach is known as a receding horizon strategy. In this work, the term $(t_f - t_0)$ denotes the prediction horizon as seen in the above discretised cost function (3.18). Future N states $[\beta_0(t), \beta_2(t), \beta_4(t)]^T$ and N inputs $I(t)$ are predicted at a current sampling instant. In the next sampling instant, $t_f - t_0$ will be the same as in last instant but initial values of the system is changed.

3.3.4 Constraints

Apart from any obvious equality constraints that satisfy the dynamics of the model, every control problem encounters inequality constraints on input and state variables. As noted from the problem (3.25), one input (current) and two non-linear constraints (voltage and side reaction overpotential) are part of this optimisation exercise. The linear inequality constraint is of the form

$$A_{eq}\,\mathbf{x} \leq b_{eq} \tag{3.21}$$

Using eq. (3.5), we get the following form of linear inequality constraint

$$\begin{bmatrix} I_N & -Tt \times A(1,2) \times M_N & -Tt \times A(1,3) \times M_N & -Tt \times B(1,1) \times M_N \\ \mathbf{0}_N & I_N - Tt \times A(2,2) \times M_N & -Tt \times A(2,3) \times M_N & -Tt \times B(2,1) \times M_N \\ \mathbf{0}_N & -Tt \times A(3,2) \times M_N & I_N - Tt \times A(3,3) \times M_N & -Tt \times B(3,1) \times M_N \end{bmatrix} \begin{bmatrix} \beta_{0_{N\times 1}} \\ \beta_{2_{N\times 1}} \\ \beta_{4_{N\times 1}} \end{bmatrix} <= \begin{bmatrix} \beta_{0,i} \times \mathbf{1}_{N\times 1} \\ \beta_{2,i} \times \mathbf{1}_{N\times 1} \\ \beta_{4,i} \times \mathbf{1}_{N\times 1} \end{bmatrix} \tag{3.22}$$

where $I_N, \mathbf{0}_N$ are $N \times N$ identity and zero matrices respectively. M_N is an integration approximation matrix of order $N \times N$, as defined in (3.6). A and B are system matrices, taken from (2.25). According to Gauss pseudo-spectral notation, $x_{j_{N\times 1}}$ means $[x_j(\tau_1), x_j(\tau_2), x_j(\tau_3), ., ., ., x_j(\tau_N)]^T$. This size of A_{eq} *and* b_{eq} matrices depends on the chosen prediction horizon. The two non-linear constraints are voltage V_{cell} and side reaction overpotential η_{sr}; both are function of states and input. In pseudo-

spectral notation using eqs. (2.18) and (2.19), it can be written as

$$V(\tau_i)) = \frac{R_{gas}T}{F}\left[\ln\left(\frac{J_p(\tau_i)}{i_{o,p}(\tau_i)a_p}\right) - \ln\left(\frac{J_n(\tau_i)}{i_{o,n}(\tau_i)a_n}\right)\right] + U_p\left(SOC_p^{ref}(\tau_i)\right) - U_n\left(SOC_n^{ref}(\tau_i)\right) + I(\tau_i)$$
(3.23)

$$\eta_{sr}(\tau_i) = \frac{R_{gas}T}{F}\ln\left(\frac{J_n(\tau_i)}{i_{o,n}(\tau_i)a_n}\right) + U_n\left(SOC_n^{ref}(\tau_i)\right) \tag{3.24}$$

Finally, the algebraic cost (3.18), along with linear (3.21) and non-linear constraints (3.23 , 3.24) make up the NLP problem. It is further solved by MATLAB function "fmincon" in this work.

3.4 Problem formulation: chemical degradation

The main aim of the control problem is to minimise SEI film resistance during charging. We adopt the receding horizon control concept to conduct online optimization at each sampling time. The optimization problem to be resolved is expressed as

$$\begin{aligned}
&\underset{I(t)}{\text{minimize}} \quad \int_{t_o}^{t_f}\left[\left(SOC_n(t) - SOC_{ref}\right)^2 + q\ R_{film}^{'}(t)\right]dt \\
&\text{subject to} \\
&model\ Eq.(2.7) - (2.19), (2.25), \\
&0 \le I(t) \le I_{max}, \\
&0 \le V(t) \le V_{max}, \\
&\eta_{sr} \ge 0
\end{aligned} \tag{3.25}$$

where q is control parameter, $R_{film}^{'}(t)$ is the time rate change of film resistance, SOC_{ref} is reference state of charge, η_{sr} is side reaction overpotential, and I_{max}, V_{max} are the maximum current and voltage respectively. The goal of this problem is to charge the cell to the desired SOC, SOC_{ref}, and minimize the growth of SEI film resistance. Also, the battery should operate in the healthy regime defined by the constraints on current, voltage and overpotential. Please note that side reaction overpotentials η_s *and* η_{sr} are not similar. η_s is side reaction based upon diffusion of

the organic solvent present in electrolyte, while η_{sr} is due to the lithium plating which should be greater than or equal to zero for the safe operation of the battery. SOC in a negative electrode can be written, using equation (2.7), as

$$SOC_n(t) = \frac{\phi_0(r)\beta_0(t) + \phi_2(r)\beta_2(t) + \phi_4(r)\beta_4(t) + \phi_6(r)\beta_6(t)}{c_{max,n}} \tag{3.26}$$

$R'_{film}(t)$ is a function of intercalation and side reaction overpotentials in the negative electrode (2.33). Equating (2.27) and (2.29), we get

$$\eta_s = \eta_n + U_{n,ref} - U_{ref,s} \tag{3.27}$$

where $\eta_n(t)$ can be written, using (2.5), (2.14) and (2.16), as

$$\eta_n(t) = \frac{R_{gas}T}{F} \ln\left(\frac{J_n(t)}{i_{o,n}(t)a_n}\right) \tag{3.28}$$

Overpotential is a function of surface concentration $c_n^{surf}(t)$, which can be approximated by

$$c_n^{surf}(t) = \phi_0(R)\beta_0(t) + \phi_2(R)\beta_2(t) + \phi_4(R)\beta_4(t) + \phi_6(R)\beta_6(t) \tag{3.29}$$

Finally $R'_{film}(t)$ can be formulated as

$$\begin{aligned} R'_{film}(t) = X\ exp\Bigg\{ &- \left(\frac{R_{gas}T}{2F}\right)\Bigg[\left(\frac{R_{gas}T}{F}\right) \\ &\ln\Bigg(\frac{-I(t)}{A_n L_n k_n \sqrt{\phi_0(R)\beta_0(t) + \phi_2(R)\beta_2(t) + \phi_4(R)\beta_4(t) + \phi_6(R)\beta_6(t) - c_{max,n}}} \\ &\frac{1}{\sqrt{\phi_0(R)\beta_0(t) + \phi_2(R)\beta_2(t) + \phi_4(R)\beta_4(t) + \phi_6(R)\beta_6(t)}\sqrt{c_e}}\Bigg) + \\ &U_{n,ref}\left(\frac{\phi_0(R)\beta_0(t) + \phi_2(R)\beta_2(t) + \phi_4(R)\beta_4(t) + \phi_6(R)\beta_6(t)}{c_{max,n}}\right) - 0.4\Bigg]\Bigg\} \end{aligned} \tag{3.30}$$

where X is a constant with value of 5.4×10^{-10} . Moreover, pseudo-spectral method discretise the cost function (3.25) using (3.7) to form a NLP problem. The proposed approach is compared against the optimal charging method without incorporating the

SEI layer growth rate, which aims to resolve the online optimization problem:

$$\begin{aligned} &\underset{I(t)}{\text{minimize}} \quad \int_{t_o}^{t_f} \left(SOC_n(t) - SOC_{ref}\right)^2 dt \\ &\text{subject to} \\ &\textit{model Eq.}(2.7) - (2.18), (2.25), \\ &0 \leq I(t) \leq I_{max}, \\ &0 \leq V(t) \leq V_{max} \end{aligned} \tag{3.31}$$

3.5 Problem Formulation: mechanical degradation

The main aim of this control problem is to minimise strain energy during charging. For this purpose, an optimal charging problem is used for demonstration of the concept. To charge a battery healthily, the optimal problem is used to minimise the degradation effects. The term "healthily" relates capacity fade with optimised charging range of the battery. Stress amplitude must be lowered to reduce the damage to the battery caused by cyclic loading. Mathematically problem can be formulated as:

$$\begin{aligned} &\underset{I(t)}{\text{minimize}} \quad \int_{t_o}^{t_f} \left[\left(SOC_n(t) - SOC_{ref}\right)^2 + q\ e(r,t)\right] dt \\ &\text{subject to} \\ &\textit{model Eq.}(2.7) - (2.18), (2.25), \\ &0 \leq I(t) \leq I_{max}, \\ &0 \leq V(t) \leq V_{max} \end{aligned} \tag{3.32}$$

where q is control parameter, $e(r,t)$ (2.58) is the time rate change of strain energy, SOC_{ref} is reference SOC, I_{max}, V_{max} are the maximum current and voltage, respectively. The goal of this problem is to charge the cell to a desired SOC, SOC_{ref}, along with minimising stress amplitude. Using equation (2.7), SOC in negative electrode can be written as

$$SOC_n(t) = \frac{\phi_0(r)\beta_0(t) + \phi_2(r)\beta_2(t) + \phi_4(r)\beta_4(t) + \phi_6(r)\beta_6(t)}{c_{max,n}} \tag{3.33}$$

Two terms are important to understand the problem formulation in diffusion-induced stresses i.e. $\int_0^{R_p} C_P\ r^2 dr$ and $\int_0^r C_P\ r^2 dr$. First is the integral part of radial and tangential stresses in SEI while later evaluates the lithium concentration in whole active particle. The concentration in any electrode can be represented as (2.20)

$$C_P(r,t) \approx \phi_0(r)\beta_{0,n}(t) + \phi_2(r)\beta_{2,n}(t) + \phi_4(r)\beta_{4,n}(t) + \phi_6(r)\beta_{6,n}(t) \tag{3.34}$$

where $\phi_i(r)$ is the known Legendre polynomial and $\beta_i(t)$ is the time coefficient to depict the dynamics of electrode. The first four even Legendre polynomials used in this chapter are as follows:

$$\begin{aligned}
\phi_0(r) &= \sqrt{\frac{1}{R_P}} \\
\phi_2(r) &= \frac{1}{2}\sqrt{\frac{5}{R_P}}\left[3\frac{r^2}{R_P^2} - 1\right] \\
\phi_4(r) &= \frac{1}{8}\sqrt{\frac{9}{R_P}}\left[35\frac{r^4}{R_P^4} - 30\frac{r^2}{R_P^2} + 3\right] \\
\phi_6(r) &= \frac{1}{16}\sqrt{\frac{13}{R_P}}\left[231\frac{r^6}{R_P^6} - 315\frac{r^4}{R_P^4} + 105\frac{r^2}{R_P^2} - 5\right]
\end{aligned} \tag{3.35}$$

Solving $\int_0^{R_p} C_P\ r^2 dr$ and $\int_0^r C_P\ r^2 dr$ to evaluate (2.54)-(2.58):

$$\int_0^r C_P\ r^2 dr = \int_0^r r^2 \Big(\phi_0(r)\beta_0(t) + \phi_2(r)\beta_2(t) + \phi_4(r)\beta_4(t) + \phi_6(r)\beta_6(t)\Big) dr$$

$$\begin{aligned}
\int_0^r C_P\ r^2 dr = \int_0^r \Bigg[&\frac{r^2}{\sqrt{R_P}}\beta_0(t) + \frac{1}{2}\sqrt{\frac{5}{R_P}}\left(\frac{3r^4}{R_P^2} - r^2\right)\beta_2(t) + \frac{1}{8}\sqrt{\frac{9}{R_P}}\left(\frac{35r^6}{R_P^4} - \frac{30r^4}{R_P^2} + 3r^2\right)\beta_4(t) \\
&+ \frac{1}{16}\sqrt{\frac{13}{R_P}}\left(\frac{231r^8}{R_P^6} - \frac{315r^6}{R_P^4} + \frac{105r^4}{R_P^2} - 5r^2\right)\beta_6(t)\Bigg] dr
\end{aligned}$$

$$\begin{aligned}
\int_0^r C_P\ r^2 dr = \Bigg[&\frac{r^3}{3\sqrt{R_P}}\beta_0(t) + \frac{1}{2}\sqrt{\frac{5}{R_P}}\left(\frac{3r^5}{5R_P^2} - \frac{r^3}{3}\right)\beta_2(t) + \frac{1}{8}\sqrt{\frac{9}{R_P}}\left(\frac{35r^7}{7R_P^4} - \frac{30r^5}{5R_P^2} + \frac{3r^3}{3}\right)\beta_4(t) \\
&+ \frac{1}{16}\sqrt{\frac{13}{R_P}}\left(\frac{231r^9}{9R_P^6} - \frac{315r^7}{7R_P^4} + \frac{105r^5}{5R_P^2} - \frac{5r^3}{3}\right)\beta_6(t)\Bigg]
\end{aligned} \tag{3.36}$$

Multiply both sides with $\frac{1}{r^3}$ and simplify to get:

$$\frac{1}{r^3}\int_0^r C_P\, r^2 dr = \frac{1}{3\sqrt{R_P}}\beta_0(t) + \frac{1}{2}\sqrt{\frac{5}{R_P}}\left(\frac{3r^2}{5R_P^2} - \frac{1}{3}\right)\beta_2(t) + \frac{1}{8}\sqrt{\frac{9}{R_P}}\left(\frac{5r^4}{R_P^4} - \frac{6r^2}{R_P^2} + 1\right)\beta_4(t) + \frac{1}{16}\sqrt{\frac{13}{R_P}}\left(\frac{77r^6}{3R_P^6} - \frac{45r^4}{R_P^4} + \frac{21r^2}{R_P^2} - \frac{5}{3}\right)\beta_6(t) \tag{3.37}$$

Similarly $\int_0^{R_p} C_P\, r^2 dr$ can be written as

$$\begin{aligned}\frac{1}{R_P^3}\int_0^{R_p} C_P\, r^2 dr &= \frac{1}{3\sqrt{R}}\beta_0(t) + \frac{1}{2}\sqrt{\frac{5}{R}}\left(\frac{3}{5} - \frac{1}{3}\right)\beta_2(t) + \frac{1}{8}\sqrt{\frac{9}{R}}\left(5 - 6 + 1\right)\beta_4(t) \\ &\quad + \frac{1}{16}\sqrt{\frac{13}{R}}\left(\frac{77}{3} - 45 + 21 - \frac{5}{3}\right)\beta_6(t) \\ &= \frac{1}{3\sqrt{R}}\beta_0(t) + \frac{2}{3\sqrt{5R}}\beta_2(t)\end{aligned} \tag{3.38}$$

To compare the results with proposed optimal control problem, this article uses standard CCCV charging problem defined in (3.31) This work is also compared with experimental results published in [78]. High energy 18650 lithium-ion battery with a nominal capacity of 2.05 has been used. All the cycling tests simulations are recorded at 35 °C with $1C$ as maximum current. In the experimental work, voltage adjustment is made after 100 cycles while in the simulation procedure is adjusted every ten cycles. The relationship between the open-circuit voltage and SOC is critical in this optimisations framework for accurate adjustment of voltage levels. The experimental curve is given by Laresgoiti et al. [79], to calculate the overpotential at the current SOC of the battery.

Chapter 4

Optimal Charging: Results and Discussion

4.1 Optimal charging: chemical degradation

The control problem (3.25) in Section 3.4 formulates the charging trajectory in lithium-ion batteries. The control target is to reach reference state of charge with minimum possible SEI layer growth and avoiding side reaction overpotential due to lithium plating. The literature survey reports several published works on health-conscious NMPC of lithium-ion batteries, where the effect of lithium plating consider in the online optimal charging of battery management system (BMS) such as [86]. Battery charge/trajectory is expressed in terms of one flat output trajectory to reduce computational burden by a factor of 5 compared with pseudo-spectral optimisation alone. Moreover, the proposed constant current constant side reaction overpotential (CCCη) strategy ensured the side reaction constraint to remain in a healthy regime during charging, i.e. positive or zero. However, in [86], authors considered only one side reaction with no quantification of SOH. Optimal charging trajectories are calculated in a healthy regime without estimation of degradation effects [80, 81]. Moreover, researchers also proposed a health-aware fast-charging methodology using model predictive control. For example, [179] explored the moving horizon approach incorporating chemical degradation effects, but the SEI film resistance is not estimated. Due to ageing effects, battery SOH does not follow a specified trajectory.

This deviation is minimised by proposing the balancing control method [82]. The effect of temperature and degradation effects also alter the voltage and state of energy responses [83]. All of the above research works do not contribute to quantifying the ageing effect represented by the thickness of the SEI layer.

4.1.1 Results and Discussion

The initial SOC is set to 0.4 while two upper current limits are considered in this work, i.e. $I_{max} = 5A$ and $7A$. Reference state of charge, SOC_{ref} is taken as 0.96, and the voltage limit is set to 4.2 volts. Problem (3.25) is set to start at $t_o = 0$, using a NMPC approach. At each time step, the solver predicts future instances with a prediction horizon of $100s$ using four collocation points. The initial guess of the solution at the present time step is a solution at the last sampling instance. Figure 4.1 shows the pictorial representation of algorithm.

SOC in the negative electrode is shown in Figure 4.2(a) and (d) for $I_{max} = 5A$ and $7A$, respectively. SOC is compared for two charging methods: the proposed method (3.25) and the method (3.31) presented in [86]. It can be seen that the reference SOC is achieved in each methodology but charging time in the proposed optimal case is higher than the method (3.31) for both upper limits of current. In the case of $I_{max} = 5A$, a 9.6% increase in charging time is recorded in the proposed method (3.25) while at $I_{max} = 7A$, charging time difference is 22%. The higher difference in case of $I_{max} = 7A$ is understandable because the CCCV methodology charges the battery in constant current (CC) scenario for maximum time. As we increase the maximum current for both methodologies, the difference in charging time becomes larger. Note that longer charging time using the proposed SEI optimal charging method can significantly reduce the SEI layer growth as demonstrated below.

It is a known practice that CCCV charging terminates at fairly low current i.e. 5 mA or 50 mA. In this work, the later current value is used. In Figure 4.2(a), SOC reaches the reference value at t_1 while it stays at same value until t_2. This is due to the current profile in CCCV charging. The optimal CCCV algorithm charges the battery

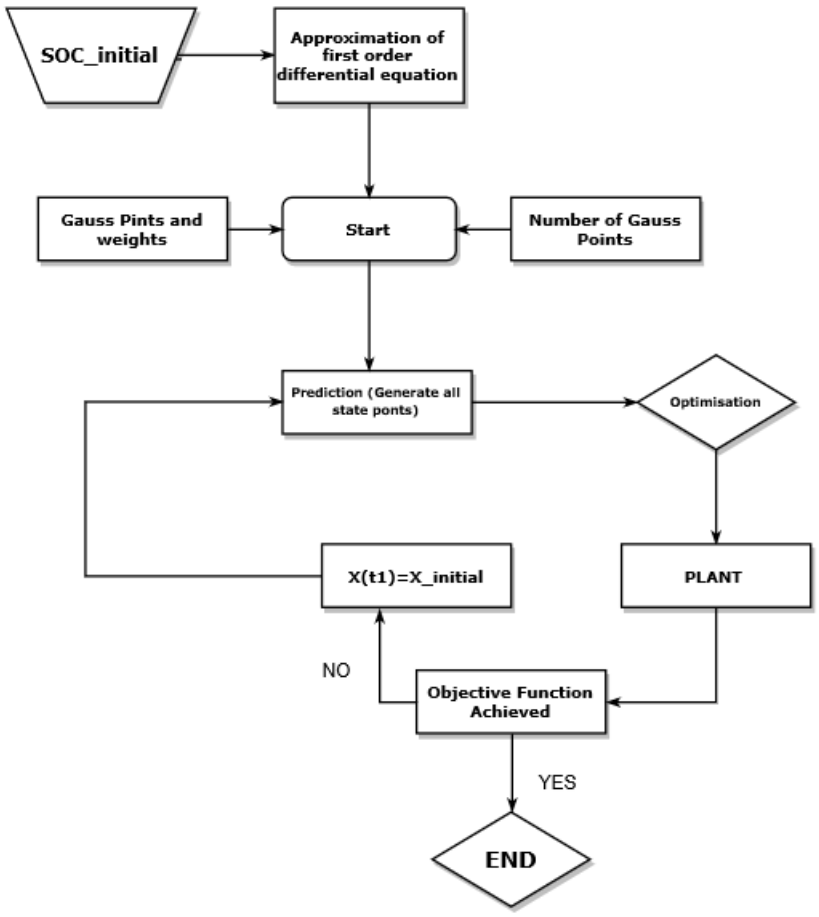

Figure 4.1: Proposed Algorithm to minimise SEI layer growth considering chemical degradation

using constant current (CC) approach from $t = 0$ to $t = t_1$. At t_1, it switches to constant voltage (CV) approach which means current needs to be lower down to keep the voltage constant. Reference SOC is achieved at t_1 which needs to be same till t_2. Current value drops from I_{max} to 50 mA in time span of $t_1 - t_2$.

Figure 4.2(b) and (e) depict the results of optimal CCCV charging for $I_{max} = 5A$ and $7A$, respectively. CCCV charging splits into two phases; CC from $t = 0$ to $t = t_1$ and CV from $t = t_1$ to $t = t_2$. In both cases for SEI reduction optimal charging method, charging starts at fairly low value to reduce the rate of lithium plating. This is because, at low SOCs, the reference potential of the negative electrode is quite high, i.e. the possibility of η_{sr} to be negative. Thus to be in the healthy regime, the charging current needs to increase slowly, since higher current can lead to lower resistance of the SEI layer. The proposed SEI reduction optimal charging profile finishes, in either of the maximum current limits, at higher current value as compared to the optimal

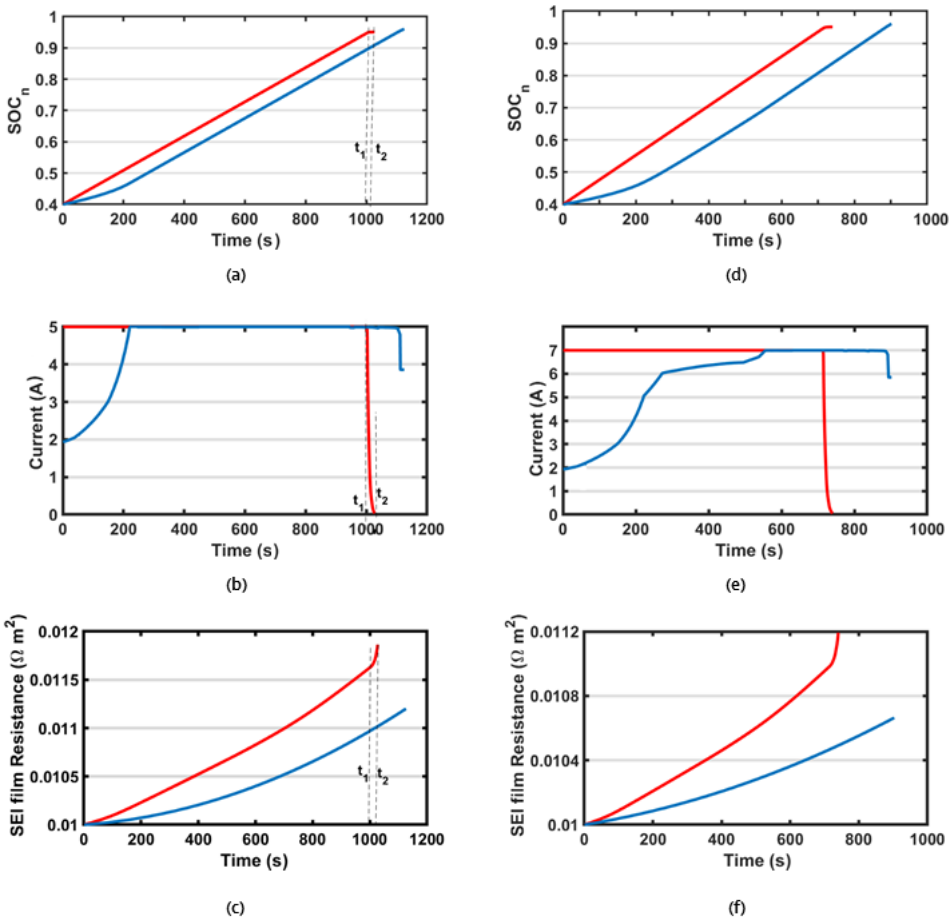

Figure 4.2: Comparison of state of charge (a,d), current profile (b,e) and SEI film resistance (c,f) vs charging time at current upper bounds of $I_{max} = 5A$(a-c) and $I_{max} = 7A$(d-f)-Optimal CCCV charging(–), Proposed SEI optimal charging(–)

CCCV charging method. Termination of SEI optimal charging at higher current value has two advantages, (i) it compensates for charging time which considerably increases due to low SOC regime (where η_{sr} can be negative), and (ii) It reduces the growth of SEI layer which increases at low values of current.

The growth of SEI film resistance is shown in Figure 4.2(c) and (f) for $I_{max} = 5A$ *and* $7A$, respectively. It is evident from the figures that SEI film resistance is quite high in optimal CCCV and SEI optimal charging cases when maximum current is $5A$. The primary reason is that lower current takes more time to complete charging. SEI film resistance drops significantly in proposed SEI optimal charging compared to the optimal CCCV charging at given maximum current value. The overall optimal charging time increases but SEI film resistance decreased. This can be explained as at higher SOCs the algorithm uses a maximum value of current, so that molar flux is high. In case of $I_{max} = 5A$ (Figure 4.2(e)), SEI layer resistance is recorded as

0.0118 Ωm^2 in optimal CCCV case, reduced to 0.0112 Ωm^2 in proposed SEI optimal formulation scenario. The percentage increase of SEI layer resistance from initial value (0.01 Ωm^2) is 18% and 12% in optimal CCCV and the proposed SEI reduction optimal charging method, respectively, which represents a 5.2% decrease of SEI layer growth using the proposed charging method. Lower percentage difference is recorded (4.95%) in case of $I_{max} = 7A$ (Figure 4.2(f)) between two strategies. The main difference is in the final phase of optimal CCCV charging, where it uses low current as compared to the proposed optimal approach. The maximum value of surface concentration and negative η_{sr} increase the SEI layer resistance to a fairly high value in optimal CCCV approach.

The profile of SEI layer in optimal CCCV charging can be categorised on the basis of SOC regimes, i.e. low or high. At low SOC regime, the current is high, which acts as a source of lithium plating. At maximum current, overpotential of negative electrode (3.28) is high, which makes side reaction overpotential η_{sr} (3.24) negative. This is not desirable as only positive η_{sr} guarantees the reduction of lithium plating side effects. Termination of optimal CCCV charging usually happens at low current, which is 50 mA in this work. Due to low current at the end stage of charging (t_1 to t_2), side reaction overpotential for SEI layer η_s (2.29) is very low. The exponential term in (2.33) ultimately leads to spike in SEI layer profile at the final stage of optimal CCCV charging.

Another added advantage of the proposed algorithm is to charge batteries in the healthy regime, which means side reaction overpotential of lithium plating is positive during the whole process. Note that cost function does not always guarantee the desired result. It can be argued that side reaction overpotential will always be positive to decrease the value of the exponential term in the cost function. However, this cannot be extrapolated for an entire range of possible values of current which indicates that limit on η_{sr} is necessary in this work. Figure 4.3 shows side reaction overpotential η_{sr} in optimal CCCV and SEI optimal charging. It is evident from the figure that in optimal CCCV charging, η_{sr} is negative while it is positive in proposed SEI optimal charging, successfully avoiding lithium plating. Hence, It means that the proposed charging algorithm runs in a healthy regime along with reducing SEI film

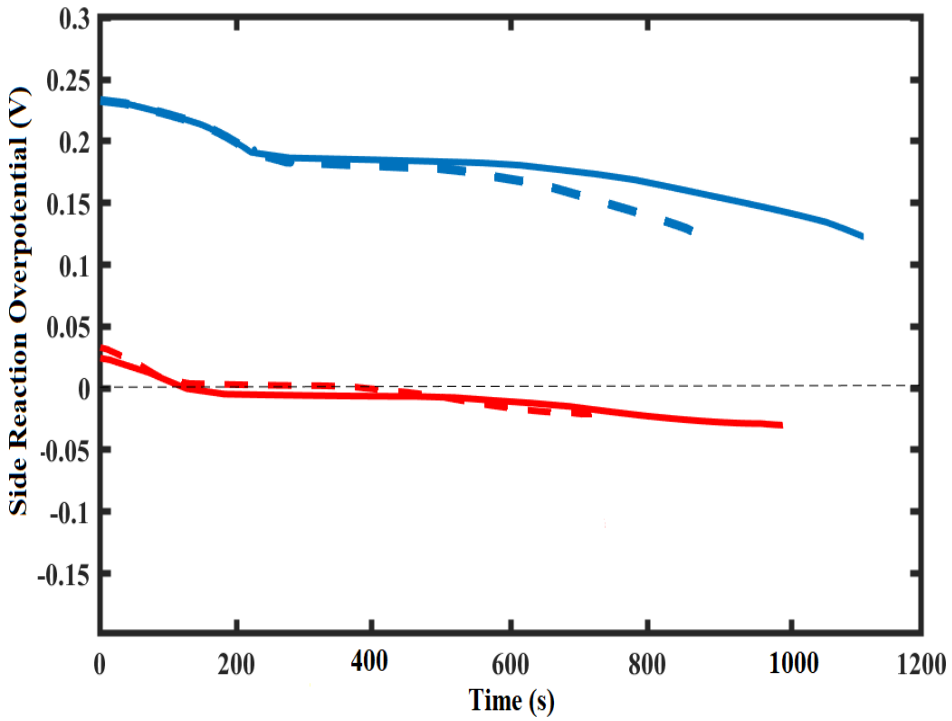

Figure 4.3: Relationship between charging time and side reaction overpotential(η_{sr}) in the proposed SEI optimal charging (–) and optimal CCCV charging (–) approaches, $I_{max} = 5A$(solid) and $I_{max} = 7A$(dashed)

resistance.

Total charging time and maximum charging current value affect the resistance of the SEI layer growth. In optimal CCCV charging, higher current upper bound means fast charging and lesser growth of the SEI layer. However, the optimal algorithm makes sure that SEI layer resistance is as low as possible along-with successfully avoiding lithium plating during the whole process of charging. If the current upper bound is constant, charging time is higher in the SEI optimal charging case than optimal CCCV but quite low SEI film resistance. Next, we compare the two methods in two scenarios to investigate: (i) At what conditions, is charging time for both methodologies the same? (ii) If SEI film resistance is the same, how does charging time relate to current upper bound?

Scenario I: Same Charging time

In optimal CCCV strategy, the upper bound current is inversely proportional to the charging time and SEI layer resistance. To get the same charging time for both methodologies, the maximum current limit of SEI optimal strategy should be higher

than optimal CCCV. Two cases are recorded in this analysis, where charging time is the same in both strategies.

It is evident from Table 4.1 that in order to get the same charging time, current

Table 4.1: Same Charging Time Cases

Case No.	Charging time (s)	Current upper bound in SEI optimal charging, I_{max}(A)	Current upper bound in optimal CCCV charging, I_{max}(A)
1	1125	5	4.55
2	902	7	5.7

upper bounds in both strategies are not the same. Consider case 2 of Table 4.1, the charging time is set to 902 seconds which is charging time for SEI optimal strategy at $I_{max} = 7A$ (Figure 4.2(d), (e) and (f)). To get same charging time for optimal CCCV, current upper bound needs to decrease because at $I_{max} = 7A$, charging time is 740 seconds. Figures 4.4 and 4.5 show the relationship between SOC, current and SEI layer resistance versus time.

Figure 4.4(a) shows the SOC of the negative electrode. Reference SOC is attained in both methods at the same time. The optimal SOC profile initially has a slightly low slope as compared to optimal CCCV. This is because of the optimal charge current profile (Figure 4.4(b)), which starts at a reasonably low value. The primary reason is to control side reaction overpotential at a low SOC, ultimately avoiding the effects of lithium plating.

At $I_{max} = 5.7A$, SEI layer resistance is recorded as 0.01155 Ωm^2(15.5% increase) compared to the SEI layer growth in the proposed SEI optimal charging method, as shown in Figure 4.5. The percentage increase in the SEI layer at $I_{max} = 5.7A$, goes up to approximately 2.5% compared to charging at $I_{max} = 7A$. Hence, the percentage difference of SEI layer resistance between proposed SEI optimal and optimal CCCV strategies climbs up to 8.6% keeping similar charging time.

Similar results are found for case 1 of Table 4.1, which shows that to get the similar charging time of 1125 seconds, the current upper bounds must be $5A$ and $4.55A$ in proposed SEI optimal and optimal CCCV strategies, respectively. The SEI layer resistance in optimal CCCV is increased to 0.01211 Ωm^2(21.1% increase) which is 0.0118 Ωm^2 at $I_{max} = 5A$. An overall percentage increase of 3.1% is recorded as

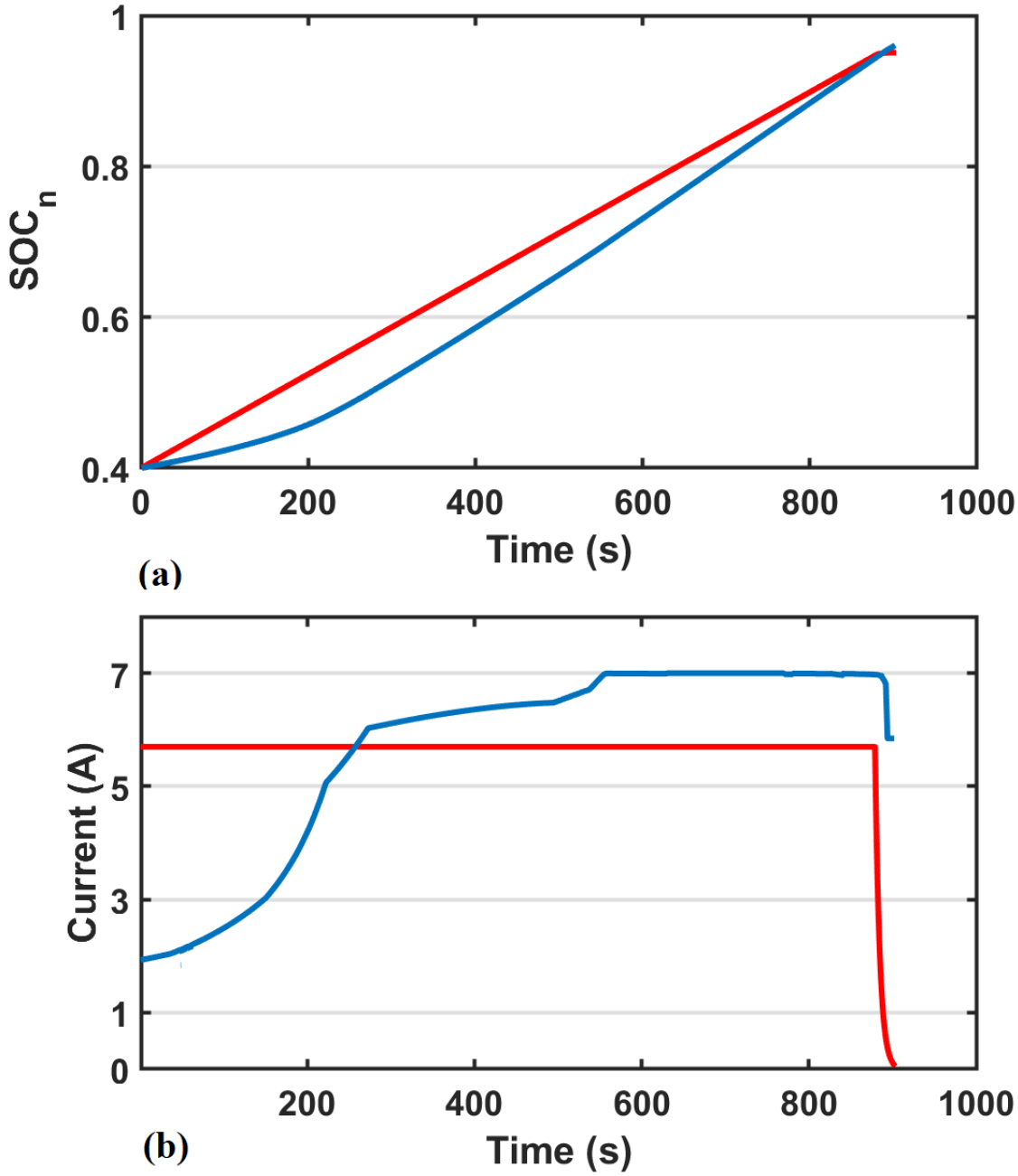

Figure 4.4: State of charge (a) and current profile (b) for same charging time-Case 2 of Table 4.1- Optimal CCCV Charging($I_{max} = 5.7A$), Proposed SEI optimal charging($I_{max} = 7A$)- Optimal CCCV charging(–), Proposed SEI optimal charging(–)

at $I_{max} = 4.55A$ compared to optimal CCCV at $I_{max} = 5A$. Thus, the percentage difference of SEI layer resistance between proposed SEI optimal and optimal CCCV strategies climbs up to 7.8% keeping similar charging time.

Scenario I analysis is summarised in Figure 4.6. It shows a relationship between charging time versus maximum current upper bound. Maximum current is taken from $2.3A(1C)$ to $9.2A(4C)$. Understandably, optimal CCCV charging is fast at a specific current upper bound value. For example, at $I_{max} = 7A$, proposed SEI optimal

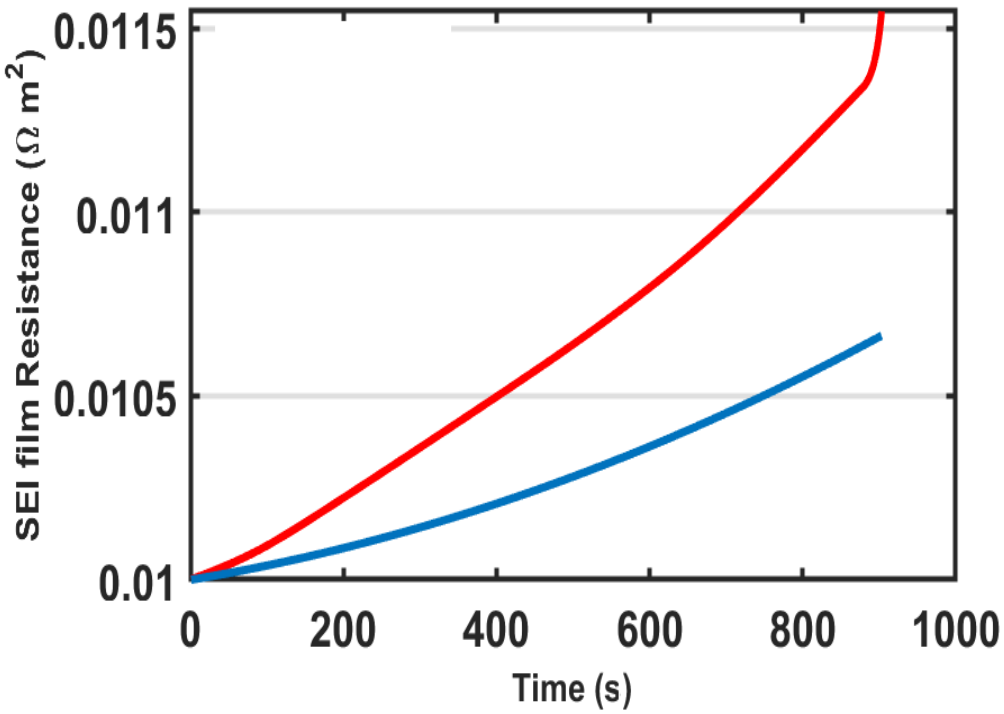

Figure 4.5: Same Charging time- Comparison of SEI film resistance in optimal CCCV charging ($I_{max} = 5.7A$) and proposed SEI optimal charging ($I_{max} = 5.7A$)-Optimal CCCV charging(–), Proposed SEI optimal charging(–)

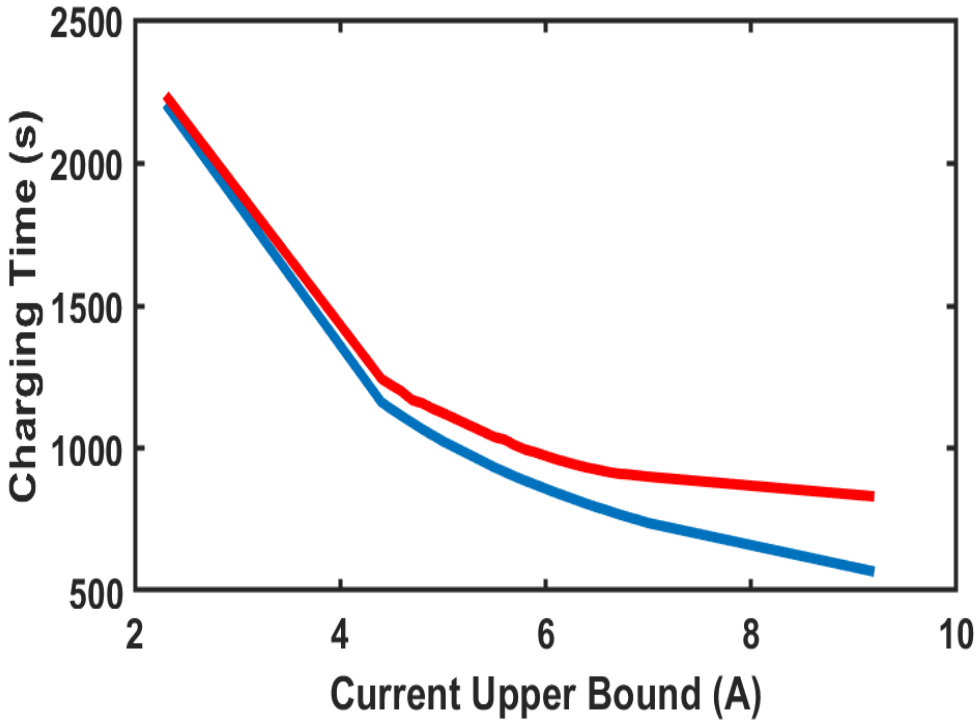

Figure 4.6: Relationship between charging time and current upper bound (I_{max}) in optimal CCCV and proposed SEI optimal charging methodologies-Optimal CCCV charging(–), Proposed SEI optimal charging(–)

charging takes almost three extra minutes. In order to find the same charging time for both methods, one can get values of current upper bounds by drawing vertical and horizontal lines from data labels. For charging time of 1100 seconds, maximum current values of optimal CCCV and proposed SEI optimal methodologies should be $4.7A$ and $5.1A$, respectively. As the maximum value of current increases, charging time difference between optimal CCCV and the proposed SEI optimal charging strategies also increases.

The conclusion from the scenario I is that charging time for proposed SEI optimal and optimal CCCV strategies can be the same, but on the cost of higher SEI layer growth. The proposed method outperforms the optimal CCCV because of two reasons; (i) SEI layer growth is low and (ii) it successfully avoids side reaction overpotential to attain value less than zero. Thus by keeping current upper bound or charging time same, the proposed SEI optimal framework is far better than optimal CCCV as it minimises SEI layer growth and tackles lithium plating too.

Scenario II: Same SEI layer Resistance

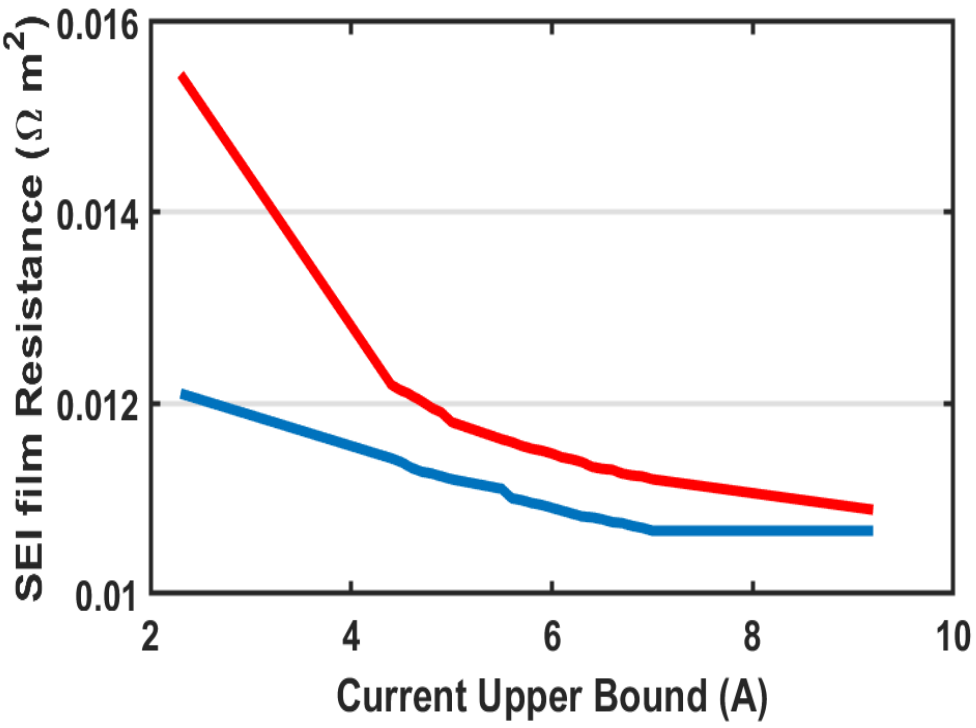

Figure 4.7: Relationship between SEI film resistance and current upper bound (I_{max}) in optimal CCCV and proposed SEI optimal charging methodologies-Optimal CCCV charging(–), Proposed SEI optimal charging(–)

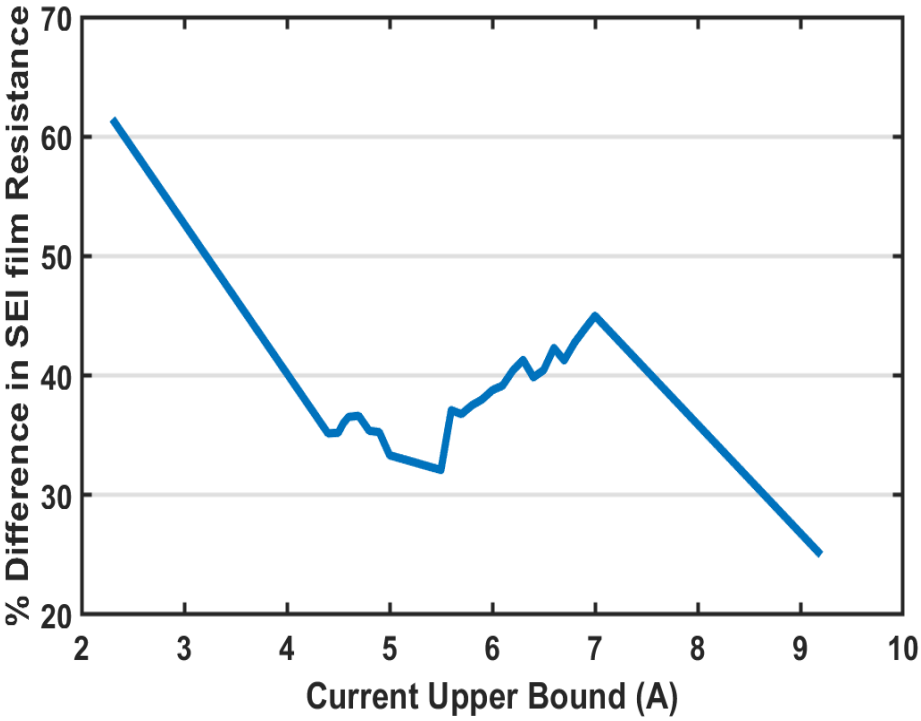

Figure 4.8: Percentage difference in SEI layer resistances between optimal CCCV and proposed SEI optimal charging methodologies from I_{max} =1C (2.3A) to I_{max} =4C (9.2A)

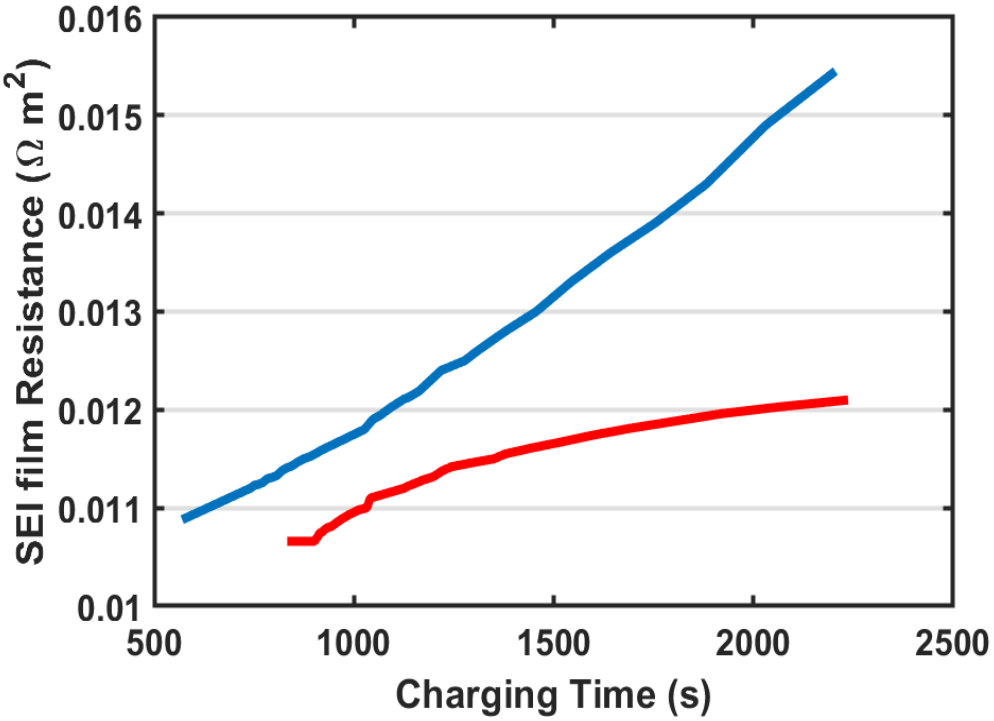

Figure 4.9: SEI film resistance versus charging time in optimal CCCV and proposed SEI optimal charging methodologies-Optimal CCCV charging(–), Proposed SEI optimal charging(–)

Figure 4.7 shows the relationship between SEI layer growth and maximum current in both methodologies. It can be seen that at low current rating, the difference in the SEI layer resistances corresponding to optimal CCCV and proposed SEI optimal strategies is high. As the value of the maximum current increases, the difference in the SEI layer resistances decreases. The primary reason for a more significant difference in the SEI layer at low current, is the high charging time. To get SEI layer resistance of 0.011 Ωm^2, the maximum current in optimal CCCV and proposed SEI optimal methodologies should be $8.1A$ and $5.6A$, respectively. Thus, a proposed optimal framework uses a low current upper bound along with generating small value of SEI layer resistance. It has been noted that there is no significant change in SEI layer resistance from $I_{max} = 7A$ to $9.2A$ in proposed optimal charging framework.

The percentage difference in SEI layer resistance between optimal CCCV and proposed SEI Optimal methodologies is shown in Figure 4.8. The highest percentage difference is recorded as 61% at the current rating of $1C$. This difference kept on decreasing from $1C$ to $2C$ and $3C$ to $4C$. The percentage difference fluctuates around 5% from $2C$ to $3C$. Because of the minimum range of work from $3C$ to $4C$, % difference in SEI layer growth is almost constant.

Charging time is not the only factor that influences SEI layer growth, but higher current can contribute to exfoliation of graphite. It leads to a loss of active anode material which can be a source of capacity and power fade. Hence, it can be concluded from the above analysis that battery charging is a trade-off between optimal charging time and the current upper bound.

Scenario II analysis is summarised in Figure 4.9. It shows the relationship between SEI layer resistance and charging time at the current upper bound range of $1C$ to $4C$. It is evident from Figure 4.9 that at any charging time, SEI layer resistance is higher in optimal CCCV than the proposed SEI optimal charging. SEI layer resistance is recorded as 0.0117 Ωm^2 (proposed SEI optimal) and 0.0132 Ωm^2(optimal CCCV), at the charging time of 1500 *seconds*. The percentage difference in SEI layer resistance is 12 % whereas the corresponding maximum current I_{max} is 3.2 A and 3.6 A in the proposed SEI optimal and optimal CCCV strategies, respectively. The proposed algorithm guarantees that the optimal approach can give the bounded output as far as

Table 4.2: Overall computational times of optimal CCCV and proposed SEI optimal charging strategies at different current rates

Current Upper Bound (I_{max})	CCCV (s)	NMPC (s)
1 C (2.3 A)	242	285
2 C (4.6 A)	132	164
3 C (6.9 A)	54	78
4 C (9.2 A)	39	58

SEI film resistance is concerned. Figures 4.7 and 4.9 explains that under low charging times (or high charging current) there is no decrement in SEI film resistance.

Another critical aspect of online control strategies is computational time. Although the proposed NMPC successfully minimises the SEI layer resistance, it must be practically implementable. Computational times of both optimal and CCCV methodologies are presented in Table 4.2 at different maximum current upper bounds using MATLAB R2016b on DELL laptop with intel (R) Core (TM) i-7-8650U CPU @ 1.90GHz 2.11 GHz processor. A 2.3 Ah A123 26650 lithium iron phosphate (LFP) is used. The simulations of optimisation problems (3.25) and (3.31) are conducted using 4 collocation points, same SPM model and a prediction horizon of 200 seconds. Moreover, a more significant range of SOC (10% to 96%) is considered to evaluate the full charging process. Overall computational time is defined as the time taken by an algorithm to charge the battery from initial to final SOC. The overall computational times of optimal CCCV and the proposed SEI optimal strategies at 1C rating are 242 and 285 seconds, respectively. The percentage difference in computational times between both strategies tends to increase as the current rate increases. The higher current decreases the simulation time, keeping all other parameters constant. At 1C, the difference in computational time between both strategies is 43 seconds. The difference keeps on decreasing as current upper bound increases, 19 seconds at 4C. As computational time difference between two strategies is not significant; it can be concluded that the proposed SEI optimal charging strategy is suitable for real-time implementation in BMSs.

The summary of the comparison of proposed methodolgy (NMPC) to benchmark approach (CCCη) [86] is shown in Table 4.3.

Table 4.3: Comparison of the proposed strategy to the benchmark approach

	CCCη	**NMPC**
Battery state eqs.	Linear	Linear
Battery output eqs.	Non-linear	Non-linear
Lithium plating	Yes	Yes
SEI model	No	Yes
Solution approach	MPC	MPC
Reduction in SEI layer (Compared to CCCV, $I_{max} = 1C$)	0%	61%
Reduction in SEI layer (Compared to CCCV, $I_{max} = 4C$)	0%	24%
Side reaction overpotential	zero	positive
Evaluating computational time	No	Yes

4.2 Optimal Charging: mechanical degradation

This section employs an approach to model the mechanical degradation effects solely based on the SEI layer formation. As mentioned, the fracture of active material is less significant than SEI layer damage. Hence, the SEI repair and break effects have been considered the main ageing mechanisms that influence the capacity fade. A unique contribution is the formulation of a non-linear model predictive control (NMPC) framework, which considers the effects of mechanical degradation. A dynamic model predicts the future instances of the controlled plant by optimising the performance cost. The cost of the problem is defined in terms of states and input arrays. Receding horizon approach is used to optimise the control actions at every sampling instance. Physics-based constraints handling throughout the charging process is the critical element for the proposed strategy. The optimisation results of the NMPC framework are compared with the traditional CCCV approach. The results of the proposed strategy are also compared with experimental results published in [78].

4.2.1 Results and Discussion

The proposed optimal strategy does not consider the effect of voltage on the Young's modulus, assumed to be constant throughout the charging process. Moreover, stress (radial or tangential) is zero in the case of an empty particle (zero concentration). The proposed algorithm is shown in Figure 4.10. Fresh battery cell undergoes a formation cycle, resulting an initial SEI layer on the surface of graphite. In each battery cycle (charging and discharging), optimiser runs for charging only. After the charging process, algorithm runs for constant current discharging. Amplitude stress can be estimated in each cycle by the DISs generated in charging and discharging. The voltage check is performed before each cycle to maintain a constant level. The NMPC strategy is implemented with the initial state of charge (SOC) as 0.4. At the same time, maximum current upper bounds vary from 0.5 C to 4 C. Reference SOC, SOC_{ref} is taken as 0.90, and the maximum voltage must not exceeds 4.2 volts. Problem (3.32) runs from initial time ($t = t_0$) to final time ($t = t_f$) , when SOC of battery reaches the predefined value. The solver predicts the future instances with a prediction horizon of 150 s using four collocation points. The solution of the current time step is the initial guess of next time instant. After tuning the control parameter at different values and to varying constraints, a general optimal charging profile can be obtained to successfully minimise the damage to the batteries. Post-processing calculations are done for each profile (optimal or CCCV) which will be discussed further.

Table 4.4: Results of parameters

Current Upper Bound	Critical Current	t_d	t_s	Charging times (s)	
U_{max}	x ($U_{cr} = x * U_{max}$)	(% of T_c)	(% of T_c)	Optimal T_c	CCCV
0.5 C	0.3	15	89	4962	4482
1C	0.36	12	91	2602	2240
1.5 C	0.40	11.3	92.6	2079	1749
2 C	0.45	10.5	93.5	1442	1200
2.5 C	0.49	9.7	94.1	1216	1006
3 C	0.53	8.8	94.3	1085	905
3.5 C	0.55	6.2	94.7	1010	860
4 C	0.56	5.7	95.1	954	834

Figure 4.11 shows the benchmark constant current constant voltage (CCCV) and

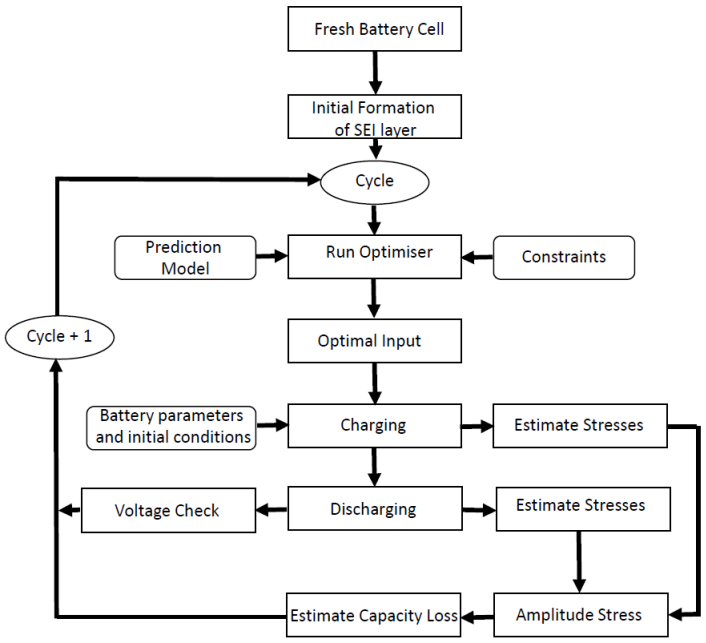

Figure 4.10: Proposed Algorithm to minimise SEI layer considering mechanical degradation

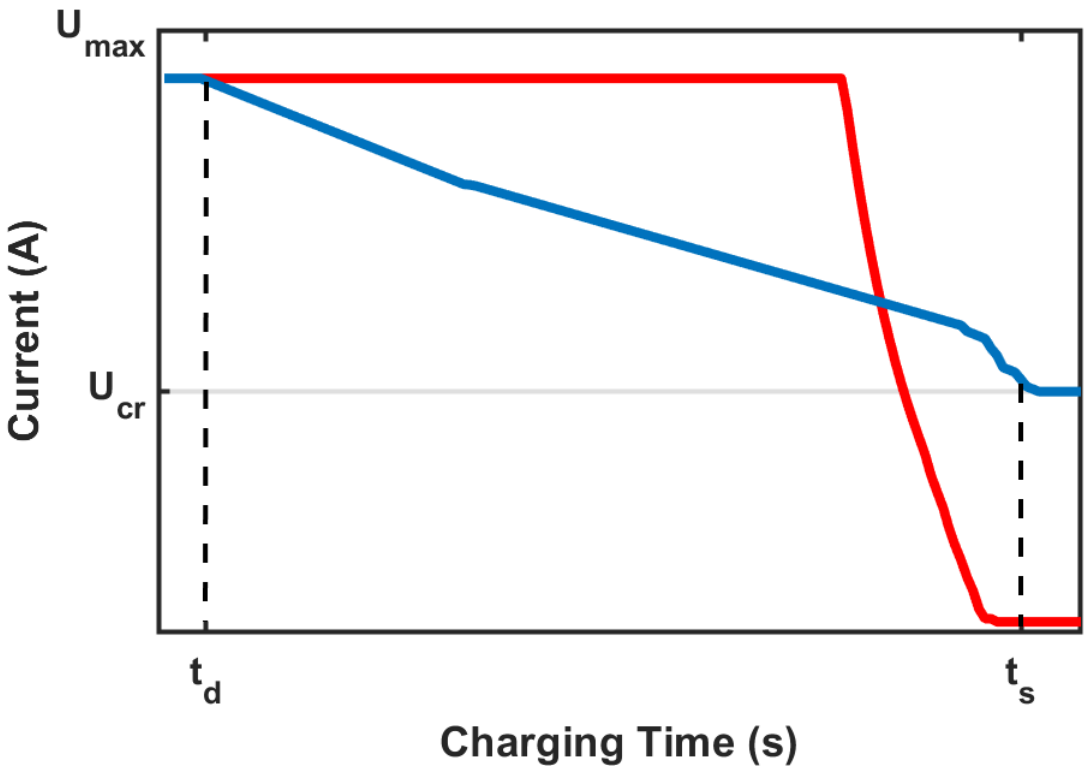

Figure 4.11: Proposed charging profile considering mechanical degradation

the proposed optimal charging profiles. In CCCV strategy, constant current is applied to the battery until battery achieves the voltage limit. Afterwards, it runs on a constant voltage scheme in which current keeps on decreasing to a lower predefined limit. In the proposed optimal strategy, charging is carried out at maximum current

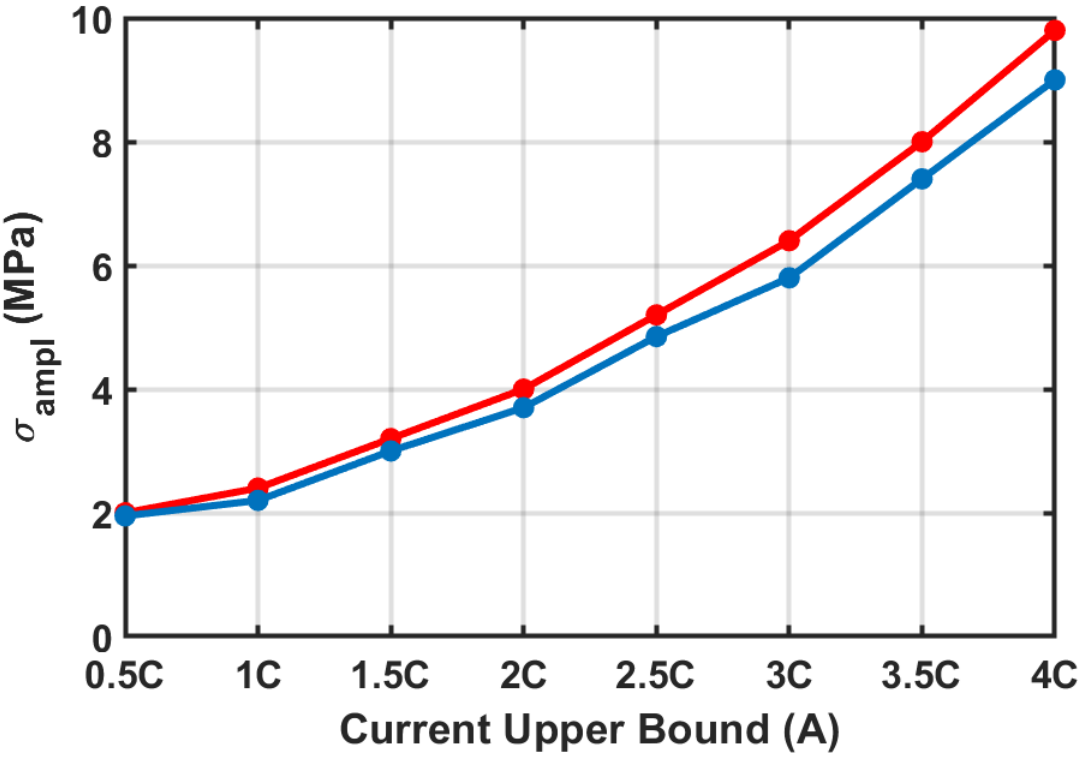

Figure 4.12: Amplitude stress versus maximum current upper bound, Optimal CCCV charging(–), Proposed SEI optimal charging(–)

for a certain period and then it decreases to a critical current level (U_{cr}). As σ_{ampl} is the key variable in analysing cyclic life, it means maximum and minimum stresses need to be evaluated for each cycle. The studies [78, 79] shows that maximum stress reaches around 50% mean SOC while minimum stress is normally found when the battery is empty or at a low concentration level. The proposed strategy uses the small current to minimise the peak stress. t_d and t_s are the time instances of decrement and settling currents respectively. Table 4.4 tabulates charging times, U_{cr},t_d and t_s. The critical current decreases as the maximum current upper bound increases. The decrement current, t_d decreases as current upper bound increases because battery charges more rapidly at higher current rates. However, the settling current, t_s is directly proportional to current upper bound. Optimal and CCCV charging times are also shown in Table 4.4. It is necessary to investigate the effects of σ_{ampl} on charging process to avoid fracture. Figure 4.12 shows the relationship between σ_{ampl} and maximum current upper bound ($0.5C$-$4C$). The percentage difference in σ_{ampl} between CCCV and optimal profiles is evident; with minimum percentage difference of 2.5 % at 0.5 C while 8.9% is recorded at 4 C. Figure 4.13 shows the relationship

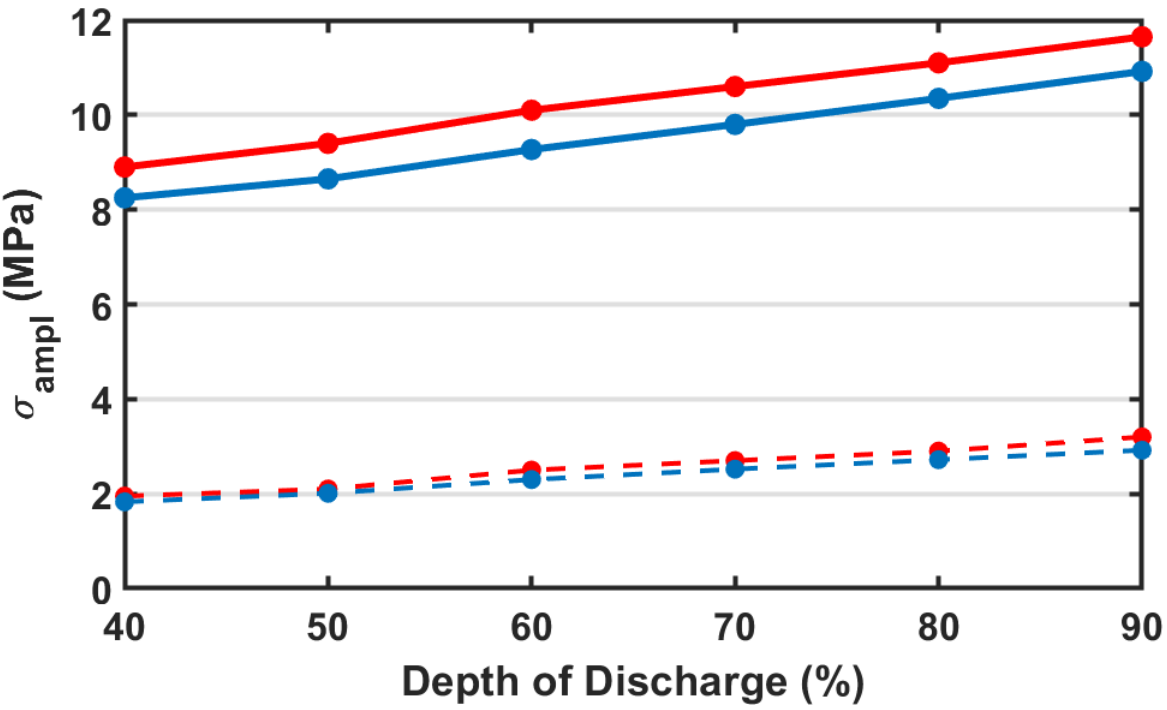

Figure 4.13: Relationship between amplitude stress and depth of discharge, Optimal CCCV charging(–), Proposed SEI optimal charging(–)

between stress amplitude and various depth of discharge (DOD) levels at different charging current rates. It is a known fact that current rate is directly proportional to σ_{ampl}. However, what happens when DOD levels vary? As the DOD level increases, σ_{ampl} also increases. Proposed optimal profile successfully decreases the σ_{ampl} at every DOD level.

Table 4.5: Mean state of charge data

SOC_{mean}	SOC_i	SOC_{ref}	ΔDOD
50	0	100	100
	25	75	50
	40	60	20
	45	55	10
	47.5	52.5	5
90	80	100	20
	85	95	10
75	65	85	20
	70	80	10
25	15	35	20
	20	30	10
10	0	20	20
	5	15	10
95	90	100	10

4.2.2 Comparison between the proposed strategy and experimental data

The proposed NMPC framework results are compared with the experimental results presented in [78]. It was assumed that the SEI break/repair effect is the primary source of loss of lithium ions. Figure 4.14(a) shows the total capacity loss versus DOD for the experimental and proposed optimal scenarios. Experimental results show an exponential increase with the DOD at 50% mean SOC. There is a trivial difference as far as low DOD levels are concerned. However, the percentage difference of 11% between two results is recorded in case of 100% DOD. In order to validate the proposed strategy, simulations have been carried out under the same conditions as the experiments are performed. Figure 4.14(b) shows the maximum tangential stress in the SEI at 100% DOD during a cycle of charging/discharging. In the simulation,

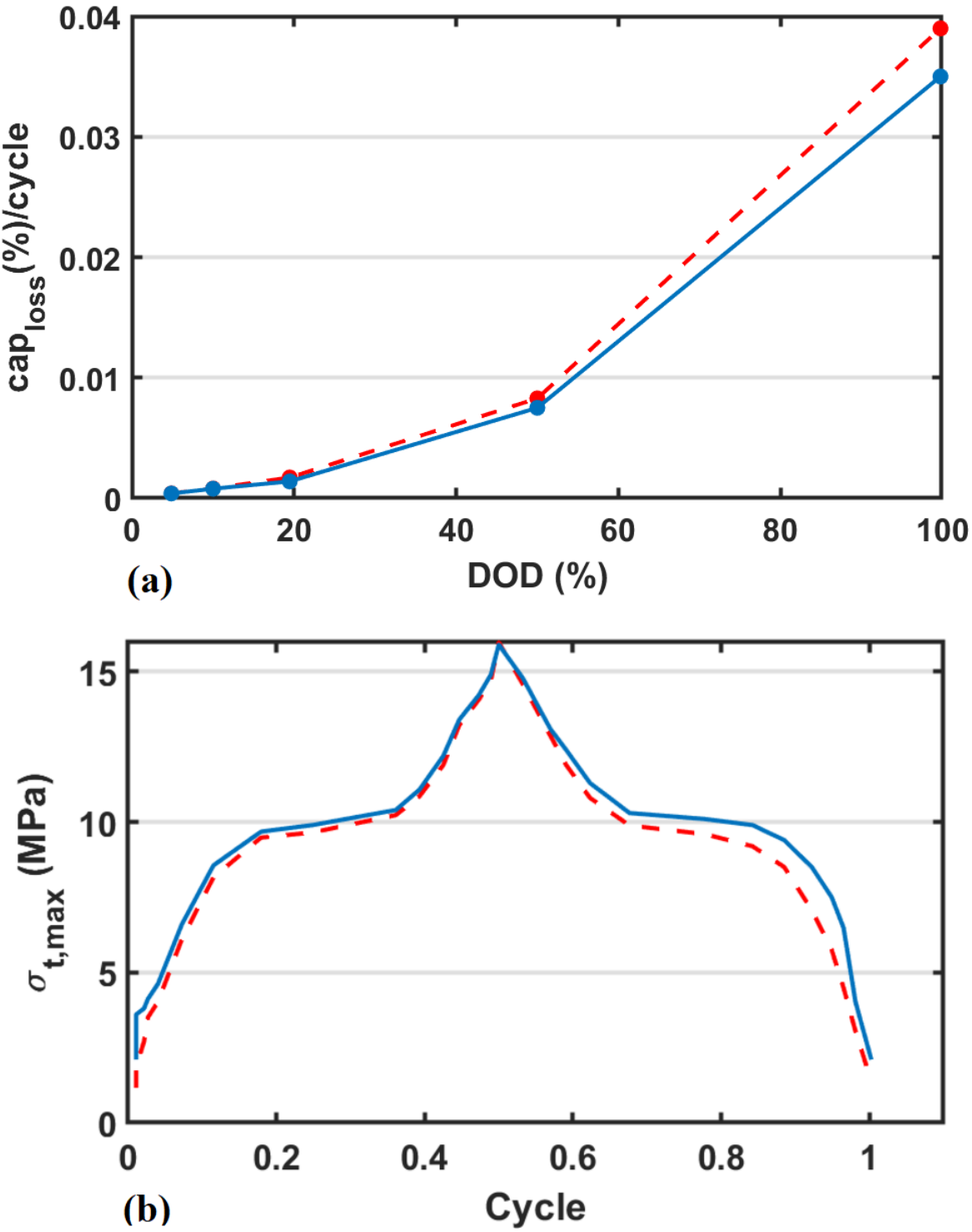

Figure 4.14: Comparing experimental and optimal results. (a) Capacity loss versus DOD at 50% SOC_{mean}, (b) Maximum tangential stress in a charging/discharging cycle- Experiment (–), Proposed SEI optimal charging(–)

50% SOC_{mean} has been maintained with varying DOD. Detail of SOC_{mean} is given in Table 4.5. It can be noted from Figure 4.14(b) that maximum stress in an optimal scenario is slightly less than the experimental case. At any point in the cycle, the maximum stress in an optimal case is lower than that of experimental results. Rela-

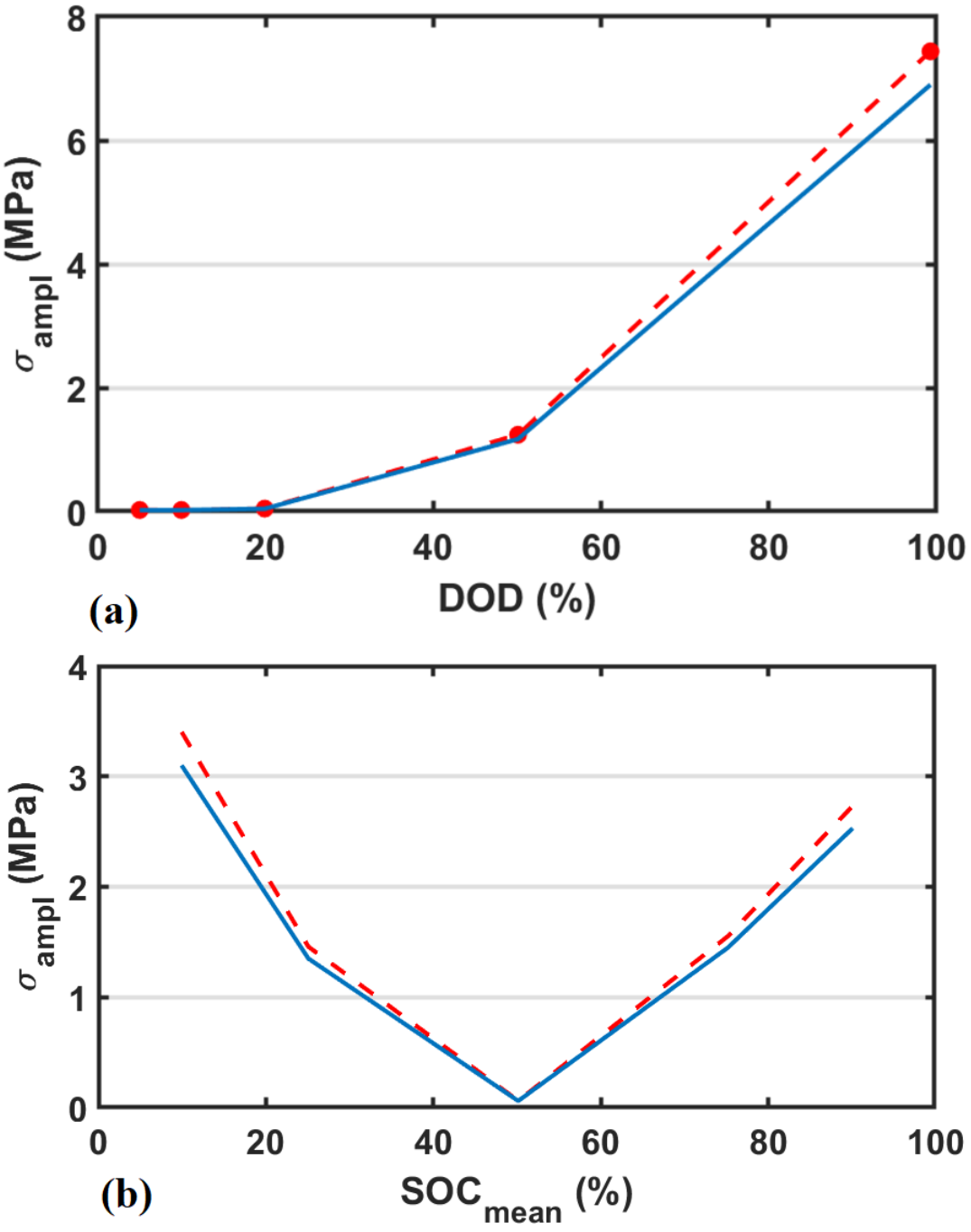

Figure 4.15: Comparing experimental and optimal results. (a) Relationship between stress amplitude and DOD, (b) Stress amplitude versus SOC_{mean} -Experiment (–), Proposed SEI optimal charging(–)

tionship between stress amplitude and depth of discharge is shown in Figure 4.15(a). There is no difference recorded at 5, 10, 20 and 50% DOD. The maximum difference is recorded at 100% DOD, which is 6.9 MPa and 7.4 MPa in optimal and experimental scenarios respectively. At higher DOD level, battery cycles show larger stress oscillations, led to bigger SEI damage. Figure 4.15(b) shows the relationship between stress amplitude and depth of discharge at different mean SOCs (20% DOD) for both

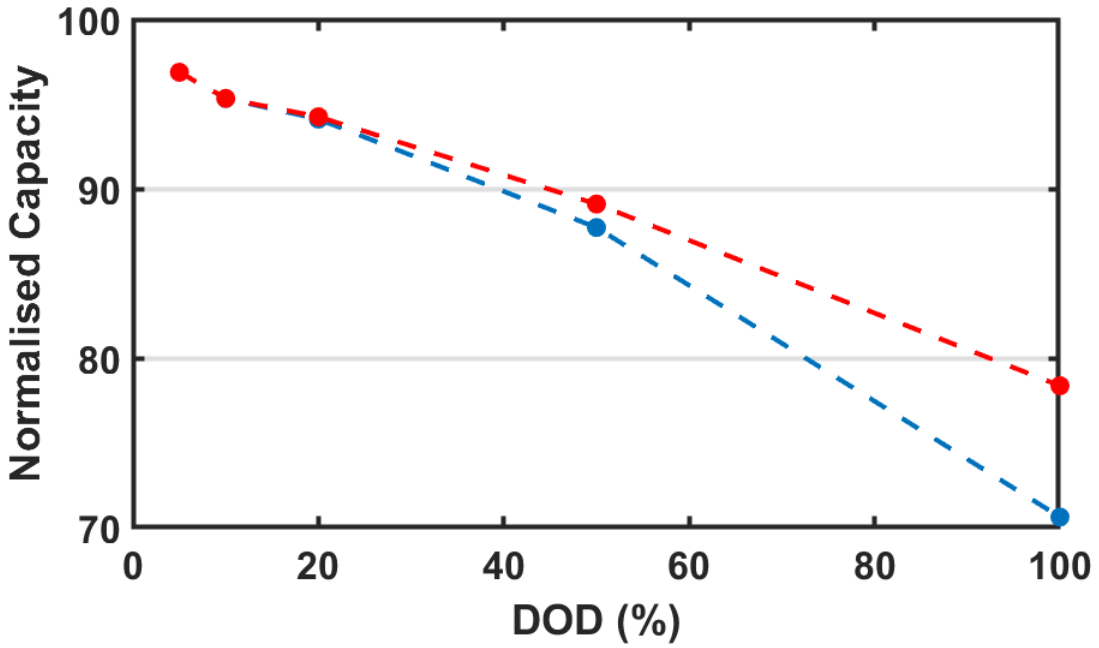

Figure 4.16: Comparison of normalised capacity versus depth of discharge (DOD) after 750 full cycles-Experiment (–), Proposed SEI optimal charging(–)

optimal and experimental scenarios. There is no difference in values recorded as far as 50% mean SOC is concerned. The higher differences between simulation and experiment are noted at 10% and 90% mean SOCs. It is understandable because at 50% SOC_{mean}, graphite expansion is minimum. It causes less SEI damage than 10% and 90% SOC_{mean} values. The influence of DOD on the ageing of battery material is compared in experimental and optimal scenarios. Simulations are done for 750 cycles, at 50% SOC_{mean} and average voltage of 3.7 volts (Figure 4.16). The capacity fade behaves linearly with different levels of DOD. The proposed optimal methodology minimises the degradation effect, but there is no significant difference recorded at 5%, 10% and 20% DOD. The optimal results show some improvements at 50 and 100 % DOD, with percentage differences of 2.3% and 10.4%, respectively.

The summary of the comparison of proposed methodology (NMPC) to diffusion induced stress (DIS) [78] approach is shown in Table 4.6.

Table 4.6: Comparison of the proposed strategy to the experimental approach

	DIS	**NMPC**
Single particle model	Yes	Yes
SEI model	DIS based model	DIS based model
Ageing	cyclic	cyclic
Weakest material	SEI	SEI
Capacity loss/cycle (%)	0.035	0.039
Normalised capacity (750 cycles)	79	70

Chapter 5

Computational Efficiency of Differential Flatness over Pseudo-spectral Methods

5.1 Introduction

This chapter proposes an optimal charging profile by applying a non-linear model predictive control (NMPC) strategy on a temperature-dependent battery model along with chemical degradation. This chapter can be seen as an extension of control problem in Section 3.4, where temperature effects are not accounted for. The main contribution compared to previous work circles around two points: (*i*) temperature is not constant; instead, it changes in every sampling instant, and (*ii*) the differential flatness method is applied to examine its computational benefits over pseudo-spectral control. The results from the optimal control strategy are compared with a standard constant current constant voltage (CCCV) strategy.

The first change compared to Section 3.4 is the selection of the electrochemical model. Instead of the SPM, this chapter adopts an extended version of SPM with thermal effects [285]. This thermal electrochemical SPM with temperature dynamics (SPM-T) has non-linear diffusion and thermal processes, both of which are coupled [286]. This makes the control more challenging, and constraints (voltage, current, side reaction overpotential and temperature) are challenging to handle. Maximum temperature (or

rise in temperature) control is an additional aspect of the proposed control strategy in this chapter. To limit the degradation speed, temperature rise can be part of an objective function along with the thermal model [270]. Some researchers try to reduce degradation rates and enhance safety by imposing constraints on temperature [271], which can also minimise the effects of side reactions, such as lithium plating [272]. However, achieving lower capacity fade is optimistic thinking because side reactions do increase at higher temperatures [6]. Hence, it is challenging to propose a generalised approach to fast-charge the battery by controlling the temperature alone.

The degradation mechanisms considered in this chapter are SEI and lithium plating [239]-[244]. The main aim is to investigate the effects of temperature on the degradation mechanisms. Researchers explain the dependency or linking of C-rates with temperatures in [273, 274]. At low charging rates, the degradation rate increases slowly, typically from 10°C to 60°C [273]. However, the degradation rate is directly proportional to the inverse of temperature at 25 °C around 1 C, and constant in a range of 25°C to 70°C [274]. The main reason for this outcome is due to the formation of particle deposits caused by lithium plating at room temperature [274]. However, the degradation rate is directly proportional to the charging rates keeping the temperature constant or otherwise [273, 274]. For example, battery degradation rate is lower at 45°C than at 25°C, at slightly higher current rate (2 C) [275]. The degrdation mechanisms considered are dissolution of transition metal atoms, surface morphology and enhanced carbonate ratios in surface SEI [275]. It is expected that battery will deteriorate more rapidly above 45°C at any current rate [276]. Hence, an optimal charging profile that minimises the degradation process by actively controlling the temperatures is needed.

A range of researchers proposed charging methods on temperature-dependent battery model control techniques with various objective functions, optimisation methods, side reactions, and most importantly, temperature [93]-[98]. The objective function in most of the cases is the combination of two variables [105]-[112]. One is charging time, and others are often temperature or side reactions rates [149]-[151]. SPM [1] or P2D [55] models with add-on ageing models are used for optimisation purposes. In the past decade, Pontryagin's minimum principle [277], the dynamic programming technique

[278], the Legendre-Gauss-Radau pseudo-spectral method [279], the extended differential flatness approach [86], the interior-point optimiser [280], Reference Governor (RG) [123], and model predictive control (MPC) [281] are the optimisation methods proposed by different researchers. RG [2, 123] and MPC [88]-[92] are the only methods which can be used for online applications. Due to the non-generalised behaviour of the RG model, MPC is the preferred solution for online optimisations [87]-[104]. In this chapter, we use a NMPC framework along with Gauss pseudo-spectral control to optimise the charging trajectory, which decreases the thickness of the SEI layer and also operates the battery in a healthy regime.

Computational efficiency is one of the main challenges in online applications [179]. Chapter 4 shows that the proposed optimisation strategy takes more time than the benchmark CCCV methodology. This is quite understandable as the proposed strategy needs to do more work with an additional term in the objective function and one more constraint to check in every sampling instant. It is expected that the computational time difference between proposed and benchmark strategies is quite high, as the prediction model needs to change at each time instant. The differential flatness technique is used in this work to improve computational efficiency [282]. Fick's law governs the diffusion dynamics in an electrode of the lithium-ion battery, and it is known to be differentially flat [283]. The concept is to use a single variable as flat output instead of considering all state and input variables. Hence, one flat output is enough to model the dynamics of an electrode. However, the flat output of the second electrode is the function of the first electrode [284]. We use this already advanced technique with the pseudo-spectral method to reduce the degradation effects.

The remainder of this chapter is organised as follows. The incorporated thermal effects in SPM and model reformulation are discussed in Section 5.2. Section 5.3 describes the definition, application and mathematical formulation of differential flatness. Section 5.4 formulates the control problem. Results are discussed in Section 5.5 with subsection 5.5.1 discusses the computational efficiency of proposed algorithm using differential flatness and pseudo-spectral approaches.

5.2 Thermal single particle model (SPM-T)

5.2.1 Distinction from SPM

The SPM-T share same equations as of SPM i.e. (2.1)-(2.18), except that all are temperature-dependent. The diffusion coefficient, reaction rate constant, and cell resistance need to be re-computed at every sampling interval. The electrochemical parameters , reference potential curves, and thermal parameters are found in [285, 286]. According to Arrhenius equation, diffusion coefficient $D_{s,i}(t)$ and reaction rate constant $k_i(t)$ are expressed as:

$$D_{s,i}(t) = D_{s,i}^{ref}\ exp\left(\frac{Ea_{D,i}}{R}\left(\frac{1}{T(t)} - \frac{1}{T_{ref}}\right)\right) \tag{5.1}$$

$$k_i(t) = k_i^{ref}\ exp\left(\frac{Ea_{k,i}}{R}\left(\frac{1}{T(t)} - \frac{1}{T_{ref}}\right)\right) \tag{5.2}$$

where $D_{s,i}^{ref}$ and k_i^{ref} are the diffusion coefficient and reaction rate constant at reference temperature, respectively. Activation energies of diffusivity and reaction rate is symbolised as $Ea_{D,i}$ and $Ea_{k,i}$ respectively. Thermal dynamics of lithium-ion batteries can be expressed as:

$$mC_p\dot{T}(t) = -hA\big(T(t) - T_{ref}(t)\big) + I(t)T(t)S + I(t)\big(\eta_p(t) - \eta_n(t) + I(t)R_{cell}\big) \tag{5.3}$$

where S, battery entropy coefficient ,is defined as :

$$S = \left(\frac{\partial U_p}{\partial T}\big(SOC_p^{surf}(t)\big) - \frac{\partial U_n}{\partial T}\big(SOC_n^{surf}(t)\big)\right) \tag{5.4}$$

The term $\frac{\partial U_i}{\partial T}\big(SOC_i^{surf}\big)$ is the entropy coefficient for electrode i. The thermal mass is represented as mC_p in (5.3), h is the convection heat transfer coefficient and A is the cell surface area. Thermal model is the sum of three terms, represent convection from battery's surface to surroundings, reversible heat generation term and irreversible heat component due to ohmic losses.

5.2.2 Model reformulation

Partial differential equations govern Fick's law of diffusion. It needs to be discretised into ordinary differential equations, as shown in section 2.2. The main difference is the use of Chebyshev polynomials instead of Legendre polynomials [70]. Also, the resulting state-space model is temperature-dependent. This makes the SPM-T highly non-linear. The state-space representation for any electrode is

$$\dot{x^*}_i(t) = A_i(T)x_i^*(t) + B_i(T)I(t) \tag{5.5}$$

where A_i and B_i are the state and input matrices respectively, while $x^* \epsilon \mathbb{R}^{3\times1}$ and I is the input current. The state and input matrices are functions of temperature in (5.5) due to temperature -dependent diffusion coefficient. The state variables representing full cell dynamics is expressed as:

$$x^*(t) = [x_n^*(t), x_p^*]^T \tag{5.6}$$

The final state matrix can be of the form

$$A(t) = \begin{bmatrix} A_n(T) & \mathbf{0} \\ \mathbf{0} & A_p(T) \end{bmatrix} \tag{5.7}$$

where $\mathbf{0}$ is a 3×3 matrix of zeros. The input matrix is formulated as:

$$B(t) = \begin{bmatrix} B_n(T) \\ B_p(T) \end{bmatrix} \tag{5.8}$$

There is also an additional variable i.e. temperature T, which describes the thermal cell dynamics. Therefore, the state vector is

$$x(t) = \begin{bmatrix} x^*(t) \\ T(t) \end{bmatrix} \tag{5.9}$$

The input vector also contains another variable, reference temperature:

$$u(t) = \begin{bmatrix} I(t) \\ T_{ref}(t) \end{bmatrix} \tag{5.10}$$

The state space representation of the full SPM-T model is expressed as

$$\dot{x}(t) = f\Big(x(t), u(t)\Big) \tag{5.11}$$

$$y = g\Big(x(t), u(t)\Big) \tag{5.12}$$

5.3 Differential flatness

Differential flatness is an enticing tool to optimise charging trajectory with reasonable computational efficiency. It gives the projection of solid-phase concentrations by considering only the centre point concentration at any time instant [80, 284]. This section will be composed of the definition of differentially flat systems, the application to batteries, and the final mathematical formulation of the control problem.

5.3.1 Definition

There must be a distinct variable, the flat output z, which makes the system differentially flat. It must have following properties.

1. states and inputs can be interpreted in terms of flat output and its derivatives.

$$x = f_x(z, \dot{z}, ..., z^{\alpha}) \tag{5.13}$$

$$u = f_u(z, \dot{z}, ..., z^{\beta}) \tag{5.14}$$

2. Similarly flat output can be written in terms of states, input and input's derivatives.

$$z = f_z(x, u, \dot{u}, ..., u^{\gamma}) \tag{5.15}$$

where α, β, γ are constants that depends on individual system [85]. The number of inputs to the system must be equal to dimension of the flat output vector z.

5.3.2 Application to batteries

The dynamics of lithium-ion batteries contemplates differentially flat by comparing it to heat dynamics [85]. [284] proved that one-dimensional linear diffusion heat equation is a subset of Fick's law of diffusion, thus battery dynamics is flat. Differential flatness can be interpreted as a tool to control non-linear systems. A linear system must be controllable to be differentially flat [284]. Hence, the diffusion dynamics in anode or cathode is controllable. Moreover, one flat output is required to optimise the charging trajectory. All the other states and input variables can be manipulated algebraically using the flat output and its derivatives.

The dynamics of the state-space represented by the model(2.25) can be reformulated into controllable canonical form. The definition of differential flatness (5.13-5.15) suggests that there must be one flat output for each electrode. The canonical form of (2.25) in any electrode i is expressed as:

$$\dot{x}_i^-(t) = \begin{bmatrix} 0 & 1 & 0 \\ 0 & 0 & 1 \\ -\alpha_{1,i} & -\alpha_{2,i} & -\alpha_{3,i} \end{bmatrix} x_i^-(t) + \begin{bmatrix} 0 \\ 0 \\ 1 \end{bmatrix} u(t) \tag{5.16}$$

where $\alpha_{j,i}$ are the coefficients of transformed state vector for the electrode. State x can be defined as

$$x_i(t) = M_i \, x_i^-(t) \tag{5.17}$$

The matrix M_i is the similarity transformation matrix to compute state vector. However the flat output, in this scenario, is defined as:

$$z(t) = x_1^-(t) \tag{5.18}$$

The states can be algebraically computed from the flat output and its derivatives.

$$x(t) = M\left(\begin{bmatrix} 1 & 0 & 0 \\ 0 & 1 & 0 \\ 0 & 0 & 1 \end{bmatrix}\begin{bmatrix} z(t) \\ \dot{z}(t) \\ \ddot{z}(t) \end{bmatrix}\right) \tag{5.19}$$

Similarly, input can be written as:

$$u(t) = \begin{bmatrix} -\alpha_1 & -\alpha_2 & -\alpha_3 & 1 \end{bmatrix}\begin{bmatrix} z(t) \\ \dot{z}(t) \\ \ddot{z}(t) \\ \dddot{z}(t) \end{bmatrix} \tag{5.20}$$

This completes the application of differential flatness property to depict the dynamics of any electrode using one flat output.

5.3.3 Flatness with Gauss pseudo-spectral method

Gauss pseudo-spectral method is discussed in detail in section 3.2. The main objective of the direct transcription method is to transform the non-linear and non-convex problems into non-linear programming problems that can be easily solved using various algorithms. Mapping of time is done by eq. (3.1). The flat output z_i is approximated as:

$$z_i(\tau) \approx z_i(\tau) = \sum_{k=0}^{N} L_k(\tau)\mathbf{z}_i(\tau_k) \tag{5.21}$$

where $z_i(\tau)$ is the flat output in terms of collocation points and $L_k(\tau)$ is the Lagrange polynomial. Using the property of Lagrange polynomials, flat output must be:

$$\mathbf{z}_i(\tau_k) = z_i(\tau_k) \tag{5.22}$$

derivatives of flat output can be computed analytically i.e. by differentiating (5.21). It can be expressed mathematically as:

$$\mathbf{z}_i^{(j)}(\tau_i) = \sum_{k=0}^{N} L_k^{(j)}(\tau_i)\ \mathbf{z}_i(\tau_k) \tag{5.23}$$

where $L_k^{(j)}(\tau_i)$ represents the i^{th} derivative of Lagrange polynomial and can be expressed, using differentiation matrix, as

$$D_j(i,k) = L_k^{(j)}(\tau_i) \tag{5.24}$$

Therefore, the j^{th} derivative of the flat output (5.23) can be expressed as

$$Z_i^{(j)} = D_j \; Z_i \tag{5.25}$$

where $Z_i = [\mathbf{z}_i(\tau_0), \mathbf{z}_i(\tau_1), \mathbf{z}_i(\tau_2), ..., \mathbf{z}_i(\tau_N)]^T$ and $Z_i^{(j)}$ is a vector of derivatives. If a state is expressed as $X_{i,k} = [x_{i,k}(\tau_1), x_{i,k}(\tau_2), ..., x_{i,k}(\tau_N)]^T$, then state variables can be expressed as:

$$X_{i,1} = Z_i, \quad X_{i,2} = D_1 \; Z_i \quad X_{i,3} = D_2 \; Z_i$$

5.3.4 Mathematical formulation of differential flatness of SPM-T

In a SPM, one flat output is required to depict the dynamics of the electrode. However, in SPM-T model, two flat outputs are needed to represent the electrochemical and thermal dynamics. This is because, in differential flatness, number of inputs must be equal to the number of flat outputs. Therefore, one flat output represents the diffusion dynamics, and second flat output represents thermal dynamics. Note that both diffusion and thermal dynamics are not independent. The first flat output is

$$z_1(t) = x_{n,1}^-(t) \tag{5.26}$$

The second flat output is the bulk temperature T,

$$z_2(t) = T(t) \tag{5.27}$$

Therefore, the flat output vector for the thermal model is

$$z(t) = \begin{bmatrix} x^{-}_{d,n,1(t)} \\ T(t) \end{bmatrix} \tag{5.28}$$

State variables $x_{d,i}$ can be computed from flat output and its corresponding derivatives.

$$x^{-}_{d,i}(t) = \begin{bmatrix} 1 & 0 & 0 \\ 0 & 1 & 0 \\ 0 & 0 & 1 \end{bmatrix} \begin{bmatrix} z_1(t) \\ \dot{z}_1(t) \\ \ddot{z}_1(t) \end{bmatrix} \tag{5.29}$$

The original state variables $x = [x_{d,i}, T]^T$ can be written as:

$$\begin{bmatrix} x_{d,i}(t) \\ T(t) \end{bmatrix} = \begin{bmatrix} M_i(z_2(t))\ x^{-}_{d,i}(t) \\ z_2(t) \end{bmatrix} \tag{5.30}$$

where $M_i(z_2(t))$ is the similarity matrix, which transforms the transformed state variables into original form.

Similarly, the input vector can also be written in terms of two flat outputs. In SPM-T, current and ambient temperature are two inputs. The input current u_1, can be mathematically expressed as

$$u_1(t) = \begin{bmatrix} -\alpha_{i,1}(z_2(t)) & -\alpha_{i,2}(z_2(t)) & -\alpha_{i,3}(z_2(t)) & 1 \end{bmatrix} \begin{bmatrix} z_{i,1}(t) \\ \dot{z}_{i,1}(t) \\ \ddot{z}_{i,1}(t) \\ \dddot{z}_{i,1}(t) \end{bmatrix} \tag{5.31}$$

The coefficients $\alpha_{i,j}$ also change with temperature $z_2(t)$. The second flat output can be expressed as:

$$u_2(t) = \frac{1}{hA}\Big(mC_p\dot{z}_2(t) - u_1(t)u_2(t)S(t) - u_1(t)\big(\eta_p(t) - \eta_n(t) - u_1(t)R_{cell}\big)\Big) + z_2(t) \tag{5.32}$$

where the entropy coefficient S and overpotential $\eta_i(t)$ can be expressed using $z_2(t)$.

5.4 Problem formulation

The main idea is to optimise charging trajectory along-with minimising solid electrolyte interface (SEI) layer resistance. An optimal charging problem is presented to validate the concept. The side reaction due to lithium plating is also incorporated in the optimisation problem. Mathematically it can be written as:

$$
\begin{aligned}
&\underset{z_n(t)}{\text{minimize}} \quad \int_{t_o}^{t_f} \Big[\big(SOC_n(t) - SOC_{ref}\big)^2 + q\ R^{'}_{film}(t) \Big] dt \\
&\text{subject to} \\
&x(t) = f_x\big(z(t), \dot{z}(t), ..., z^{\alpha}(t)\big), \\
&u(t) = f_u\big(z(t), \dot{z}(t), ..., z^{\beta}(t)\big), \\
&z(t) = f_x\big(x(t), u(t), \dot{u}(t), ..., u^{\gamma}(t)\big), \\
&SOC_n(t) = \frac{c_{s,n,avg}(t)}{c_{s,n,max}}, \\
&SOC^{surf}(t) = \frac{c_s^{surf}(t)}{c_{s,max}}, \\
&c_{s,avg} = \int_0^R c_s\ dr, \\
&c(r,t) \approx \sum_{i=0}^{M} \beta_i(t)\ \phi_i(r), \\
&J(t) = i_0(t) \left[exp\bigg(\frac{\alpha_a F}{RT} \eta(t) \bigg) - exp\bigg(-\frac{\alpha_c F}{RT} \eta(t) \bigg) \right], \\
&\eta_{sr}(t) = \eta_n + U_n(SOC_n^{surf}(t)), \\
&0 \leq I(t) \leq I_{max}, \\
&0 \leq V(t) \leq V_{max}, \\
&T_{min} \leq T(t) \leq T_{max}, \\
&\eta_{sr} \geq 0
\end{aligned}
\tag{5.33}
$$

where q is the control parameter, $R^{'}_{film}(t)$ is the time rate change of SEI film resistance, SOC_{ref} is reference state of charge (SOC), η_{sr} is the side reaction overpotential, I_{max} and V_{max} are the maximum current and voltage, respectively. Using equation (2.7),

SOC in negative electrode can be written as

$$SOC_n(t) = \frac{\phi_0(r)z_n(t) + \phi_2(r)D_1z_n(t) + \phi_4(r)D_2z_n(t) + \phi_6(r)\beta_6(t)}{c_{max,n}} \tag{5.34}$$

$R^{'}_{film}(t)$ is function of intercalation and side reaction overpotentials in negative electrode (2.33). It can be ref-formulated as:

$$\begin{aligned} R^{'}_{film}(t) = P \times \ exp\Bigg\{ - \left(\frac{R_{gas}T}{2F}\right)\Bigg[\left(\frac{R_{gas}T}{F}\right) \\ \ln\Bigg(\frac{-I(t)}{A_nL_nk_n\sqrt{\phi_0(R)z_n(t) + \phi_2(R)D_1z_n(t) + \phi_4(R)D_2z_n(t) + \phi_6(R)\beta_6(t) - c_{max,n}}} \\ \frac{1}{\sqrt{\phi_0(R)z_n(t) + \phi_2(R)D_1z_n(t) + \phi_4(R)D_2z_n(t) + \phi_6(R)\beta_6(t)}\sqrt{c_e}}\Bigg) + \\ U_{n,ref}\left(\frac{\phi_0(R)z_n(t) + \phi_2(R)D_1z_n(t) + \phi_4(R)D_2z_n(t) + \phi_6(R)\beta_6(t)}{c_{max,n}}\right) - 0.4\Bigg]\Bigg\} \end{aligned} \tag{5.35}$$

where P is a constant. To compare the results with proposed optimal control problem, this chapter uses standard CCCV charging problem defined as follows

$$\begin{aligned} &\underset{I(t)}{\text{minimize}} \quad \int_{t_o}^{t_f} \left(SOC_n(t) - SOC_{ref}\right)^2 dt \\ &\text{subject to} \\ &\dot{x}(t) = A(T)x(t) + B(T)u(t), \\ &SOC_n(t) = \frac{c_{s,n,avg}(t)}{c_{s,n,max}}, \\ &SOC^{surf}(t) = \frac{c_s^{surf}(t)}{c_{s,max}}, \\ &c_{s,avg} = \int_0^R c_s \ dr, \\ &c(r,t) \approx \sum_{i=0}^{M} \beta_i(t) \ \phi_i(r), \\ &J(t) = i_0(t)\left[exp\left(\frac{\alpha_aF}{RT}\eta(t)\right) - exp\left(-\frac{\alpha_cF}{RT}\eta(t)\right)\right], \\ &0 \le I(t) \le I_{max}, \\ &0 \le V(t) \le V_{max}, \\ &T_{min} \le T(t) \le T_{max} \end{aligned} \tag{5.36}$$

NMPC strategy is used to optimise trajectory without differential flatness. The overall mathematical formulation of NMPC strategy is similar to one presented in section 3.3. One difference is use of temperature-dependent electrode dynamics (5.7) instead of (2.25).

5.5 Results and Discussion

The results of the problem (5.33) with differential flatness and Gauss pseudo-spectral are almost similar. A minute difference is seen at a high SOC due to numerical errors and can be ignored. The initial and reference SOCs are taken as 10% and 90% respectively. At every time instant, future responses are recorded using four collocation points with a prediction horizon of 100 seconds. The solution of the current time step is taken as an initial guess for the next time interval. The problems are solved in MATLAB using "*nlmpc*" function.

Figure 5.1 depicts the online optimal charging using SPM-T model with maximum

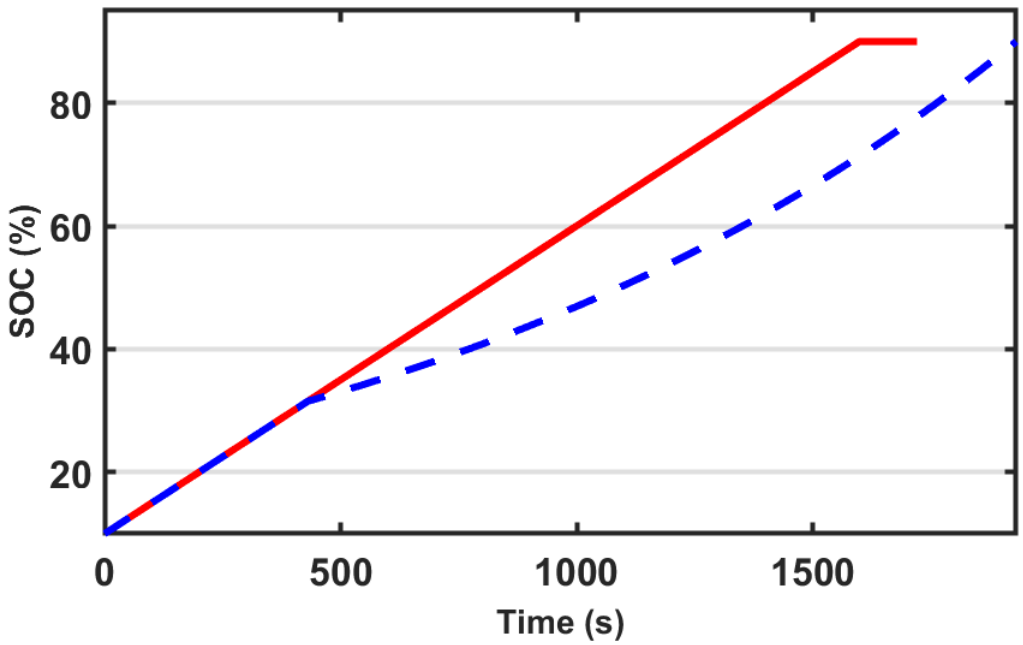

Figure 5.1: State of charge (SOC) in optimal and benchmark strategies ($U_{max} = 2C$)- Optimal CCCV charging(–), Proposed SEI optimal charging(–)

current of -4.4 A (2C). SOC profiles in both cases reach the desired goal but takes more time in case of optimal scenario. This is primarily because optimal charging needs to satisfy an additional constraint (lithium plating) and also needs to optimise

an extra term in objective function i.e. to minimise SEI film resistance. The temperature constraint is also added in this chapter. Due to this reason, overall charging time is increased.

It is necessary to analyse the current profiles in detail, to fully understand the be-

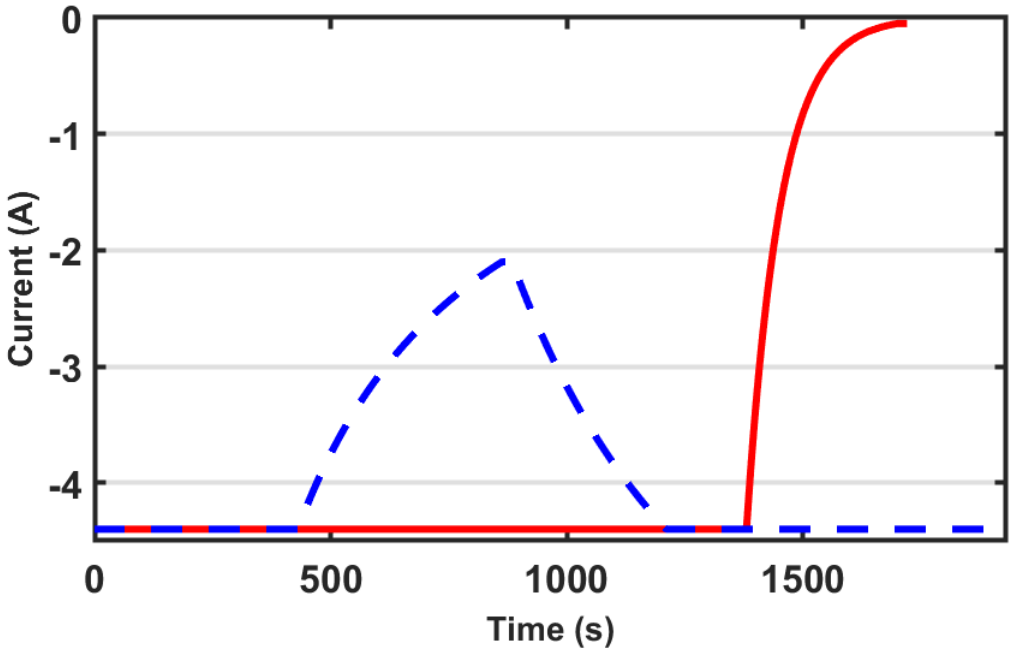

Figure 5.2: Current profiles at $U_{max} = 2C$- Optimal CCCV charging(–), Proposed SEI optimal charging(–)

haviour of SOC in both optimal and CCCV scenarios. In the case of CCCV, charging starts at constant current until a battery reaches to the maximum voltage limit, then it continues at a constant voltage to the pre-defined current limit. However, proposed optimal strategy starts with the constant current just like CCCV but relatively at low SOC, current drops to a minimum level (Figure 5.2). This high current is excellent as far as side reaction overpotential of lithium plating is concerned because overpotential is positive at high current even at low SOCs. SEI film resistance keeps on increasing at low SOCs using higher current. The exponential term in eq. (2.33), gives high values at low SOCs and low currents. Moreover, it must be noted that temperature is also changing in a certain defined range.

The profiles of SEI film resistance are shown in Figure 5.3 in both optimal and CCCV methodologies. It can be easily understood by simultaneously observing the current profile. As current is the same, SEI film resistance is increasing at the same rate. However, as charging current decreases in case of an optimal scenario, the SEI film

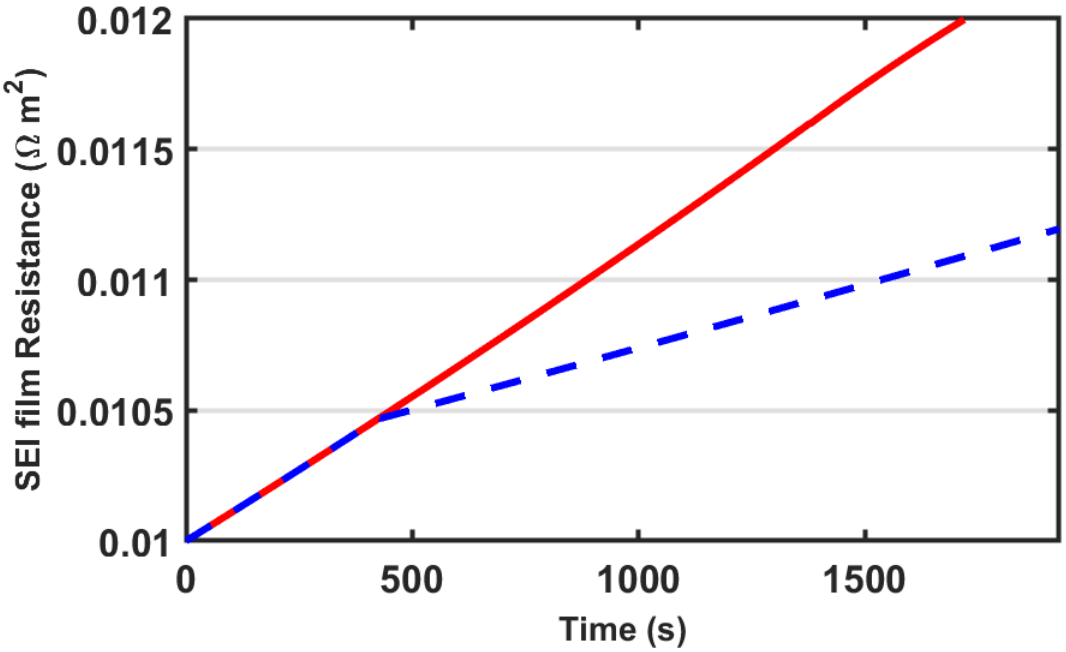

Figure 5.3: Resistance of SEI layer versus charging time: Current upper bound=2C-Temperature range 25 °C-35 °C- Optimal CCCV charging(–), Proposed SEI optimal charging(–)

resistance tends to decrease. The low current at low SOC has two advantages; (i) SEI film resistance drops significantly and (ii) temperature is in the desirable range. The temperature, however, does not high enough to drop. However, this abrupt change in optimal charging profile is useful in higher charging current rates. At higher SOC, the current is quite high and finishes at the high value. It has two advantages; higher current compensates the loss of charging time at low SOC, and it successfully reduces the SEI film resistance. The overall percentage difference of SEI film resistance in optimal and CCCV strategies is 6.9 %.

The initial temperature is 25 °C while maximum temperature limit sets to 35 °C in case of 2C current upper bound. The profiles of temperature are shown in Figure 5.4. In the optimal case, the temperature never reaches the maximum limit. However, in the case of CCCV, temperature eventually passes the maximum limit during the constant current phase. It eventually comes down to a satisfactory value because of the low current at final time. The temperature effect can be crucial for battery life and safety during continuous cycling.

The side reaction overpotential which gives qualitative information about lithium plating, must be greater than or equal to zero. It is necessary for healthy operation of

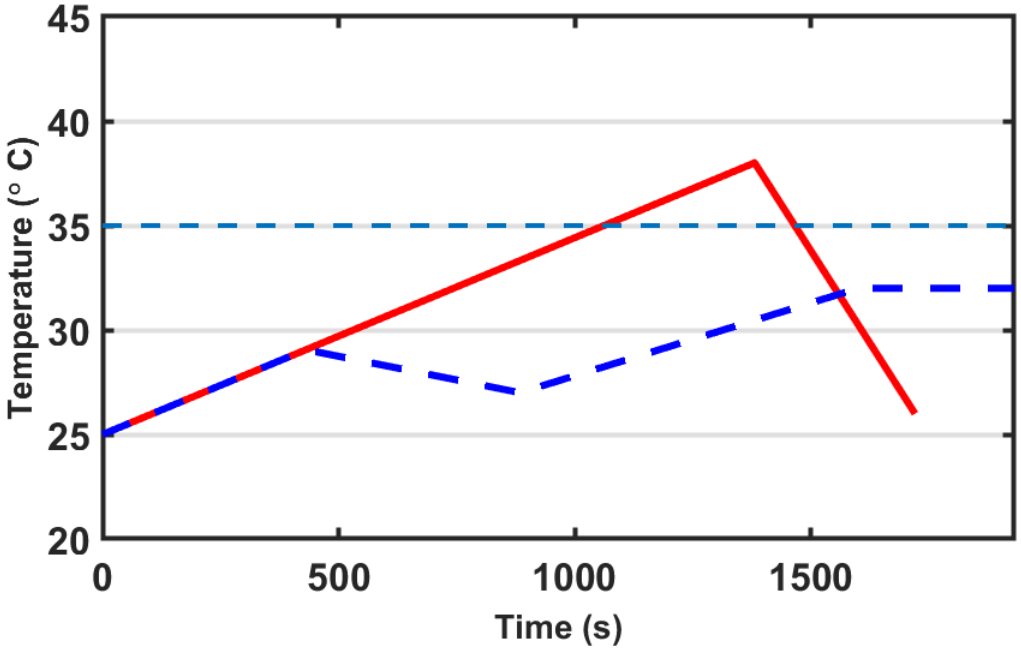

Figure 5.4: Relationship of temperature and charging time at $U_{max} = 2C$- Optimal CCCV charging(–), Proposed SEI optimal charging(–)

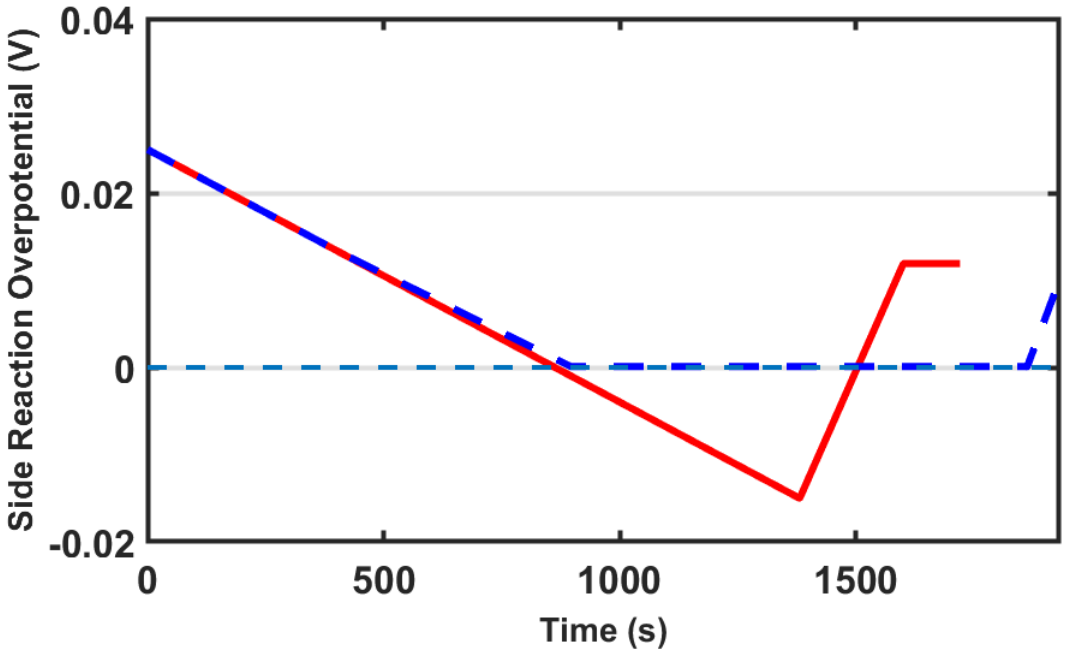

Figure 5.5: Side reaction overpotential at $U_{max} = 2C$- Optimal CCCV charging(–), Proposed SEI optimal charging(–)

battery and its longevity. The comparison of η_{sr} in optimal and CCCV cases is shown in Figure 5.5. It is positive at low SOC in CCCV case but eventually it goes down to negative range. It means at CCCV charging, it is quite a chance that lithium deposits form on the surface of the electrode. However in optimal case, side reaction constraint reaches zero and the charging current decreases to satisfy the constraint. Therefore,

optimal charging strategy successfully operates battery in a healthy regime.

The optimisation problem is repeated with the current upper bound of $U_{max} = 4C$

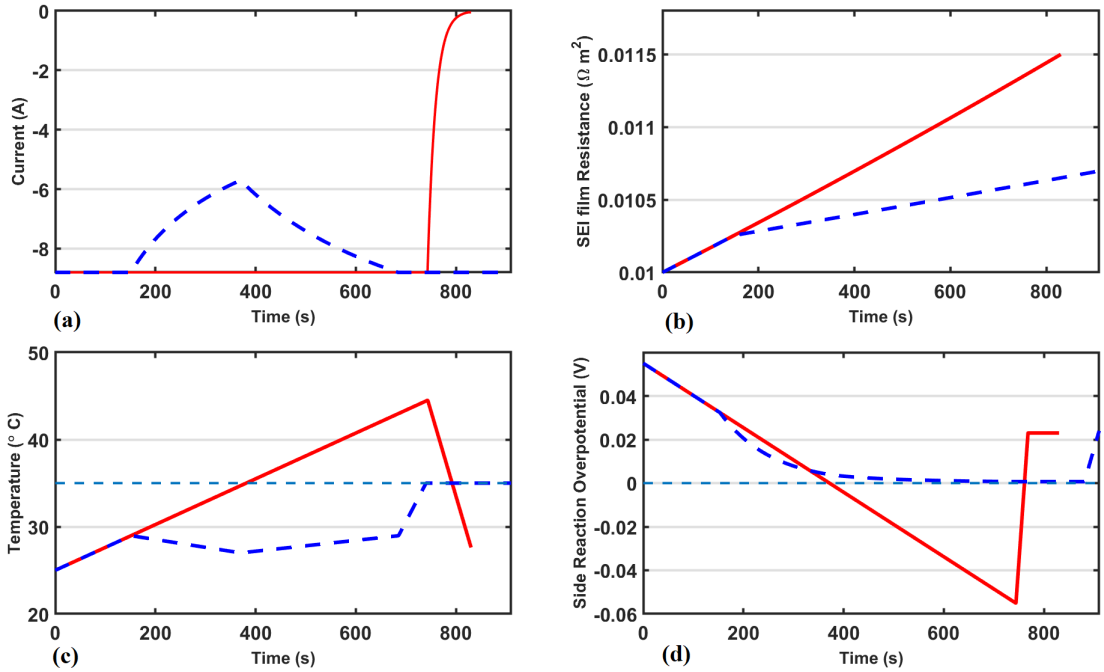

Figure 5.6: Profiles of current (a), resistance of SEI layer (b), temperature (c) and η_{sr} at $4C$- Optimal CCCV charging(–), Proposed SEI optimal charging(–)

(Figure 5.6). The current profiles are similar to Figure 5.2 qualitatively. Charging time in the optimal case is higher than CCCV. The resistance of the SEI layer significantly decreases in an optimal scenario with a percentage difference of 7.23 %. The maximum temperature sets to 35 °C. Temperature is not in the defined range in CCCV scenario, while proposed optimal strategy restrains it successfully. The side reaction overpotential goes into the negative range in CCCV as shown in Figure 5.6(d). The optimal strategy keeps it to zero to avoid lithium plating.

5.5.1 Computational efficiency

The problem (5.33) also solve using Gauss pseudo-spectral method without considering differential flatness. The aim is to compare the computational complexity of GPM with and without differential flatness. In this work, computational complexity is defined in terms of the total number of optimisation variables. The difference in computational efficiency between the two methods can be recorded with a different number of collocation points N defined in (3.1). There are two major benefits of us-

ing differential flatness in pseudo-spectral optimisation. In the case of pseudo-spectral optimisation alone, the governing battery model equations translate into inequality constraints (3.3.4). However, the differential flatness removes these constraints as state (5.19) and input (5.20) profiles are expressed in terms of the flat output (5.18). The states and input can be computed later once the optimisation complete (5.25). The second benefit of using the differential flatness approach is that it uses fewer optimisation variables. In pseudo-spectral optimisation, state x and input u produces an NLP problem with $N(n+m)$ optimisation variables, where n and m are the numbers of state and input variables. The resulting optimisation problem can be computationally expensive, especially at the high number of collocation points. However, the NLP problem has only N optimisation variables in the differential flatness approach. For example in problem (3.25), the number of optimisation variable is $4N$ in pseudo-spectral optimisation alone. However, there are three states and two outputs in the problem (5.33). It means the number of optimisation variables in pseudo-spectral optimisation alone is $7N$ compared to differential flatness which still has N optimisation variables. The states and inputs profiles are the same using both approaches, but the computational time difference is significant.

The objective of using differential flatness is to reduce the computational time, which is quite high in Gauss pseudo-spectral method. It is proved in chapter 2, that proposed strategy takes more computational time because of additional constraint. However, this difference is quite high in the case of SPM-T, because of the temperature-dependent diffusion model. Differential flatness method successfully reduces the computational time as compared to Gauss pseudo-spectral method. Figure 5.7 shows the average simulation time for a single time step at different current rates using four collocation points. Simulations prove that flatness takes less time as compared to Gauss pseudo-spectral method (GPM) at each current rate. As the current rate increases, computational time decreases in both flatness and GPM. The computational time of optimal scenario in GPM and Differential flatness method at 1C are 0.45 and 0.15 seconds, respectively. The difference is a bit low in the case of 4C, which is 0.24 and 0.03 seconds in GPM and flatness methods, respectively.

The efficiency of flatness method over GPM is also tested by using the different

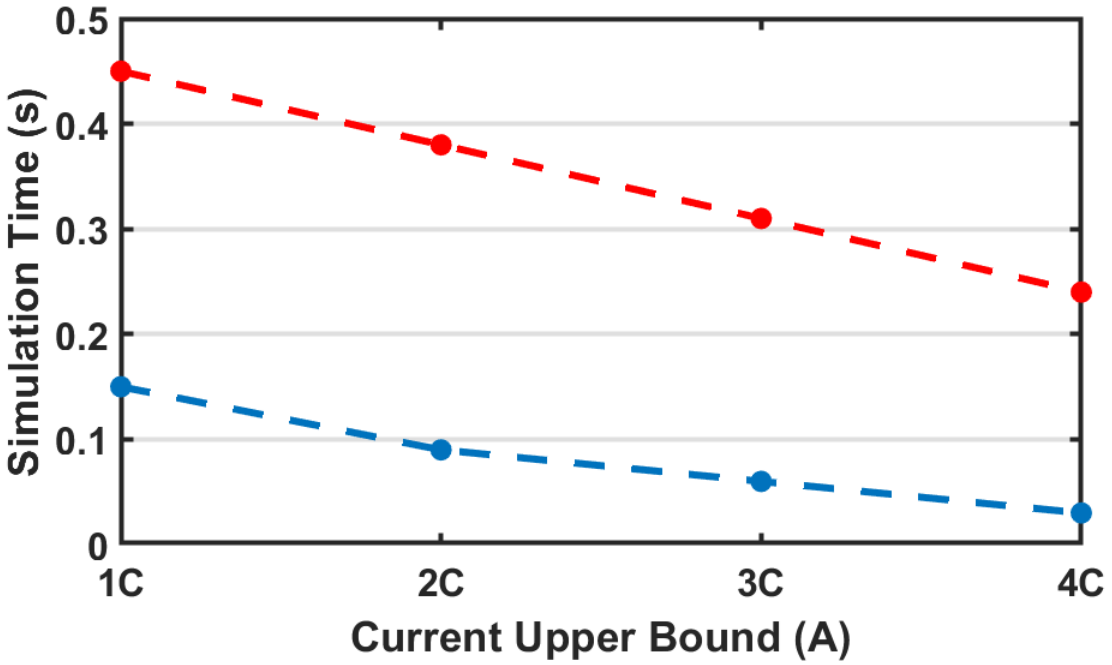

Figure 5.7: Average simulation time for one sampling interval at N=4 - GPM(–), Differential flatness(–)

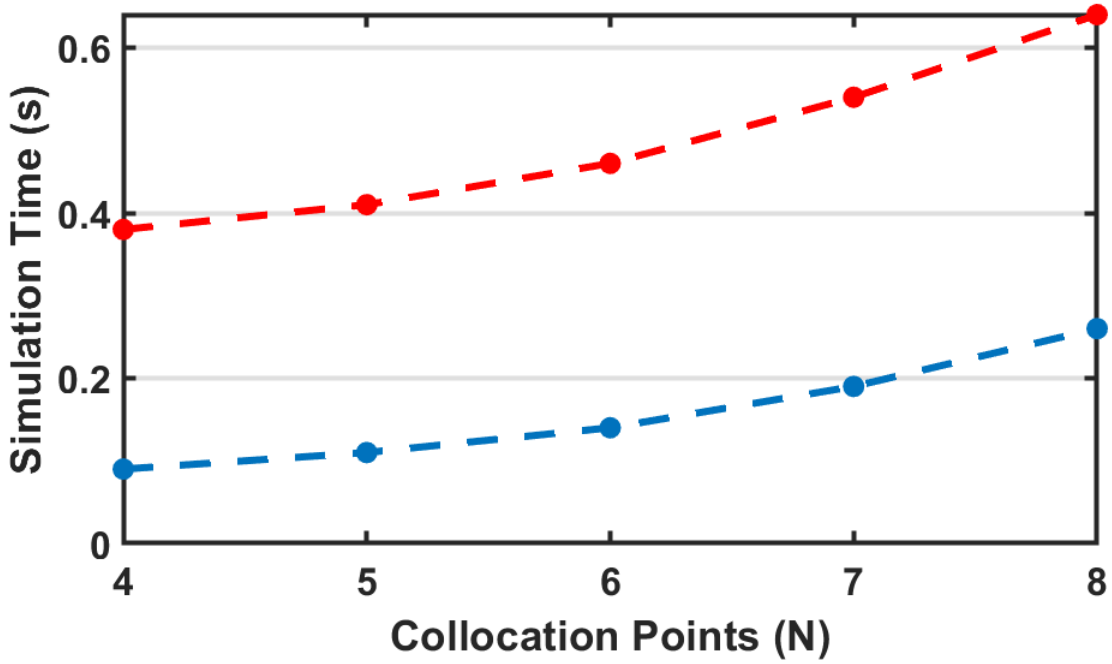

Figure 5.8: Relationship of average simulation time and collocation point (U_{max} = $2C$)- GPM(–), Differential flatness(–)

number of collocation points. Both GPM and flatness approaches produce the same charging profiles (Figure 5.8), but computational efficiency is not similar. Flatness method outperforms the GPM method at every collocation points. As the number of collocation points increases, the simulation time of both flatness and GPM increases,

keeping the current rate constant. The computational time of flatness and GPM is 0.26 and 0.64 seconds respectively at $N = 4$. Flatness method is efficient mainly for two reasons. First, the flatness method automatically satisfies the dynamic constraints. It means the NLP problem does not constitute any active dynamic constraint. Secondly, this flatness method requires a low number of optimisation variables as compared to GPM.

The summary of the comparison of proposed differential flatness (DF) method to Gauss pseudo-spectral methods is shown in Table 5.1.

Table 5.1: Comparison of the differential flatness with Gauss pseudo-spectral approaches

	GPM-I	**GPM-II**	**DF**
Battery Model	SPM	SPM	SPM
SEI Model	Yes	Yes	Yes
Temperature effects	No	Yes	Yes
Computational complexity	Medium	High	low
Collocation points	4	4	4
Prediction Horizon	Receding	Receding	Receding
states	3	4	1
inputs	1	2	2
Optimisation variables	16	24	4
Solver	fmincon	fmincon	fmincon
Time Consumption	high	high	low
Average simulation time (N=4, $I_{max} = 1C$)	0.37	0.45	0.15

Chapter 6

Conclusions and Future Work

6.1 Conclusions

The dissertation proposes an online NMPC framework that minimises SEI layer growth during charging considering chemical or mechanical degradation. The work builds on the literature that highlights the challenges of the computational efficiency of model-based control in an online optimisation problem and quantifies the state of health in terms of SEI layer growth. The differential flatness method is also compared with the pseudo-spectral method to test the computational efficiency using the proposed algorithm approach.

The proposed algorithm uses the integral Gauss pseudo-spectral approach to optimise battery charging trajectory. In chemical degradation, apart from the SEI layer minimisation, the algorithm deals with another side reaction, i.e. lithium plating. The algorithm guarantees that the battery works in a healthy regime, i.e. positive during charging. It is evident from the results that SEI film resistance decreases significantly in proposed SEI optimal charging as compared to optimal CCCV charging. There is up to 24% difference in SEI layer growth, recorded in the proposed SEI optimal methodology. SEI layer resistance is higher in the optimal CCCV charging than the proposed algorithm, considering the same charging time.

The proposed NMPC strategy is also used to optimise charging trajectory by explicitly incorporated mechanical degradation effects. Diffusion induced stresses are believed to cause the growth of the SEI layer. The main aim is to find any similarities in charg-

ing pattern by incorporating chemical or mechanical degradation concepts separately. The proposed methodology is based on the assumption that the electrode's active material is not the weakest material (elastic range) but the SEI layer, which breaks and repairs during charging. It is proved that although CCCV is the most popular method to charge the battery, it increases the amplitude stresses as compared to the proposed methodology. An optimal charging profile is always preferable to CCCV over the range of DOD levels. The proposed NMPC framework is also compared with already published experimental ageing data. Results confirmed that the proposed strategy outperforms experimental data almost at every level. There is not much difference recorded at low DOD levels, but the performance of the proposed strategy is substantial at 50% and 100% depth of discharge levels.

The differential flatness method is also used to compare the computational efficiency with the Gauss pseudo-spectral method. SPM-T is used to analyse the thermal dynamic in lithium-ion batteries instead of SPM. Moreover, optimisation runs in the predefined temperature range. NMPC framework takes care of two side reactions; SEI layer growth and lithium plating. The differential flatness method outperforms the GPM either in terms of collocation points or maximum current upper bounds.

The main improvements compared to existing literature are as follows:

- The SEI layer growth has been quantified considering chemical degradations (Figures 4.2, 4.5, 4.7 and 4.9).
- The proposed optimal strategy reduces the SEI layer growth compared to optimal CCCV charging considering chemical degradation (Figures 4.2, 4.5, 4.7 and 4.9).
- The proposed optimal framework ensures that battery operates in a healthy regime, i.e. side reaction overpotential is positive considering chemical degradation along with minimising SEI film resistance (Figures 4.3, 5.5 and 5.6).
- The results shows that charging should not be terminated at low current irrespective of degradation concept (Figures 4.2 and 4.11).
- The computational efficiency of proposed charging algorithm is significantly

improved using differential flatness (Table 4.2, Figures 5.7 and 5.8).

6.2 Future work

The proposed SEI optimal methodology is the best candidate to charge the battery. This work can be further used to compute cyclic capacity fade, thus estimating the life of batteries. Model-based control is difficult to implement online but useful as it computes the internal variables of the batteries. The battery model is an essential part of online optimisation and should be computationally inexpensive. A homogenised model of lithium-ion batteries can be used to predict SOC and SOH. In battery packs, a set of connected models (ECMs and EMs) can estimate various variables in the batteries. The effective control of BMS is the future direction of control engineers.

The testing of the proposed optimal charging profiles is the future step. In the proposed strategies, it is recommended that charging should start at a low current and ends at a higher current value. It decreases the degradation rate in lithium-ion batteries. Moreover, implementing the proposed NMPC strategy (chemical or mechanical degradation mechanisms) in BMS is another future research direction. Past data of batteries is critical for two reasons: empirical modelling and charging trajectory can be optimised for whole battery life.

A single battery cell's optimised battery charging profile can be extended to a battery pack by achieving cell equalisation. The resultant charging strategy is more intelligent and runs according to user demand. The online optimisation scheme runs for only one optimal charging trajectory, and the remaining cells should follow this designed cell, which can initially reduce the computational time. The violation of constraints (e.g. overcharging) is effectively minimised due to the online management system using well-defined cell balancing approach. Although this closed optimal scheme slightly takes more time than an open loop, it over-performs later because of robustness and real-time errors of the system. Also, it can successfully reduce the degradation effects on the battery.

The work can be extended to optimise the charging scenario in electric vehicles. A few areas for further research, specifically for control engineers, include:

- The proposed algorithm can be implemented using DFN or P2D battery models to increase the accuracy of estimating the states of charge and health of lithium-ion batteries.
- The proposed algorithm can be extended to the entire battery pack to estimate the ageing of batteries.
- An intelligent battery management system using the proposed battery charging approach can be formulated to quantify the ageing effects of lithium-ion batteries while cycling.

Bibliography

[1] Jie Li, K Adewuyi, Nima Lotfi, Robert G Landers, and Jonghyun Park. A single particle model with chemical/mechanical degradation physics for lithium ion battery state of health (soh) estimation. *Applied energy*, 212:1178–1190, 2018.

[2] Scott J Moura, Nalin A Chaturvedi, and M Krstić. Constraint management in li-ion batteries: A modified reference governor approach. In *2013 American Control Conference*, pages 5332–5337. IEEE, 2013.

[3] Christopher D Rahn and Chao-Yang Wang. *Battery systems engineering*. John Wiley & Sons, 2013.

[4] Reinhardt Klein, Nalin A Chaturvedi, Jake Christensen, Jasim Ahmed, Rolf Findeisen, and Aleksandar Kojic. Electrochemical model based observer design for a lithium-ion battery. *IEEE Transactions on Control Systems Technology*, 21(2):289–301, 2012.

[5] Eduardo Redondo-Iglesias, Pascal Venet, and Serge Pelissier. Calendar and cycling ageing combination of batteries in electric vehicles. *Microelectronics Reliability*, 88:1212–1215, 2018.

[6] Ramadass, PHBWRPB and Haran, Bala and White, Ralph and Popov, Branko N. Capacity fade of Sony 18650 cells cycled at elevated temperatures: Part I. Cycling performance. *Journal of power sources*, 112(2):606–613, 2002.

[7] M Safari, M Morcrette, A Teyssot, and C Delacourt. Multimodal physics-based aging model for life prediction of li-ion batteries. *Journal of The Electrochemical Society*, 156(3):A145, 2008.

[8] P Gyan, P Aubret, J Hafsaoui, F Sellier, S Bourlot, Stéphane Zinola, and François Badin. Experimental assessment of battery cycle life within the simstock research program. *Oil & Gas Science and Technology–Revue d'IFP Energies nouvelles*, 68(1):137–147, 2013.

[9] Zhe Li, Languang Lu, Minggao Ouyang, and Yuankun Xiao. Modeling the capacity degradation of lifepo4/graphite batteries based on stress coupling analysis. *Journal of Power Sources*, 196(22):9757–9766, 2011.

[10] John Wang, Ping Liu, Jocelyn Hicks-Garner, Elena Sherman, Souren Soukiazian, Mark Verbrugge, Harshad Tataria, James Musser, and Peter Finamore. Cycle-life model for graphite-lifepo4 cells. *Journal of power sources*, 196(8):3942–3948, 2011.

[11] Noshin Omar, Mohamed Abdel Monem, Yousef Firouz, Justin Salminen, Jelle Smekens, Omar Hegazy, Hamid Gaulous, Grietus Mulder, Peter Van den Bossche, Thierry Coosemans, et al. Lithium iron phosphate based battery–assessment of the aging parameters and development of cycle life model. *Applied Energy*, 113:1575–1585, 2014.

[12] Eduardo Redondo-Iglesias, Pascal Venet, and Serge Pelissier. Global model for self-discharge and capacity fade in lithium-ion batteries based on the generalized eyring relationship. *IEEE Transactions on Vehicular Technology*, 67(1):104–113, 2017.

[13] M Safari, M Morcrette, A Teyssot, and C Delacourt. Life prediction methods for lithium-ion batteries derived from a fatigue approach ii. capacity-loss prediction of batteries subjected to complex current profiles. *Journal of The Electrochemical Society*, 157(7):A892–A898, 2010.

[14] Christoph R Birkl, Matthew R Roberts, Euan McTurk, Peter G Bruce, and David A Howey. Degradation diagnostics for lithium ion cells. *Journal of Power Sources*, 341:373–386, 2017.

[15] J Henry. Chevy volt battery fires threaten all electric vehicle makers, not just gm, 2011.

[16] Michael J Rothenberger. Optimal input shaping for fisher identifiability of control-oriented lithium-ion battery models. 2016.

[17] Andrey W Golubkov, René Planteu, Philipp Krohn, Bernhard Rasch, Bernhard Brunnsteiner, Alexander Thaler, and Viktor Hacker. Thermal runaway of large automotive li-ion batteries. *Rsc Advances*, 8(70):40172–40186, 2018.

[18] Fredrik Larsson, Simon Bertilsson, Maurizio Furlani, Ingvar Albinsson, and Bengt-Erik Mellander. Gas explosions and thermal runaways during external heating abuse of commercial lithium-ion graphite-licoo2 cells at different levels of ageing. *Journal of power sources*, 373:220–231, 2018.

[19] Donal P Finegan, Eric Darcy, Matthew Keyser, Bernhard Tjaden, Thomas MM Heenan, Rhodri Jervis, Josh J Bailey, Romeo Malik, Nghia T Vo, Oxana V Magdysyuk, et al. Characterising thermal runaway within lithium-ion cells by inducing and monitoring internal short circuits. *Energy & Environmental Science*, 10(6):1377–1388, 2017.

[20] Stefan Adams. Ultrafast lithium migration in surface modified lifepo4 by heterogeneous doping. *Applied energy*, 90(1):323–328, 2012.

[21] M Ottaway. Lithium batteries, highly energetic materials: The varied use of adiabatic calorimetry to aid safety and battery development. In *37th North American thermal Analysis Society (NATAS) annual conference, USA*, 2009.

[22] C Julien. Design considerations for lithium batteries. In *Materials for lithium-ion batteries*, pages 1–20. Springer, 2000.

[23] Isidor Buchmann. Batteries in a portable world: a handbook on rechargeable batteries for non-engineers. 2001.

[24] Qian Lin, Jun Wang, Rui Xiong, Weixiang Shen, and Hongwen He. Towards a smarter battery management system: A critical review on optimal charging methods of lithium ion batteries. *Energy*, 183:220–234, 2019.

[25] B Gundogdu, DT Gladwin, MP Foster, and DA Stone. A forecasting battery state of charge management strategy for frequency response in the uk system. In *2018 IEEE International Conference on Industrial Technology (ICIT)*, pages 1726–1731. IEEE, 2018.

[26] M Brandl, H Gall, M Wenger, V Lorentz, M Giegerich, Federico Baronti, Gabriele Fantechi, Luca Fanucci, Roberto Roncella, Roberto Saletti, et al. Batteries and battery management systems for electric vehicles. In *2012 Design, Automation & Test in Europe Conference & Exhibition (DATE)*, pages 971–976. IEEE, 2012.

[27] Yinjiao Xing, Eden WM Ma, Kwok L Tsui, and Michael Pecht. Battery management systems in electric and hybrid vehicles. *Energies*, 4(11):1840–1857, 2011.

[28] Reinhardt Klein, Nalin A Chaturvedi, Jake Christensen, Jasim Ahmed, Rolf Findeisen, and Aleksandar Kojic. Optimal charging strategies in lithium-ion battery. In *Proceedings of the 2011 american Control Conference*, pages 382–387. IEEE, 2011.

[29] Philipp Fortenbacher, Johanna L Mathieu, and Göran Andersson. Modeling, identification, and optimal control of batteries for power system applications. In *2014 Power Systems Computation Conference*, pages 1–7. IEEE, 2014.

[30] Ming Shen and Qing Gao. A review on battery management system from the modeling efforts to its multiapplication and integration. *International Journal of Energy Research*, 43(10):5042–5075, 2019.

[31] Jinhao Meng, Mattia Ricco, Guangzhao Luo, Maciej Swierczynski, Daniel-Ioan Stroe, Ana-Irina Stroe, and Remus Teodorescu. An overview and comparison of online implementable soc estimation methods for lithium-ion battery. *IEEE Transactions on Industry Applications*, 54(2):1583–1591, 2017.

[32] Juan Pablo Rivera-Barrera, Nicolás Muñoz-Galeano, and Henry Omar Sarmiento-Maldonado. Soc estimation for lithium-ion batteries: Review and future challenges. *Electronics*, 6(4):102, 2017.

[33] Qian Wang, Bin Jiang, Bo Li, and Yuying Yan. A critical review of thermal management models and solutions of lithium-ion batteries for the development of pure electric vehicles. *Renewable and Sustainable Energy Reviews*, 64:106–128, 2016.

[34] Joris Jaguemont and Joeri Van Mierlo. A comprehensive review of future thermal management systems for battery-electrified vehicles. *Journal of Energy Storage*, 31:101551, 2020.

[35] Naixing Yang, Xiongwen Zhang, Guojun Li, and Dong Hua. Assessment of the forced air-cooling performance for cylindrical lithium-ion battery packs: A comparative analysis between aligned and staggered cell arrangements. *Applied thermal engineering*, 80:55–65, 2015.

[36] Lip Huat Saw, Yonghuang Ye, Andrew AO Tay, Wen Tong Chong, Seng How Kuan, and Ming Chian Yew. Computational fluid dynamic and thermal analysis of lithium-ion battery pack with air cooling. *Applied energy*, 177:783–792, 2016.

[37] Taeyoung Han, Bahram Khalighi, Erik C Yen, and Shailendra Kaushik. Li-ion battery pack thermal management: liquid versus air cooling. *Journal of Thermal Science and Engineering Applications*, 11(2), 2019.

[38] Cong Wang, Guoqing Zhang, Xinxi Li, Jin Huang, Ziyuan Wang, Youfu Lv, Like Meng, Wenfu Situ, and Mumin Rao. Experimental examination of large capacity lifepo4 battery pack at high temperature and rapid discharge using novel liquid cooling strategy. *International Journal of Energy Research*, 42(3):1172–1182, 2018.

[39] Xiongwen Zhang, Xin Kong, Guojun Li, and Jun Li. Thermodynamic assessment of active cooling/heating methods for lithium-ion batteries of electric vehicles in extreme conditions. *Energy*, 64:1092–1101, 2014.

[40] Seonggi Park, Dong Soo Jang, DongChan Lee, Seong Ho Hong, and Yongchan Kim. Simulation on cooling performance characteristics of a refrigerant-cooled

active thermal management system for lithium ion batteries. *International journal of heat and mass transfer*, 135:131–141, 2019.

[41] Abu Raihan Mohammad Siddique, Shohel Mahmud, and Bill Van Heyst. A comprehensive review on a passive (phase change materials) and an active (thermoelectric cooler) battery thermal management system and their limitations. *Journal of Power Sources*, 401:224–237, 2018.

[42] Farah Souayfane, Farouk Fardoun, and Pascal-Henry Biwole. Phase change materials (pcm) for cooling applications in buildings: A review. *Energy and buildings*, 129:396–431, 2016.

[43] Huiming Zou, Wei Wang, Guiying Zhang, Fei Qin, Changqing Tian, and Yuying Yan. Experimental investigation on an integrated thermal management system with heat pipe heat exchanger for electric vehicle. *Energy Conversion and Management*, 118:88–95, 2016.

[44] Qian Wang, Bin Jiang, QF Xue, HL Sun, Bo Li, HM Zou, and YY Yan. Experimental investigation on ev battery cooling and heating by heat pipes. *Applied Thermal Engineering*, 88:54–60, 2015.

[45] Xinxi Li, Zhaoda Zhong, Jinghai Luo, Ziyuan Wang, Weizhong Yuan, Guoqing Zhang, Chengzhao Yang, and Chuxiong Yang. Experimental investigation on a thermoelectric cooler for thermal management of a lithium-ion battery module. *International Journal of Photoenergy*, 2019, 2019.

[46] Annika Hacker, Ravi Gorthala, and Maria-Isabel Carnasciali. Thermoelectric heating and cooling system with integrated thermal energy storage (thermal battery) for electric vehicles. In *ASME 2018 12th International Conference on Energy Sustainability collocated with the ASME 2018 Power Conference and the ASME 2018 Nuclear Forum*. American Society of Mechanical Engineers Digital Collection, 2018.

[47] Peng Qin, Mengran Liao, Danfeng Zhang, Yujun Liu, Jinhua Sun, and Qingsong Wang. Experimental and numerical study on a novel hybrid battery thermal

management system integrated forced-air convection and phase change material. *Energy Conversion and Management*, 195:1371–1381, 2019.

[48] Hassan Fathabadi. High thermal performance lithium-ion battery pack including hybrid active–passive thermal management system for using in hybrid/electric vehicles. *Energy*, 70:529–538, 2014.

[49] Lip Huat Saw, Hiew Mun Poon, Hui San Thiam, Zuansi Cai, Wen Tong Chong, Nugroho Agung Pambudi, and Yeong Jin King. Novel thermal management system using mist cooling for lithium-ion battery packs. *Applied energy*, 223:146–158, 2018.

[50] Qing Gao, Yubin Liu, Guohua Wang, Fan Deng, and Jichen Zhu. An experimental investigation of refrigerant emergency spray on cooling and oxygen suppression for overheating power battery. *Journal of Power Sources*, 415:33–43, 2019.

[51] Bittagopal Mondal, Carlos F Lopez, and Partha P Mukherjee. Exploring the efficacy of nanofluids for lithium-ion battery thermal management. *International Journal of Heat and Mass Transfer*, 112:779–794, 2017.

[52] Yutao Huo and Zhonghao Rao. The numerical investigation of nanofluid based cylinder battery thermal management using lattice boltzmann method. *International Journal of Heat and Mass Transfer*, 91:374–384, 2015.

[53] Saeed Khaleghi Rahimian, Sean Rayman, and Ralph E White. Optimal charge rates for a lithium ion cell. *Journal of Power Sources*, 196(23):10297–10304, 2011.

[54] Kandler A Smith, Christopher D Rahn, and Chao-Yang Wang. Model-based electrochemical estimation and constraint management for pulse operation of lithium ion batteries. *IEEE Transactions on Control Systems Technology*, 18(3):654–663, 2009.

[55] Bharatkumar Suthar, Paul WC Northrop, Richard D Braatz, and Venkat R Subramanian. Optimal charging profiles with minimal intercalation-induced stresses

for lithium-ion batteries using reformulated pseudo 2-dimensional models. *Journal of The Electrochemical Society*, 161(11):F3144, 2014.

[56] Yinjiao Xing, Eden WM Ma, Kwok L Tsui, and Michael Pecht. Battery management systems in electric and hybrid vehicles. *Energies*, 4(11):1840–1857, 2011.

[57] James M Green, Brent Hartman, and Peter F Glowacki. A system-based view of the standards and certification landscape for electric vehicles. *World Electric Vehicle Journal*, 8(2):564–575, 2016.

[58] Jiuchun Jiang and Caiping Zhang. *Fundamentals and applications of lithium-ion batteries in electric drive vehicles*. John Wiley & Sons, 2015.

[59] Valer Pop, Henk Jan Bergveld, Dmitry Danilov, Paul PL Regtien, and Peter HL Notten. *Battery management systems: Accurate state-of-charge indication for battery-powered applications*, volume 9. Springer Science & Business Media, 2008.

[60] Woosuk Sung and Chee Burm Shin. Electrochemical model of a lithium-ion battery implemented into an automotive battery management system. *Computers & Chemical Engineering*, 76:87–97, 2015.

[61] Markus Lelie, Thomas Braun, Marcus Knips, Hannes Nordmann, Florian Ringbeck, Hendrik Zappen, and Dirk Uwe Sauer. Battery management system hardware concepts: an overview. *Applied Sciences*, 8(4):534, 2018.

[62] Orazio Aiello. Electromagnetic susceptibility of battery management systems' ics for electric vehicles: Experimental study. *Electronics*, 9(3):510, 2020.

[63] Thomas Bruen, James Michael Hooper, James Marco, Miguel Gama, and Gael Henri Chouchelamane. Analysis of a battery management system (bms) control strategy for vibration aged nickel manganese cobalt oxide (nmc) lithium-ion 18650 battery cells. *Energies*, 9(4):255, 2016.

[64] Kailong Liu, Kang Li, Qiao Peng, and Cheng Zhang. A brief review on key technologies in the battery management system of electric vehicles. *Frontiers of mechanical engineering*, 14(1):47–64, 2019.

[65] Rui Xiong, Suxiao Ma, Hailong Li, Fengchun Sun, and Ju Li. Toward a safer battery management system: A critical review on diagnosis and prognosis of battery short circuit. *Iscience*, 23(4):101010, 2020.

[66] Languang Lu, Xuebing Han, Jianqiu Li, Jianfeng Hua, and Minggao Ouyang. A review on the key issues for lithium-ion battery management in electric vehicles. *Journal of power sources*, 226:272–288, 2013.

[67] Hossam A Gabbar, Ahmed M Othman, and Muhammad R Abdussami. Review of battery management systems (bms) development and industrial standards. *Technologies*, 9(2):28, 2021.

[68] Ali Davari and Abozar Ahmadi. New implementation of legendre polynomials for solving partial differential equations. *Applied Mathematics*, 4(12):1647, 2013.

[69] Michelle A Kehs, Michael D Beeney, and Hosam K Fathy. Computational efficiency of solving the dfn battery model using descriptor form with legendre polynomials and galerkin projections. In *2014 American Control Conference*, pages 260–267. IEEE, 2014.

[70] Daniel Ronald Herber. Basic implementation of multiple-interval pseudospectral methods to solve optimal control problems. Technical report, 2015.

[71] Liang Yang, Hao Zhou, and Wanchun Chen. Application of linear gauss pseudospectral method in model predictive control. *Acta Astronautica*, 96:175–187, 2014.

[72] Anil V Rao, David A Benson, Christopher Darby, Michael A Patterson, Camila Francolin, Ilyssa Sanders, and Geoffrey T Huntington. Algorithm 902: Gpops, a matlab software for solving multiple-phase optimal control problems using the gauss pseudospectral method. *ACM Transactions on Mathematical Software (TOMS)*, 37(2):1–39, 2010.

[73] Qi Gong, Wei Kang, Nazareth S Bedrossian, Fariba Fahroo, Pooya Sekhavat, and Kevin Bollino. Pseudospectral optimal control for military and industrial

applications. In *2007 46th IEEE Conference on Decision and Control*, pages 4128–4142. IEEE, 2007.

[74] David Benson. *A Gauss pseudospectral transcription for optimal control*. PhD thesis, Massachusetts Institute of Technology, 2005.

[75] Rutooj Deshpande, Mark Verbrugge, Yang-Tse Cheng, John Wang, and Ping Liu. Battery cycle life prediction with coupled chemical degradation and fatigue mechanics. *Journal of the Electrochemical Society*, 159(10):A1730–A1738, 2012.

[76] Sébastien Grolleau, Arnaud Delaille, Hamid Gualous, Philippe Gyan, Renaud Revel, Julien Bernard, Eduardo Redondo-Iglesias, Jérémy Peter, and SIMCAL Network. Calendar aging of commercial graphite/lifepo4 cell–predicting capacity fade under time dependent storage conditions. *Journal of Power Sources*, 255:450–458, 2014.

[77] Jiagang Xu, Rutooj D Deshpande, Jie Pan, Yang-Tse Cheng, and Vincent S Battaglia. Electrode side reactions, capacity loss and mechanical degradation in lithium-ion batteries. *Journal of The Electrochemical Society*, 162(10):A2026–A2035, 2015.

[78] Izaro Laresgoiti, Stefan Käbitz, Madeleine Ecker, and Dirk Uwe Sauer. Modeling mechanical degradation in lithium ion batteries during cycling: Solid electrolyte interphase fracture. *Journal of Power Sources*, 300:112–122, 2015.

[79] Ecker, Madeleine and Nieto, Nerea and Käbitz, Stefan and Schmalstieg, Johannes and Blanke, Holger and Warnecke, Alexander and Sauer, Dirk Uwe. Calendar and cycle life study of Li (NiMnCo) O2-based 18650 lithium-ion batteries. *Journal of Power Sources*, 248:839–851, 2014.

[80] Ji Liu, Guang Li, and Hosam K Fathy. A computationally efficient approach for optimizing lithium-ion battery charging. *Journal of Dynamic Systems, Measurement, and Control*, 138(2), 2016.

[81] JC Burns, DA Stevens, and JR Dahn. In-situ detection of lithium plating using high precision coulometry. *Journal of the Electrochemical Society*, 162(6):A959, 2015.

[82] Nan Li, Feng Gao, Tianqu Hao, Zhan Ma, and Chenghui Zhang. Soh balancing control method for the mmc battery energy storage system. *IEEE Transactions on Industrial Electronics*, 65(8):6581–6591, 2017.

[83] Kaiyuan Li, Feng Wei, King Jet Tseng, and Boon-Hee Soong. A practical lithium-ion battery model for state of energy and voltage responses prediction incorporating temperature and ageing effects. *IEEE Transactions on Industrial Electronics*, 65(8):6696–6708, 2017.

[84] Chin Pei Tang, Patrick T Miller, Venkat N Krovi, Ji-Chul Ryu, and Sunil K Agrawal. Differential-flatness-based planning and control of a wheeled mobile manipulator—theory and experiment. *IEEE/ASME Transactions on Mechatronics*, 16(4):768–773, 2010.

[85] Béatrice Laroche, Philippe Martin, and Pierre Rouchon. Motion planning for the heat equation. *International Journal of Robust and Nonlinear Control: IFAC-Affiliated Journal*, 10(8):629–643, 2000.

[86] Ji Liu, Guang Li, and Hosam K Fathy. An extended differential flatness approach for the health-conscious nonlinear model predictive control of lithium-ion batteries. *IEEE Transactions on Control Systems Technology*, 25(5):1882–1889, 2016.

[87] David Q Mayne. Model predictive control: Recent developments and future promise. *Automatica*, 50(12):2967–2986, 2014.

[88] Jingyu Yan, Guoqing Xu, Huihuan Qian, Yangsheng Xu, and Zhibin Song. Model predictive control-based fast charging for vehicular batteries. *Energies*, 4(8):1178–1196, 2011.

[89] Marcello Torchio, Nicolas A Wolff, Davide M Raimondo, Lalo Magni, Ulrike Krewer, R Bushan Gopaluni, Joel A Paulson, and Richard D Braatz. Real-time

model predictive control for the optimal charging of a lithium-ion battery. In *2015 American Control Conference (ACC)*, pages 4536–4541. IEEE, 2015.

[90] Kailong Liu, Kang Li, and Cheng Zhang. Constrained generalized predictive control of battery charging process based on a coupled thermoelectric model. *Journal of Power Sources*, 347:145–158, 2017.

[91] Marcelo A Xavier and M Scott Trimboli. Lithium-ion battery cell-level control using constrained model predictive control and equivalent circuit models. *Journal of Power Sources*, 285:374–384, 2015.

[92] Quan Ouyang, Jian Chen, Jian Zheng, and Huazhen Fang. Optimal multiobjective charging for lithium-ion battery packs: A hierarchical control approach. *IEEE Transactions on Industrial Informatics*, 14(9):4243–4253, 2018.

[93] Ning Tian, Huazhen Fang, and Yebin Wang. Real-time optimal lithium-ion battery charging based on explicit model predictive control. *IEEE Transactions on Industrial Informatics*, 17(2):1318–1330, 2020.

[94] Manan Pathak, Dayaram Sonawane, Shriram Santhanagopalan, Richard D Braatz, and Venkat R Subramanian. Analyzing and minimizing capacity fade through optimal model-based control-theory and experimental validation. *ECS transactions*, 75(23):51, 2017.

[95] Sai Varun Aduru, Manan Pathak, Suryanarayana Kolluri, Richard D Braatz, and Venkat R Subramanian. Nonlinear model predictive control strategies for optimal charging of a lithium-ion battery. In *ECS Meeting Abstracts*, number 1, page 106. IOP Publishing, 2019.

[96] Marcello Torchio, L Magni, Richard D Braatz, and DM Raimondo. Design of piecewise affine and linear time-varying model predictive control strategies for advanced battery management systems. *Journal of The Electrochemical Society*, 164(4):A949, 2017.

[97] M Torchio, L Magni, RD Braatz, and DM Raimondo. Optimal health-aware charging protocol for lithium-ion batteries: A fast model predictive control approach. *IFAC-PapersOnLine*, 49(7):827–832, 2016.

[98] Ahsen Ulutas, Ismail Hakki Altas, Ahmet Onen, and Taha Selim Ustun. Neuro-fuzzy-based model predictive energy management for grid connected microgrids. *Electronics*, 9(6):900, 2020.

[99] ASHUTOSH A PATWARDHAN, JAMES B RAWLINGS, and THOMAS F EDGAR. Nonlinear model predictive control. *Chemical Engineering Communications*, 87(1):123–141, 1990.

[100] Bharatkumar Suthar. Optimal battery operations and design considering capacity fade mechanisms. 2015.

[101] Suryanarayana Kolluri, Sai Varun Aduru, Manan Pathak, Richard D Braatz, and Venkat R Subramanian. Real-time nonlinear model predictive control (nmpc) strategies using physics-based models for advanced lithium-ion battery management system (bms). *Journal of The Electrochemical Society*, 167(6):063505, 2020.

[102] Changfu Zou, Chris Manzie, and Dragan Nešić. Model predictive control for lithium-ion battery optimal charging. *IEEE/ASME Transactions on Mechatronics*, 23(2):947–957, 2018.

[103] Jianhua Guo, Wei Zhang, Cui Liu, and Liang Chu. Adaptive model predictive control strategy of hybrid electric bus based on soc programming. In *2016 IEEE Information Technology, Networking, Electronic and Automation Control Conference*, pages 796–799. IEEE, 2016.

[104] David Q Mayne, James B Rawlings, Christopher V Rao, and Pierre OM Scokaert. Constrained model predictive control: Stability and optimality. *Automatica*, 36(6):789–814, 2000.

[105] Jamie Gomez, Ruben Nelson, Egwu E Kalu, Mark H Weatherspoon, and Jim P Zheng. Equivalent circuit model parameters of a high-power li-ion battery: Ther-

mal and state of charge effects. *Journal of Power Sources*, 196(10):4826–4831, 2011.

[106] Saehong Park, Dylan Kato, Zach Gima, Reinhardt Klein, and Scott Moura. Optimal experimental design for parameterization of an electrochemical lithium-ion battery model. *Journal of The Electrochemical Society*, 165(7):A1309, 2018.

[107] Tanvir R Tanim, Christopher D Rahn, and Chao-Yang Wang. A temperature dependent, single particle, lithium ion cell model including electrolyte diffusion. *Journal of Dynamic Systems, Measurement, and Control*, 137(1), 2015.

[108] TR Ashwin, Yongmann M Chung, and Jihong Wang. Capacity fade modelling of lithium-ion battery under cyclic loading conditions. *Journal of Power Sources*, 328:586–598, 2016.

[109] Xiaosong Hu, Shengbo Li, Huei Peng, and Fengchun Sun. Charging time and loss optimization for linmc and lifepo4 batteries based on equivalent circuit models. *Journal of Power Sources*, 239:449–457, 2013.

[110] R Painter, B Berryhill, L Sharpe, and S Keith Hargrove. A single particle thermal model for lithium ion batteries. In *Proceedings COMSOL Conference*, 2014.

[111] Tanvir R Tanim, Christopher D Rahn, and Chao-Yang Wang. State of charge estimation of a lithium ion cell based on a temperature dependent and electrolyte enhanced single particle model. *Energy*, 80:731–739, 2015.

[112] Shu-Xia Tang, Leobardo Camacho-Solorio, Yebin Wang, and Miroslav Krstic. State-of-charge estimation from a thermal–electrochemical model of lithium-ion batteries. *Automatica*, 83:206–219, 2017.

[113] Zhihao Yu, Ruituo Huai, and Linjing Xiao. State-of-charge estimation for lithium-ion batteries using a kalman filter based on local linearization. *Energies*, 8(8):7854–7873, 2015.

[114] Kandler A Smith, Christopher D Rahn, and Chao-Yang Wang. Model order reduction of 1d diffusion systems via residue grouping. *Journal of Dynamic Systems, Measurement, and Control*, 130(1), 2008.

[115] Venkat R Subramanian, Vinten D Diwakar, and Deepak Tapriyal. Efficient macro-micro scale coupled modeling of batteries. *Journal of The Electrochemical Society*, 152(10):A2002, 2005.

[116] Long Cai and Ralph E White. Lithium ion cell modeling using orthogonal collocation on finite elements. *Journal of Power Sources*, 217:248–255, 2012.

[117] Christopher Mayhew, Wei He, Christoph Kroener, Reinhardt Klein, Nalin Chaturvedi, and Aleksandar Kojić. Investigation of projection-based model-reduction techniques for solid-phase diffusion in li-ion batteries. In *2014 American Control Conference*, pages 123–128. IEEE, 2014.

[118] I Michael Ross and Fariba Fahroo. Issues in the real-time computation of optimal control. *Mathematical and computer modelling*, 43(9-10):1172–1188, 2006.

[119] Zheng Chen, Xing Shu, Xiaoyu Li, Renxin Xiao, and Jiangwei Shen. Lifepo4 battery charging strategy design considering temperature rise minimization. *Journal of Renewable and Sustainable Energy*, 9(6):064103, 2017.

[120] Scott J Moura, Joel C Forman, Saeid Bashash, Jeffrey L Stein, and Hosam K Fathy. Optimal control of film growth in lithium-ion battery packs via relay switches. *IEEE Transactions on Industrial Electronics*, 58(8):3555–3566, 2010.

[121] Saeid Bashash, Scott J Moura, Joel C Forman, and Hosam K Fathy. Plug-in hybrid electric vehicle charge pattern optimization for energy cost and battery longevity. *Journal of power sources*, 196(1):541–549, 2011.

[122] Abdullah-Al Mamun, Iyswarya Narayanan, Di Wang, Anand Sivasubramaniam, and Hosam K Fathy. Multi-objective optimization to minimize battery degradation and electricity cost for demand response in datacenters. In *ASME 2015 Dynamic Systems and Control Conference*. American Society of Mechanical Engineers Digital Collection, 2015.

[123] Hector Perez, Niloofar Shahmohammadhamedani, and Scott Moura. Enhanced performance of li-ion batteries via modified reference governors and electrochemical models. *IEEE/ASME Transactions on Mechatronics*, 20(4):1511–1520, 2015.

[124] Divya Garg, William W Hager, and Anil V Rao. Pseudospectral methods for solving infinite-horizon optimal control problems. *Automatica*, 47(4):829–837, 2011.

[125] Ravi Methekar, Venkatasailanathan Ramadesigan, Richard D Braatz, and Venkat R Subramanian. Optimum charging profile for lithium-ion batteries to maximize energy storage and utilization. *ECS Transactions*, 25(35):139, 2010.

[126] Fariba Fahroo and I Michael Ross. Costate estimation by a legendre pseudospectral method. *Journal of Guidance, Control, and Dynamics*, 24(2):270–277, 2001.

[127] Ernesto Inoa and Jin Wang. Phev charging strategies for maximized energy saving. *IEEE Transactions on Vehicular Technology*, 60(7):2978–2986, 2011.

[128] Kristen A Severson, Peter M Attia, Norman Jin, Nicholas Perkins, Benben Jiang, Zi Yang, Michael H Chen, Muratahan Aykol, Patrick K Herring, Dimitrios Fraggedakis, et al. Data-driven prediction of battery cycle life before capacity degradation. *Nature Energy*, 4(5):383–391, 2019.

[129] M Foad Samadi and Mehrdad Saif. Nonlinear model predictive control for cell balancing in li-ion battery packs. In *2014 American Control Conference*, pages 2924–2929. IEEE, 2014.

[130] Paris Ali Topan, M Nisvo Ramadan, Ghufron Fathoni, Adha Imam Cahyadi, and Oyas Wahyunggoro. State of charge (soc) and state of health (soh) estimation on lithium polymer battery via kalman filter. In *2016 2nd International Conference on Science and Technology-Computer (ICST)*, pages 93–96. IEEE, 2016.

[131] Hongwen He, Rui Xiong, and Jinxin Fan. Evaluation of lithium-ion battery equivalent circuit models for state of charge estimation by an experimental approach. *energies*, 4(4):582–598, 2011.

[132] Ala A Hussein. Derivation and comparison of open-loop and closed-loop neural network battery state-of-charge estimators. *Energy Procedia*, 75:1856–1861, 2015.

[133] Satadru Dey, Beshah Ayalew, and Pierluigi Pisu. Nonlinear robust observers for state-of-charge estimation of lithium-ion cells based on a reduced electrochemical model. *IEEE Transactions on Control Systems Technology*, 23(5):1935–1942, 2015.

[134] Xiaosong Hu, Fengchun Sun, and Yuan Zou. Estimation of state of charge of a lithium-ion battery pack for electric vehicles using an adaptive luenberger observer. *Energies*, 3(9):1586–1603, 2010.

[135] Leobardo Camacho-Solorio, Miroslav Krstic, Reinhardt Klein, Anahita Mirtabatabaei, and Scott J Moura. State estimation for an electrochemical model of multiple-material lithium-ion batteries. In *Dynamic Systems and Control Conference*, volume 50695, page V001T08A004. American Society of Mechanical Engineers, 2016.

[136] Xidong Tang, Xiaofeng Mao, Jian Lin, and Brian Koch. Li-ion battery parameter estimation for state of charge. In *Proceedings of the 2011 American control conference*, pages 941–946. IEEE, 2011.

[137] Changfu Zou, Chris Manzie, Dragan Nešić, and Abhijit G Kallapur. Multi-time-scale observer design for state-of-charge and state-of-health of a lithium-ion battery. *Journal of Power Sources*, 335:121–130, 2016.

[138] Shriram Santhanagopalan and Ralph E White. State of charge estimation using an unscented filter for high power lithium ion cells. *International Journal of Energy Research*, 34(2):152–163, 2010.

[139] Zheng Chen, Yuhong Fu, and Chunting Chris Mi. State of charge estimation of lithium-ion batteries in electric drive vehicles using extended kalman filtering. *IEEE Transactions on Vehicular Technology*, 62(3):1020–1030, 2012.

[140] Zheng Chen, Xiaoyu Li, Jiangwei Shen, Wensheng Yan, and Renxin Xiao. A novel state of charge estimation algorithm for lithium-ion battery packs of electric vehicles. *Energies*, 9(9):710, 2016.

[141] Scott J Moura, Nalin A Chaturvedi, and Miroslav Krstić. Adaptive partial differential equation observer for battery state-of-charge/state-of-health estimation via an electrochemical model. *Journal of Dynamic Systems, Measurement, and Control*, 136(1), 2014.

[142] Satadru Dey, Sara Mohon, Pierluigi Pisu, Beshah Ayalew, and Simona Onori. Online state and parameter estimation of battery-double layer capacitor hybrid energy storage system. In *2015 54th IEEE Conference on Decision and Control (CDC)*, pages 676–681. IEEE, 2015.

[143] Rui Xiong, Fengchun Sun, Xianzhi Gong, and Chenchen Gao. A data-driven based adaptive state of charge estimator of lithium-ion polymer battery used in electric vehicles. *Applied Energy*, 113:1421–1433, 2014.

[144] Matthias Rausch, Reinhardt Klein, Stefan Streif, Christian Pankiewitz, and Rolf Findeisen. Set-based state of charge estimation for lithium-ion batteries. In *2014 American Control Conference*, pages 1566–1571. IEEE, 2014.

[145] Bharatkumar Suthar, Venkatasailanathan Ramadesigan, Paul WC Northrop, Bhushan Gopaluni, Shriram Santhanagopalan, Richard D Braatz, and Venkat R Subramanian. Optimal control and state estimation of lithium-ion batteries using reformulated models. In *2013 American Control Conference*, pages 5350–5355. IEEE, 2013.

[146] Patrick Frost, Patricia M Laskowsky, and Brian J Koch. Battery state estimator combining electrochemical solid-state concentration model with empirical equivalent-circuit model, June 28 2016. US Patent 9,377,512.

[147] Thomas F Fuller, Marc Doyle, and John Newman. Simulation and optimization of the dual lithium ion insertion cell. *Journal of the Electrochemical Society*, 141(1):1, 1994.

[148] Saeed Khaleghi Rahimian, Sean Rayman, and Ralph E White. Extension of physics-based single particle model for higher charge–discharge rates. *Journal of Power Sources*, 224:180–194, 2013.

[149] Nima Lotfi, Jie Li, Robert G Landers, and Jonghyun Park. Li-ion battery state of health estimation based on an improved single particle model. In *2017 American Control Conference (ACC)*, pages 86–91. IEEE, 2017.

[150] Xuebing Han, Minggao Ouyang, Languang Lu, and Jianqiu Li. Simplification of physics-based electrochemical model for lithium ion battery on electric vehicle. part ii: Pseudo-two-dimensional model simplification and state of charge estimation. *Journal of Power Sources*, 278:814–825, 2015.

[151] Kirk D Stetzel, Lukas L Aldrich, M Scott Trimboli, and Gregory L Plett. Electrochemical state and internal variables estimation using a reduced-order physics-based model of a lithium-ion cell and an extended kalman filter. *Journal of Power Sources*, 278:490–505, 2015.

[152] Xuebing Han, Minggao Ouyang, Languang Lu, and Jianqiu Li. Simplification of physics-based electrochemical model for lithium ion battery on electric vehicle. part i: Diffusion simplification and single particle model. *Journal of Power Sources*, 278:802–813, 2015.

[153] Isaiah Oyewole, Kyoung Hyun Kwak, Youngki Kim, and Xianke Lin. Optimal discretization approach to the enhanced single particle model for li-ion batteries. *IEEE Transactions on Transportation Electrification*, 2020.

[154] Venkatasailanathan Ramadesigan, Paul WC Northrop, Sumitava De, Shriram Santhanagopalan, Richard D Braatz, and Venkat R Subramanian. Modeling and simulation of lithium-ion batteries from a systems engineering perspective. *Journal of the electrochemical society*, 159(3):R31, 2012.

[155] Joel C Forman, Scott J Moura, Jeffrey L Stein, and Hosam K Fathy. Genetic identification and fisher identifiability analysis of the doyle–fuller–newman model

from experimental cycling of a lifepo4 cell. *Journal of Power Sources*, 210:263–275, 2012.

[156] LHJ Raijmakers, DL Danilov, R-A Eichel, and PHL Notten. A review on various temperature-indication methods for li-ion batteries. *Applied energy*, 240:918–945, 2019.

[157] Elke Schuster, Carlos Ziebert, Andreas Melcher, Magnus Rohde, and Hans Jürgen Seifert. Thermal behavior and electrochemical heat generation in a commercial 40 ah lithium ion pouch cell. *Journal of Power Sources*, 286:580–589, 2015.

[158] C Heubner, M Schneider, C Lämmel, and A Michaelis. Local heat generation in a single stack lithium ion battery cell. *Electrochimica Acta*, 186:404–412, 2015.

[159] D Danilov and PHL Notten. Mathematical modelling of ionic transport in the electrolyte of li-ion batteries. *Electrochimica Acta*, 53(17):5569–5578, 2008.

[160] Davide Grazioli, Marco Magri, and Alberto Salvadori. Computational modeling of li-ion batteries. *Computational Mechanics*, 58(6):889–909, 2016.

[161] D Andre, M Meiler, K Steiner, Ch Wimmer, T Soczka-Guth, and DU Sauer. Characterization of high-power lithium-ion batteries by electrochemical impedance spectroscopy. i. experimental investigation. *Journal of Power Sources*, 196(12):5334–5341, 2011.

[162] Allen Pei, Guangyuan Zheng, Feifei Shi, Yuzhang Li, and Yi Cui. Nanoscale nucleation and growth of electrodeposited lithium metal. *Nano letters*, 17(2):1132–1139, 2017.

[163] Aniruddha Jana and R Edwin García. Lithium dendrite growth mechanisms in liquid electrolytes. *Nano Energy*, 41:552–565, 2017.

[164] David S Eastwood, Paul M Bayley, Hee Jung Chang, Oluwadamilola O Taiwo, Joan Vila-Comamala, Daniel JL Brett, Christoph Rau, Philip J Withers, Paul R

Shearing, Clare P Grey, et al. Three-dimensional characterization of electrodeposited lithium microstructures using synchrotron x-ray phase contrast imaging. *Chemical communications*, 51(2):266–268, 2015.

[165] Dongsheng Ren, Kandler Smith, Dongxu Guo, Xuebing Han, Xuning Feng, Languang Lu, Minggao Ouyang, and Jianqiu Li. Investigation of lithium plating-stripping process in li-ion batteries at low temperature using an electrochemical model. *Journal of The Electrochemical Society*, 165(10):A2167, 2018.

[166] Owen Crowther and Alan C West. Effect of electrolyte composition on lithium dendrite growth. *Journal of the Electrochemical Society*, 155(11):A806, 2008.

[167] Cheng Lin, Aihua Tang, Ningning Wu, and Jilei Xing. Electrochemical and mechanical failure of graphite-based anode materials in li-ion batteries for electric vehicles. *Journal of Chemistry*, 2016, 2016.

[168] Noman Iqbal and Seungjun Lee. Mechanical failure analysis of graphite anode particles with pvdf binders in li-ion batteries. *Journal of The Electrochemical Society*, 165(9):A1961, 2018.

[169] Pengfei Yan, Jianming Zheng, Meng Gu, Jie Xiao, Ji-Guang Zhang, and Chong-Min Wang. Intragranular cracking as a critical barrier for high-voltage usage of layer-structured cathode for lithium-ion batteries. *Nature communications*, 8(1):1–9, 2017.

[170] Sihao Xia, Linqin Mu, Zhengrui Xu, Junyang Wang, Chenxi Wei, Lei Liu, Piero Pianetta, Kejie Zhao, Xiqian Yu, Feng Lin, et al. Chemomechanical interplay of layered cathode materials undergoing fast charging in lithium batteries. *Nano energy*, 53:753–762, 2018.

[171] William H Woodford, Yet-Ming Chiang, and W Craig Carter. "electrochemical shock" of intercalation electrodes: a fracture mechanics analysis. *Journal of the Electrochemical Society*, 157(10):A1052, 2010.

[172] Kejie Zhao, Matt Pharr, Joost J Vlassak, and Zhigang Suo. Fracture of electrodes in lithium-ion batteries caused by fast charging. *Journal of Applied Physics*, 108(7):073517, 2010.

[173] Sulin Zhang, Kejie Zhao, Ting Zhu, and Ju Li. Electrochemomechanical degradation of high-capacity battery electrode materials. *Progress in Materials Science*, 89:479–521, 2017.

[174] Amartya Mukhopadhyay and Brian W Sheldon. Deformation and stress in electrode materials for li-ion batteries. *Progress in Materials Science*, 63:58–116, 2014.

[175] Scott J Moura, Miroslav Krstic, and Nalin A Chaturvedi. Adaptive pde observer for battery soc/soh estimation. In *Dynamic Systems and Control Conference*, volume 45295, pages 101–110. American Society of Mechanical Engineers, 2012.

[176] Xin Zhou, Jeffrey L Stein, and Tulga Ersal. Battery state of health monitoring by estimation of the number of cyclable li-ions. *Control Engineering Practice*, 66:51–63, 2017.

[177] Satadru Dey, Beshah Ayalew, and Pierluigi Pisu. Combined estimation of state-of-charge and state-of-health of li-ion battery cells using smo on electrochemical model. In *2014 13th International Workshop on Variable Structure Systems (VSS)*, pages 1–6. IEEE, 2014.

[178] Githin K Prasad and Christopher D Rahn. Model based identification of aging parameters in lithium ion batteries. *Journal of power sources*, 232:79–85, 2013.

[179] Changfu Zou, Xiaosong Hu, Zhongbao Wei, Torsten Wik, and Bo Egardt. Electrochemical estimation and control for lithium-ion battery health-aware fast charging. *IEEE Transactions on Industrial Electronics*, 65(8):6635–6645, 2017.

[180] Perla B Balbuena and Yixuan Wang. *Lithium-ion batteries: solid-electrolyte interphase*. Imperial college press, 2004.

[181] Satu Kristiina Heiskanen, Jongjung Kim, and Brett L Lucht. Generation and evolution of the solid electrolyte interphase of lithium-ion batteries. *Joule*, 3(10):2322–2333, 2019.

[182] HH Lee, CC Wan, and YY Wang. Thermal stability of the solid electrolyte interface on carbon electrodes of lithium batteries. *Journal of The Electrochemical Society*, 151(4):A542, 2004.

[183] Guorong Zhuang, Yufeng Chen, and Philip N Ross. The reaction of lithium with dimethyl carbonate and diethyl carbonate in ultrahigh vacuum studied by x-ray photoemission spectroscopy. *Langmuir*, 15(4):1470–1479, 1999.

[184] Karim Zaghib, Gabrielle Nadeau, and Kimio Kinoshita. Effect of graphite particle size on irreversible capacity loss. *Journal of the Electrochemical Society*, 147(6):2110, 2000.

[185] Rachid Yazami and Yvan F Reynier. Mechanism of self-discharge in graphite–lithium anode. *Electrochimica Acta*, 47(8):1217–1223, 2002.

[186] Doron Aurbach, Yair Ein-Eli, Orit Chusid, Yaakov Carmeli, Matsliach Babai, and Herzel Yamin. The correlation between the surface chemistry and the performance of li-carbon intercalation anodes for rechargeable 'rocking-chair'type batteries. *Journal of The Electrochemical Society*, 141(3):603, 1994.

[187] JO Besenhard, Martin Winter, J Yang, and W Biberacher. Filming mechanism of lithium-carbon anodes in organic and inorganic electrolytes. *Journal of Power Sources*, 54(2):228–231, 1995.

[188] Ingrid Roten Mattson. Stability of the graphite electrode for li-ion batteries. Master's thesis, Institutt for materialteknologi, 2013.

[189] Dietrich Goers, Michael E Spahr, Antonio Leone, Wolfgang Märkle, and Petr Novák. The influence of the local current density on the electrochemical exfoliation of graphite in lithium-ion battery negative electrodes. *Electrochimica Acta*, 56(11):3799–3808, 2011.

[190] Michael E Spahr, Dietrich Goers, Wolfgang Märkle, Joseph Dentzer, Andreas Würsig, Hilmi Buqa, Cathie Vix-Guterl, and Petr Novák. Overpotentials and solid electrolyte interphase formation at porous graphite electrodes in mixed ethylene carbonate–propylene carbonate electrolyte systems. *Electrochimica acta*, 55(28):8928–8937, 2010.

[191] D Alliata, R Kötz, P Novák, and H Siegenthaler. Electrochemical spm investigation of the solid electrolyte interphase film formed on hopg electrodes. *Electrochemistry communications*, 2(6):436–440, 2000.

[192] Martin Winter, Petr Novák, and Alain Monnier. Graphites for lithium-ion cells: the correlation of the first-cycle charge loss with the brunauer-emmett-teller surface area. *Journal of the Electrochemical Society*, 145(2):428, 1998.

[193] Tao Zheng, Antoni S Gozdz, and Glenn G Amatucci. Reactivity of the solid electrolyte interface on carbon electrodes at elevated temperatures. *Journal of The Electrochemical Society*, 146(11):4014, 1999.

[194] Petr Novák, Joachim Ufheil, Hilmi Buqa, Frank Krumeich, Michael E Spahr, Dietrich Goers, Henri Wilhelm, Joseph Dentzer, Roger Gadiou, and Cathie Vix-Guterl. The importance of the active surface area of graphite materials in the first lithium intercalation. *Journal of power sources*, 174(2):1082–1085, 2007.

[195] SH Ng, C Vix-Guterl, Ph Bernardo, N Tran, J Ufheil, H Buqa, J Dentzer, R Gadiou, ME Spahr, D Goers, et al. Correlations between surface properties of graphite and the first cycle specific charge loss in lithium-ion batteries. *Carbon*, 47(3):705–712, 2009.

[196] Doron Aurbach, Mikhail D Levi, Elena Levi, and Alexander Schechter. Failure and stabilization mechanisms of graphite electrodes. *The Journal of Physical Chemistry B*, 101(12):2195–2206, 1997.

[197] Yair Ein-Eli, Boris Markovsky, Doron Aurbach, Yaakov Carmeli, Herzel Yamin, and Shalom Luski. The dependence of the performance of li-c intercalation an-

odes for li-ion secondary batteries on the electrolyte solution composition. *Electrochimica Acta*, 39(17):2559–2569, 1994.

[198] D Bar-Tow, E Peled, and L Burstein. A study of highly oriented pyrolytic graphite as a model for the graphite anode in li-ion batteries. *Journal of the Electrochemical Society*, 146(3):824, 1999.

[199] A Kominato, E Yasukawa, N Sato, T Ijuuin, H Asahina, and S Mori. Analysis of surface films on lithium in various organic electrolytes. *Journal of power sources*, 68(2):471–475, 1997.

[200] FP Campana, H Buqa, P Novak, R Kötz, and H Siegenthaler. In situ atomic force microscopy study of exfoliation phenomena on graphite basal planes. *Electrochemistry communications*, 10(10):1590–1593, 2008.

[201] Minoru Inaba, Yutaka Kawatate, Atsushi Funabiki, Soon-Ki Jeong, Takeshi Abe, and Zempachi Ogumi. Stm study on graphite/electrolyte interface in lithium-ion batteries: solid electrolyte interface formation in trifluoropropylene carbonate solution. *Electrochimica acta*, 45(1-2):99–105, 1999.

[202] QuanChao Zhuang, LeiLei Tian, GuoZhen Wei, QuanFeng Dong, and ShiGang Sun. Two-and three-electrode impedance spectroscopic studies of graphite electrode in the first lithiation. *Chinese Science Bulletin*, 54(15):2627–2632, 2009.

[203] MC Smart, BV Ratnakumar, S Surampudi, Y Wang, X Zhang, SG Greenbaum, A Hightower, CC Ahn, and B Fultz. Irreversible capacities of graphite in low-temperature electrolytes for lithium-ion batteries. *Journal of The Electrochemical Society*, 146(11):3963, 1999.

[204] Ernö Pretsch, Thomas Clerc, Joseph Seibl, and Wilhelm Simon. *Tables of spectral data for structure determination of organic compounds*. Springer Science & Business Media, 2013.

[205] Ken-ichi Morigaki and Akira Ohta. Analysis of the surface of lithium in organic electrolyte by atomic force microscopy, fourier transform infrared spectroscopy

and scanning auger electron microscopy. *Journal of power sources*, 76(2):159–166, 1998.

[206] Quan-Chao Zhuang, Jin-Mei Xu, Jing-Hua Tian, Xiao-Yong Fan, Quan-Feng Dong, and Shi-Gang Sun. Studies on graphite anode during electrochemical scan cycles by eis, raman spectroscopy and xrd. 2008.

[207] Eun-Gi Shim, Tae-Heum Nam, Jung-Gu Kim, Hyun-Soo Kim, and Seong-In Moon. Effects of functional electrolyte additives for li-ion batteries. *Journal of power sources*, 172(2):901–907, 2007.

[208] MN Richard and JR Dahn. Accelerating rate calorimetry study on the thermal stability of lithium intercalated graphite in electrolyte. ii. modeling the results and predicting differential scanning calorimeter curves. *Journal of The Electrochemical Society*, 146(6):2078, 1999.

[209] Hitoshi Ota, Tomohiro Sato, Hitoshi Suzuki, and Takao Usami. Tpd–gc/ms analysis of the solid electrolyte interface (sei) on a graphite anode in the propylene carbonate/ethylene sulfite electrolyte system for lithium batteries. *Journal of power sources*, 97:107–113, 2001.

[210] Thomas Waldmann, Björn-Ingo Hogg, and Margret Wohlfahrt-Mehrens. Li plating as unwanted side reaction in commercial li-ion cells–a review. *Journal of Power Sources*, 384:107–124, 2018.

[211] Meike Fleischhammer, Thomas Waldmann, Gunther Bisle, Björn-Ingo Hogg, and Margret Wohlfahrt-Mehrens. Interaction of cyclic ageing at high-rate and low temperatures and safety in lithium-ion batteries. *Journal of Power Sources*, 274:432–439, 2015.

[212] Pankaj Arora, Marc Doyle, and Ralph E White. Mathematical modeling of the lithium deposition overcharge reaction in lithium-ion batteries using carbon-based negative electrodes. *Journal of The Electrochemical Society*, 146(10):3543, 1999.

[213] Roger D Perkins, Alfred V Randall, Xiangchun Zhang, and Gregory L Plett. Controls oriented reduced order modeling of lithium deposition on overcharge. *Journal of Power Sources*, 209:318–325, 2012.

[214] Simon Hein and Arnulf Latz. Influence of local lithium metal deposition in 3d microstructures on local and global behavior of lithium-ion batteries. *Electrochimica Acta*, 201:354–365, 2016.

[215] Hao Ge, Tetsuya Aoki, Nobuhisa Ikeda, Sohei Suga, Takuma Isobe, Zhe Li, Yuichiro Tabuchi, and Jianbo Zhang. Investigating lithium plating in lithium-ion batteries at low temperatures using electrochemical model with nmr assisted parameterization. *Journal of The Electrochemical Society*, 164(6):A1050, 2017.

[216] Xiao-Guang Yang, Yongjun Leng, Guangsheng Zhang, Shanhai Ge, and Chao-Yang Wang. Modeling of lithium plating induced aging of lithium-ion batteries: Transition from linear to nonlinear aging. *Journal of Power Sources*, 360:28–40, 2017.

[217] Christian von Lüders, Jonas Keil, Markus Webersberger, and Andreas Jossen. Modeling of lithium plating and lithium stripping in lithium-ion batteries. *Journal of Power Sources*, 414:41–47, 2019.

[218] Yang-Tse Cheng and Mark W Verbrugge. Evolution of stress within a spherical insertion electrode particle under potentiostatic and galvanostatic operation. *Journal of Power Sources*, 190(2):453–460, 2009.

[219] S Prussin. Generation and distribution of dislocations by solute diffusion. *Journal of Applied Physics*, 32(10):1876–1881, 1961.

[220] James Chen-Min Li. Physical chemistry of some microstructural phenomena. *Metallurgical Transactions A*, 9(10):1353–1380, 1978.

[221] Sanboh Lee, WL Wang, and JR Chen. Diffusion-induced stresses in a hollow cylinder:: Constant surface stresses. *Materials Chemistry and Physics*, 64(2):123–130, 2000.

[222] Fuqian Yang and JCM Li. Diffusion-induced beam bending in hydrogen sensors. *Journal of Applied Physics*, 93(11):9304–9309, 2003.

[223] R Edwin Garcıa, Yet-Ming Chiang, W Craig Carter, Pimpa Limthongkul, and Catherine M Bishop. Microstructural modeling and design of rechargeable lithium-ion batteries. *Journal of The Electrochemical Society*, 152(1):A255, 2004.

[224] Xiangchun Zhang, Wei Shyy, and Ann Marie Sastry. Numerical simulation of intercalation-induced stress in li-ion battery electrode particles. *Journal of the Electrochemical Society*, 154(10):A910, 2007.

[225] Xiangchun Zhang, Ann Marie Sastry, and Wei Shyy. Intercalation-induced stress and heat generation within single lithium-ion battery cathode particles. *Journal of The Electrochemical Society*, 155(7):A542, 2008.

[226] Dong Zhang, Branko N Popov, and Ralph E White. Modeling lithium intercalation of a single spinel particle under potentiodynamic control. *Journal of the Electrochemical Society*, 147(3):831, 2000.

[227] John Christensen and John Newman. Stress generation and fracture in lithium insertion materials. *Journal of Solid State Electrochemistry*, 10(5):293–319, 2006.

[228] Mark Verbrugge and Yang-Tse Cheng. Stress distribution within spherical particles undergoing electrochemical insertion and extraction. *ECS Transactions*, 16(13):127, 2008.

[229] Jonghyun Park, Wei Lu, and Ann Marie Sastry. Numerical simulation of stress evolution in lithium manganese dioxide particles due to coupled phase transition and intercalation. *Journal of the Electrochemical Society*, 158(2):A201, 2010.

[230] Yue Qi, Haibo Guo, Louis G Hector Jr, and Adam Timmons. Threefold increase in the young's modulus of graphite negative electrode during lithium intercalation. *Journal of The Electrochemical Society*, 157(5):A558, 2010.

[231] Fuqian Yang. Insertion-induced breakage of materials. *Journal of Applied Physics*, 108(7):073536, 2010.

[232] Kenji Takahashi and Venkat Srinivasan. Examination of graphite particle cracking as a failure mode in lithium-ion batteries: a model-experimental study. *Journal of The Electrochemical Society*, 162(4):A635, 2015.

[233] John Wang, Justin Purewal, Ping Liu, Jocelyn Hicks-Garner, Souren Soukazian, Elena Sherman, Adam Sorenson, Luan Vu, Harshad Tataria, and Mark W Verbrugge. Degradation of lithium ion batteries employing graphite negatives and nickel–cobalt–manganese oxide+ spinel manganese oxide positives: Part 1, aging mechanisms and life estimation. *Journal of Power Sources*, 269:937–948, 2014.

[234] Scott J Moura, Federico Bribiesca Argomedo, Reinhardt Klein, Anahita Mirtabatabaei, and Miroslav Krstic. Battery state estimation for a single particle model with electrolyte dynamics. *IEEE Transactions on Control Systems Technology*, 25(2):453–468, 2016.

[235] M Safari and C Delacourt. Modeling of a commercial graphite/lifepo4 cell. *Journal of the Electrochemical Society*, 158(5):A562, 2011.

[236] Nalin A Chaturvedi, Reinhardt Klein, Jake Christensen, Jasim Ahmed, and Aleksandar Kojic. Modeling, estimation, and control challenges for lithium-ion batteries. In *Proceedings of the 2010 American Control Conference*, pages 1997–2002. IEEE, 2010.

[237] Nalin A Chaturvedi, Reinhardt Klein, Jake Christensen, Jasim Ahmed, and Aleksandar Kojic. Algorithms for advanced battery-management systems. *IEEE Control systems magazine*, 30(3):49–68, 2010.

[238] Guodong Fan and Marcello Canova. Model order reduction of electrochemical batteries using galerkin method. In *Dynamic Systems and Control Conference*, volume 57243, page V001T13A006. American Society of Mechanical Engineers, 2015.

[239] Robert Darling and John Newman. Modeling side reactions in composite li y mn2 o 4 electrodes. *Journal of The Electrochemical Society*, 145(3):990, 1998.

[240] Robert Spotnitz. Simulation of capacity fade in lithium-ion batteries. *Journal of power sources*, 113(1):72–80, 2003.

[241] Pankaj Arora, Ralph E White, and Marc Doyle. Capacity fade mechanisms and side reactions in lithium-ion batteries. *Journal of the Electrochemical Society*, 145(10):3647, 1998.

[242] Ramadass Premanand, Anand Durairajan, Bala Haran, Ralph White, and Branko Popov. Studies on capacity fade of spinel-based li-ion batteries. *Journal of the Electrochemical Society*, 149(1):A54, 2001.

[243] P Ramadass, Bala Haran, Ralph White, and Branko N Popov. Mathematical modeling of the capacity fade of li-ion cells. *Journal of power sources*, 123(2):230–240, 2003.

[244] P Ramadass, Bala Haran, Parthasarathy M Gomadam, Ralph White, and Branko N Popov. Development of first principles capacity fade model for li-ion cells. *Journal of the Electrochemical Society*, 151(2):A196, 2004.

[245] MD Levi, G Salitra, B Markovsky, H Teller, D Aurbach, Udo Heider, and Lilia Heider. Solid-state electrochemical kinetics of li-ion intercalation into li1-x coo2: simultaneous application of electroanalytical techniques sscv, pitt, and eis. *Journal of the Electrochemical Society*, 146(4):1279, 1999.

[246] AM Winter and SB Hanauer. Medical management of perianal crohn's disease. In *Seminars in Gastrointestinal Disease*, volume 9, pages 10–14, 1998.

[247] Pallavi Verma, Pascal Maire, and Petr Novák. A review of the features and analyses of the solid electrolyte interphase in li-ion batteries. *Electrochimica Acta*, 55(22):6332–6341, 2010.

[248] John Christensen and John Newman. A mathematical model of stress generation and fracture in lithium manganese oxide. *Journal of the Electrochemical Society*, 153(6):A1019, 2006.

[249] Jake Christensen. Modeling diffusion-induced stress in li-ion cells with porous electrodes. *Journal of the Electrochemical Society*, 157(3):A366, 2010.

[250] Sindhuja Renganathan, Godfrey Sikha, Shriram Santhanagopalan, and Ralph E White. Theoretical analysis of stresses in a lithium ion cell. *Journal of the Electrochemical Society*, 157(2):A155, 2009.

[251] Jici Wen, Yujie Wei, and Yang-Tse Cheng. Stress evolution in elastic-plastic electrodes during electrochemical processes: A numerical method and its applications. *Journal of the Mechanics and Physics of Solids*, 116:403–415, 2018.

[252] Stephen P Timoshenko and James M Gere. *Theory of elastic stability*. Courier Corporation, 2009.

[253] OH Basquin. The exponential law of endurance tests. In *Proc Am Soc Test Mater*, volume 10, pages 625–630, 1910.

[254] MA Miner et al. Cumulative fatigue damage. *Journal of applied mechanics*, 12(3):A159–A164, 1945.

[255] Kong Soon Ng, Chin-Sien Moo, Yi-Ping Chen, and Yao-Ching Hsieh. Enhanced coulomb counting method for estimating state-of-charge and state-of-health of lithium-ion batteries. *Applied energy*, 86(9):1506–1511, 2009.

[256] Jiuchun Jiang, Qiujiang Liu, Caiping Zhang, and Weige Zhang. Evaluation of acceptable charging current of power li-ion batteries based on polarization characteristics. *IEEE Transactions on Industrial Electronics*, 61(12):6844–6851, 2014.

[257] RC Van Dongen. Li-ion charger for implantable devices-selection of optimal charge algorithm and implementation. 2012.

[258] Rui Xiong, Quanqing Yu, Cheng Lin, et al. A novel method to obtain the open circuit voltage for the state of charge of lithium ion batteries in electric vehicles by using h infinity filter. *Applied energy*, 207:346–353, 2017.

[259] Yi-Hsien Chiang, Wu-Yang Sean, and Jia-Cheng Ke. Online estimation of internal resistance and open-circuit voltage of lithium-ion batteries in electric vehicles. *Journal of Power Sources*, 196(8):3921–3932, 2011.

[260] Ruixin Yang, Rui Xiong, Hongwen He, and Zeyu Chen. A fractional-order model-based battery external short circuit fault diagnosis approach for all-climate electric vehicles application. *Journal of cleaner production*, 187:950–959, 2018.

[261] Quanqing Yu, Rui Xiong, and Cheng Lin. Online estimation of state-of-charge based on the h infinity and unscented kalman filters for lithium ion batteries. *Energy Procedia*, 105:2791–2796, 2017.

[262] Daniyal Ali, Shayok Mukhopadhyay, and Habibur Rehman. A novel adaptive technique for li-ion battery model parameters estimation. In *2016 IEEE National Aerospace and Electronics Conference (NAECON) and Ohio Innovation Summit (OIS)*, pages 23–26. IEEE, 2016.

[263] Mohammad A Hannan, MS Hossain Lipu, Aini Hussain, and Azah Mohamed. A review of lithium-ion battery state of charge estimation and management system in electric vehicle applications: Challenges and recommendations. *Renewable and Sustainable Energy Reviews*, 78:834–854, 2017.

[264] Simon Schwunk, Nils Armbruster, Sebastian Straub, Johannes Kehl, and Matthias Vetter. Particle filter for state of charge and state of health estimation for lithium–iron phosphate batteries. *Journal of Power Sources*, 239:705–710, 2013.

[265] Zeyu Ma, Zhenpo Wang, Rui Xiong, and Jiuchun Jiang. A mechanism identification model based state-of-health diagnosis of lithium-ion batteries for energy storage applications. *Journal of Cleaner Production*, 193:379–390, 2018.

[266] Peter HL Notten, JHG Op het Veld, and JRG Van Beek. Boostcharging li-ion batteries: A challenging new charging concept. *Journal of Power Sources*, 145(1):89–94, 2005.

[267] Geoffrey Todd Huntington. *Advancement and analysis of a Gauss pseudospectral transcription for optimal control problems*. PhD thesis, Citeseer, 2007.

[268] Josef Stoer and Roland Bulirsch. *Introduction to numerical analysis*, volume 12. Springer Science & Business Media, 2013.

[269] Owe Axelsson. Global integration of differential equations through lobatto quadrature. *BIT Numerical Mathematics*, 4(2):69–86, 1964.

[270] Kailong Liu, Kang Li, Zhile Yang, Cheng Zhang, and Jing Deng. An advanced lithium-ion battery optimal charging strategy based on a coupled thermoelectric model. *Electrochimica Acta*, 225:330–344, 2017.

[271] Changfu Zou, Xiaosong Hu, Zhongbao Wei, and Xiaolin Tang. Electrothermal dynamics-conscious lithium-ion battery cell-level charging management via state-monitored predictive control. *Energy*, 141:250–259, 2017.

[272] Hector Eduardo Perez, Xiaosong Hu, Satadru Dey, and Scott J Moura. Optimal charging of li-ion batteries with coupled electro-thermal-aging dynamics. *IEEE Transactions on Vehicular Technology*, 66(9):7761–7770, 2017.

[273] Weiping Diao, Saurabh Saxena, and Michael Pecht. Accelerated cycle life testing and capacity degradation modeling of licoo2-graphite cells. *Journal of Power Sources*, 435:226830, 2019.

[274] Thomas Waldmann, Marcel Wilka, Michael Kasper, Meike Fleischhammer, and Margret Wohlfahrt-Mehrens. Temperature dependent ageing mechanisms in lithium-ion batteries–a post-mortem study. *Journal of Power Sources*, 262:129–135, 2014.

[275] Tomoyuki Matsuda, Masao Myojin, K Ando, and Daichi Imamura. Degradation analyses of commercial lithium-ion cells by temperature/c-rate controlled cycle test. *ECS Transactions*, 64(22):69, 2015.

[276] Shuai Ma, Modi Jiang, Peng Tao, Chengyi Song, Jianbo Wu, Jun Wang, Tao Deng, and Wen Shang. Temperature effect and thermal impact in lithium-ion batteries: A review. *Progress in Natural Science: Materials International*, 28(6):653–666, 2018.

[277] Sourav Pramanik and Sohel Anwar. Electrochemical model based charge optimization for lithium-ion batteries. *Journal of Power Sources*, 313:164–177, 2016.

[278] Xianke Lin, Xiaoguang Hao, Zhenyu Liu, and Weiqiang Jia. Health conscious fast charging of li-ion batteries via a single particle model with aging mechanisms. *Journal of Power Sources*, 400:305–316, 2018.

[279] HE Perez, S Dey, X Hu, and SJ Moura. Optimal charging of li-ion batteries via a single particle model with electrolyte and thermal dynamics. *Journal of The Electrochemical Society*, 164(7):A1679, 2017.

[280] Andrea Pozzi, Marcello Torchio, and Davide M Raimondo. Film growth minimization in a li-ion cell: a pseudo two dimensional model-based optimal charging approach. In *2018 European Control Conference (ECC)*, pages 1753–1758. IEEE, 2018.

[281] Yilin Yin and Song-Yul Choe. Actively temperature controlled health-aware fast charging method for lithium-ion battery using nonlinear model predictive control. *Applied Energy*, 271:115232, 2020.

[282] Subbarao Varigonda, Tryphon T Georgiou, and Prodromos Daoutidis. Numerical solution of the optimal periodic control problem using differential flatness. *IEEE Transactions on Automatic Control*, 49(2):271–275, 2004.

[283] Ji Liu, Guang Li, and Hosam K Fathy. Efficient lithium-ion battery model predictive control using differential flatness-based pseudospectral methods. In *Dynamic Systems and Control Conference*, volume 57243, page V001T13A005. American Society of Mechanical Engineers, 2015.

[284] Ji Liu. Computationally efficient online model-based control and estimation for lithium-ion batteries. 2017.

[285] Adrien Bizeray. *State and parameter estimation of physics-based lithium-ion battery models*. PhD thesis, University of Oxford, 2016.

[286] Adrien M Bizeray, Shi Zhao, Stephen R Duncan, and David A Howey. Lithium-ion battery thermal-electrochemical model-based state estimation using orthogonal collocation and a modified extended kalman filter. *Journal of Power Sources*, 296:400–412, 2015.

[287] Michel Fliess, Jean Lévine, Philippe Martin, and Pierre Rouchon. Flatness and defect of non-linear systems: introductory theory and examples. *International journal of control*, 61(6):1327–1361, 1995.

Appendices

Appendix A

Approximation of concentration profile and solid state diffusion

A.0.1 Concentration Profile Approximation

In this work, it is assumed that concentration in any electrode is only a function of time and radial periphery. The lithium ion concentration $c(r,t)$ can be approximated by a linear combination of Legendre polynomials and corresponding time variables.

$$c(r,t) \approx \phi_0(r)\beta_0(t) + \phi_2(r)\beta_2(t) + \phi_4(r)\beta_4(t) + \phi_6(r)\beta_6(t) = \sum_{i=0}^{4} \phi_i(r)\dot{\beta}_i(t) \quad \text{(A.1)}$$

where $\phi_i(r)$ are even Legendre polynomials and $\beta_i(t)$ represents the time dynamics of battery. The differential of even polynomials at collocation point is zero. Normalising of Legendre polynomials can be done such that:

$$\int_0^R \phi_i(r)\phi_j(r)dr = \begin{cases} 0 & \text{if} \quad i \neq j \\ 1 & \text{if} \quad i = j \end{cases}$$

where R is the radius of particle. The first four even Legendre polynomials used in this work are as follows:

$$\begin{aligned}
\phi_0(r) &= \sqrt{\frac{1}{R}} \\
\phi_2(r) &= \frac{1}{2}\sqrt{\frac{5}{R}}\left[3\frac{r^2}{R^2} - 1\right] \\
\phi_4(r) &= \frac{1}{8}\sqrt{\frac{9}{R}}\left[35\frac{r^4}{R^4} - 30\frac{r^2}{R^2} + 3\right] \\
\phi_6(r) &= \frac{1}{16}\sqrt{\frac{13}{R}}\left[231\frac{r^6}{R^6} - 315\frac{r^4}{R^4} + 105\frac{r^2}{R^2} - 5\right]
\end{aligned} \tag{A.2}$$

A.0.2 Approximation of solid state diffusion

The solid state diffusion is further solved using Legendre polynomials. The governing differential equation of Fick's second law of diffusion is:

$$\frac{\partial C(r,t)}{\partial t} = \frac{D}{r^2}\frac{\partial}{\partial r}\left(r^2\frac{\partial C(r,t)}{\partial r}\right) \tag{A.3}$$

$$\frac{\partial C(r,t)}{\partial t} = \frac{D}{r^2}\left(2r\ \frac{\partial C(r,t)}{\partial r} + r^2\ \frac{\partial^2 C(r,t)}{\partial r^2}\right)$$

$$\frac{\partial C(r,t)}{\partial t} = D\left(\frac{2}{r}\ \frac{\partial C(r,t)}{\partial r} + \frac{\partial^2 C(r,t)}{\partial r^2}\right) \tag{A.4}$$

where D is diffusion constant. Putting (A.1) in (A.4), we get different terms in form of Legendre polynomials and time variables.

$$\frac{\partial C(r,t)}{\partial t} = \phi_0(r)\dot{\beta}_0(t) + \phi_2(r)\dot{\beta}_2(t) + \phi_4(r)\dot{\beta}_4(t) + \phi_6(r)\dot{\beta}_6(t)$$

$$\begin{aligned}
\frac{\partial C(r,t)}{\partial r} &= \beta_0(t)\frac{d\phi_0(r)}{dr} + \beta_2(t)\frac{d\phi_2(r)}{dr} + \beta_4(t)\frac{d\phi_4(r)}{dr} + \beta_6(t)\frac{d\phi_6(r)}{dr} \\
\frac{\partial^2 C(r,t)}{\partial r^2} &= \beta_0(t)\frac{d\phi_0^2(r)}{dr^2} + \beta_2(t)\frac{d\phi_2^2(r)}{dr^2} + \beta_4(t)\frac{d\phi_4^2(r)}{dr^2} + \beta_6(t)\frac{d\phi_6^2(r)}{dr^2}
\end{aligned} \tag{A.5}$$

Computing differentials

$$\frac{d\phi_0(r)}{dr} = \frac{d\phi_0^2(r)}{dr^2} = 0$$

$$\frac{d\phi_2(r)}{dr} = \sqrt{\frac{5}{R}}\left[3\frac{r}{R^2}\right]$$

$$\frac{d\phi_2^2(r)}{dr^2} = \sqrt{\frac{5}{R}}\left[\frac{3}{R^2}\right]$$

$$\frac{d\phi_4(r)}{dr} = \frac{1}{8}\sqrt{\frac{9}{R}}\left[140\frac{r^3}{R^4} - 60\frac{r}{R^2}\right]$$

$$\frac{d\phi_4^2(r)}{dr^2} = \frac{1}{8}\sqrt{\frac{9}{R}}\left[420\frac{r^2}{R^4} - \frac{60}{R^2}\right]$$

$$\frac{d\phi_6(r)}{dr} = \frac{1}{16}\sqrt{\frac{13}{R}}\left[1386\frac{r^5}{R^6} - 1260\frac{r^3}{R^4} + 210\frac{r}{R^2}\right]$$

$$\frac{d\phi_6^2(r)}{dr^2} = \frac{1}{16}\sqrt{\frac{13}{R}}\left[6930\frac{r^5}{R^6} - 3780\frac{r^3}{R^4} + \frac{210}{R^2}\right]$$

Finally eq. (A.4) becomes:

$$\begin{bmatrix}\phi_0 & \phi_2 & \phi_4 & \phi_6\end{bmatrix}\begin{bmatrix}\dot{\beta}_0\\ \dot{\beta}_2\\ \dot{\beta}_4\\ \dot{\beta}_6\end{bmatrix} = \frac{2D}{r}\begin{bmatrix}\phi_0' & \phi_2' & \phi_4' & \phi_6'\end{bmatrix}\begin{bmatrix}\beta_0(t)\\ \beta_2(t)\\ \beta_4(t)\\ \beta_6(t)\end{bmatrix} + D\begin{bmatrix}\phi_0'' & \phi_2'' & \phi_4'' & \phi_6''\end{bmatrix}\begin{bmatrix}\beta_0(t)\\ \beta_2(t)\\ \beta_4(t)\\ \beta_6(t)\end{bmatrix} \tag{A.6}$$

To separate β terms from each other, it is important to take advantage of the orthonormal property of the Legendre polynomials. By applying Galerkin projections

$\int_0^R \phi_n(r)dr$ to above equation, the governing equation then becomes:

$$\begin{bmatrix} \int_0^R \phi_0\phi_0 dr & \int_0^R \phi_2\phi_0 dr & \int_0^R \phi_4\phi_0 dr & \int_0^R \phi_6\phi_0 dr \\ \int_0^R \phi_2\phi_0 dr & \int_0^R \phi_2\phi_2 dr & \int_0^R \phi_4\phi_2 dr & \int_0^R \phi_6\phi_2 dr \\ \int_0^R \phi_4\phi_0 dr & \int_0^R \phi_2\phi_4 dr & \int_0^R \phi_4\phi_4 dr & \int_0^R \phi_6\phi_4 dr \\ \int_0^R \phi_6\phi_0 dr & \int_0^R \phi_2\phi_6 dr & \int_0^R \phi_4\phi_6 dr & \int_0^R \phi_6\phi_6 dr \end{bmatrix} \begin{bmatrix} \dot{\beta}_0 \\ \dot{\beta}_2 \\ \dot{\beta}_4 \\ \dot{\beta}_6 \end{bmatrix}$$

$$\frac{2D}{r} \begin{bmatrix} \int_0^R \phi_0^{'}\phi_0 dr & \int_0^R \phi_2\phi_0^{'}\phi_0 dr & \int_0^R \phi_4\phi_0^{'}\phi_0 dr & \int_0^R \phi_6\phi_0^{'}\phi_0 dr \\ \int_0^R \phi_2\phi_0^{'}\phi_0 dr & \int_0^R \phi_2\phi_0^{'}\phi_2 dr & \int_0^R \phi_4\phi_0^{'}\phi_2 dr & \int_0^R \phi_6\phi_0^{'}\phi_2 dr \\ \int_0^R \phi_4\phi_0^{'}\phi_0 dr & \int_0^R \phi_2\phi_0^{'}\phi_4 dr & \int_0^R \phi_4\phi_0^{'}\phi_4 dr & \int_0^R \phi_6\phi_0^{'}\phi_4 dr \\ \int_0^R \phi_6\phi_0^{'}\phi_0 dr & \int_0^R \phi_2\phi_0^{'}\phi_6 dr & \int_0^R \phi_4\phi_0^{'}\phi_6 dr & \int_0^R \phi_6\phi_0^{'}\phi_6 dr \end{bmatrix} \begin{bmatrix} \beta_0(t) \\ \beta_2(t) \\ \beta_4(t) \\ \beta_6(t) \end{bmatrix}$$

$$+D \begin{bmatrix} \int_0^R \phi_0^{''}\phi_0 dr & \int_0^R \phi_2\phi_0^{''}\phi_0 dr & \int_0^R \phi_4\phi_0^{''}\phi_0 dr & \int_0^R \phi_6\phi_0^{''}\phi_0 dr \\ \int_0^R \phi_2\phi_0^{'}\phi_0 dr & \int_0^R \phi_2\phi_0^{''}\phi_2 dr & \int_0^R \phi_4\phi_0^{''}\phi_2 dr & \int_0^R \phi_6\phi_0^{''}\phi_2 dr \\ \int_0^R \phi_4\phi_0^{''}\phi_0 dr & \int_0^R \phi_2\phi_0^{''}\phi_4 dr & \int_0^R \phi_4\phi_0^{''}\phi_4 dr & \int_0^R \phi_6\phi_0^{''}\phi_4 dr \\ \int_0^R \phi_6\phi_0^{''}\phi_0 dr & \int_0^R \phi_2\phi_0^{''}\phi_6 dr & \int_0^R \phi_4\phi_0^{''}\phi_6 dr & \int_0^R \phi_6\phi_0^{''}\phi_6 dr \end{bmatrix} \begin{bmatrix} \beta_0(t) \\ \beta_2(t) \\ \beta_4(t) \\ \beta_6(t) \end{bmatrix} \tag{A.7}$$

where $\dot{\beta}_i$ is the derivative with respect to the time. After solving integrals, the diffusion dynamics can be expressed as:

$$\begin{bmatrix} \dot{\beta_0}(t) \\ \dot{\beta_2}(t) \\ \dot{\beta_4}(t) \\ \dot{\beta_6}(t) \end{bmatrix} = \frac{D_{s,n}}{R_n^2} \begin{bmatrix} 0 & 9\sqrt{5} & 20 & 29.4\sqrt{13} \\ 0 & 0 & 35\sqrt{5} & 16.8\sqrt{65} \\ 0 & 0 & 0 & 46.2\sqrt{13} \\ 0 & 0 & 0 & 0 \end{bmatrix} \begin{bmatrix} \beta_0(t) \\ \beta_2(t) \\ \beta_4(t) \\ \beta_6(t) \end{bmatrix} \tag{A.8}$$

Appendix B

State equations using pseudo-spectral method

The concentration at negative electrode can be approximated as:

$$c_n(r,t) = \beta_0(t_i)\phi_0(t_i) + \beta_2(t_i)\phi_2(t_i) + \beta_4(t_i)\phi_4(t_i) + \beta_6(t_i)\phi_6(t_i) \tag{B.1}$$

State of Charge in negative electrode $SOC_n = \frac{c_{n,avg}}{c_{max}}$ can be computed as:

$$SOC_n(t_i) = \frac{\beta_0(t_i)\phi_{0_{SOC}} + \beta_2(t_i)\phi_{2_{SOC}} + \beta_4(t_i)\phi_{4_{SOC}} + \beta_6(t_i)\phi_{6_{SOC}}}{c_{max}} \tag{B.2}$$

As we know that, from the state space model of negative electrode. $\beta_6(t_i)$ can be computed from algebraic equation.

$$\beta_6(t_i) = C(1,2)\beta_2(t_i) + C(1,3)\beta_4(t_i) + D(4,1)U(t_i) \tag{B.3}$$

where matrices C *and* D are obtained from state space model of negative electrode. so state of charge will be

$$SOC_n(t_i) = \frac{\beta_0(t_i)\phi_{0_{SOC}} + \beta_2(t_i)\phi_{2_{SOC}} + \beta_4(t_i)\phi_{4_{SOC}} + \Big(C(1,2)\beta_2(t_i) + C(1,3)\beta_4(t_i) + D(4,1)U(t_i)\Big)\phi_{6_{SOC}}}{c_{max}} \tag{B.4}$$

After simplifying the above equation, we get

$$SOC_n(t_i) = \frac{\beta_0(t_i)\phi_{0_{SOC}} + \beta_2(t_i)\Big(\phi_{2_{SOC}} + C(1,2)\phi_{6_{SOC}}\Big) + \beta_4(t_i)\Big(\phi_{4_{SOC}} + C(1,3)\phi_{6_{SOC}}\Big) + D(4,1)\phi_{6_{SOC}}U(t_i)}{c_{max}} \tag{B.5}$$

So Objective function (J) will be

$$J = \frac{t_f - t_0}{2} \sum_{i=1}^{N} w_i (SOC_n(t_i) - SOC_{ref})^2 \tag{B.6}$$

Now the discrete dynamic equations can be written in form as

$$X(t_i) = X(t_0) + \frac{t_f - t_0}{2} \sum_{k=1}^{N} A_{ik} \Big(A_n x_n + B_n U \Big) \tag{B.7}$$

As we know that there are three states in the system namely $\beta_0, \beta_4 and \beta_6$, so writing individually we have

$$\begin{aligned}
\beta_0(t_i) &= \beta_0(t_0) + \frac{t_f - t_0}{2} \sum_{k=1}^{N} A_{ik} \Big(A(1,2)\beta_2 + A(1,3)\beta_4 + B(1,1)U(t_i) \Big) \\
\beta_2(t_i) &= \beta_2(t_0) + \frac{t_f - t_0}{2} \sum_{k=1}^{N} A_{ik} \Big(A(2,2)\beta_2 + A(2,3)\beta_4 + B(2,1)U(t_i) \Big) \\
\beta_4(t_i) &= \beta_4(t_0) + \frac{t_f - t_0}{2} \sum_{k=1}^{N} A_{ik} \Big(A(3,2)\beta_2 + A(3,3)\beta_4 + B(3,1)U(t_i) \Big)
\end{aligned} \tag{B.8}$$

State of charge at surface of negative electrode will be computed as:

$$SOC_n^{surf}(t_i) = \frac{\beta_0(t_i)\phi_{0_{R_n}} + \beta_2(t_i)\phi_{2_{R_n}} + \beta_4(t_i)\phi_{4_{R_n}} + \beta_6(t_i)\phi_{6_{R_n}}}{c_{max}} \tag{B.9}$$

Eliminating $\beta_6(t_i)$ from the above equation, we get

$$SOC_n^{surf}(t_i) = \frac{\beta_0(t_i)\phi_{0_{R_n}} + \beta_2(t_i)\Big(\phi_{2_{R_n}} + C(1,2)\phi_{6_{R_n}}\Big) + \beta_4(t_i)\Big(\phi_{4_{R_n}} + C(1,3)\phi_{6_{R_n}}\Big) + D(4,1)\phi_{6_{R_n}} U(t_i)}{c_{max}} \tag{B.10}$$

Appendix C

State-space canonical form

Consider the system defined by

$$y^{(n)} + a_1 y^{(n-1)} + ... + a_{n-1}\dot{y} + a_n y = b_0 u^{(n)} + b_1 u^{(n-1)} + ... + b_{n-1}\dot{u} + b_n u \quad \text{(C.1)}$$

where u is the input, y is the output and $y^{(n)}$ represents the n^{th} derivative of y with respect to time. Taking the Laplace transform of both sides:

$$Y(s)\Big(s^n + a_1 s^{n-1} + ... + a_{n-1}s + a_n\Big) = U(s)\Big(b_0 s^n + b_1 s^{n-1} + ... + b_{n-1}s + b_n\Big) \quad \text{(C.2)}$$

which yields the transfer function:

$$\frac{Y(s)}{U(s)} = \frac{b_0 s^n + b_1 s^{n-1} + ... + b_{n-1}s + b_n}{s^n + a_1 s^{n-1} + ... + a_{n-1}s + a_n} \quad \text{(C.3)}$$

The controllable canonical form arranges the coefficient of the transfer function (C.3) is:

$$\begin{bmatrix} \dot{x_1} \\ \dot{x_2} \\ . \\ . \\ . \\ \dot{x_{n-1}} \\ \dot{x_n} \end{bmatrix} = \begin{bmatrix} 0 & 1 & 0 & ... & 0 \\ 0 & 0 & 1 & ... & 0 \\ . & . & . & ... & . \\ . & . & . & ... & . \\ . & . & . & ... & . \\ 0 & 0 & 0 & ... & 1 \\ -a_n & -a_{n-1} & -a_{n-2} & ... & -a_1 \end{bmatrix} \begin{bmatrix} x_1 \\ x_2 \\ . \\ . \\ . \\ x_{n-1} \\ x_n \end{bmatrix} + \begin{bmatrix} 0 \\ 0 \\ . \\ . \\ . \\ 0 \\ 1 \end{bmatrix} u \tag{C.4}$$

$$y = \begin{bmatrix} b_n & -a_n b_0 & b_{n-1} - a_{n-1} b_0 & ... & b_1 - a_1 b_0 \end{bmatrix} \begin{bmatrix} x_1 \\ x_2 \\ . \\ . \\ . \\ x_{n-1} \\ x_n \end{bmatrix} + b_0 u \tag{C.5}$$

Appendix D

Model Parameters: Single Particle Model (SPM)

Battery: A123 26650 lithium iron phosphate (LFP)

Capacity: 2.3 Ah

Table D.1: Parameters of single particle model

Parameter	Negative electrode	Positive electrode
L_j (μm)	70	34
A_j (cm^2)	1694	17554
R_j (nm)	36.5	3500
$c_{s,j,max}$ (mol/m^3)	22806	31370
$D_{s,j}$ (m^2/s)	1.26×10^{-15}	1.648×10^{-15}
k_j (A/m^2)	8.692×10^{-7}	1.127×10^{-7}
α_j	0.5	0.5
ϵ_j	0.35	0.45
c_e (mol/L)	1	
R_{cell} $(m\Omega)$	9	
F (C/mol)	96487	
R $(J/(mol.K))$	8.3143	
T $(^\circ C)$	25	

Appendix E

Model Parameters: Single Particle Model with Thermal Dynamics (SPM-T)

Battery: Lithium cobalt oxide (LCO)

Capacity: 2.2 Ah

Table E.1: Parameters of temperature-dependent single particle model

Parameter	Negative electrode	Positive electrode
$L_j\ (m)$	73.5×10^{-6}	25×10^{-6}
$A_j\ (m^2)$	0.0982	0.0982
$R_j\ (m)$	12.5×10^{-6}	8.5×10^{-6}
$c_{s,j,max}\ (mol/m^3)$	30556	51555
$D_{s,j}\ (m^2/s)$	3.9×10^{-14}	1×10^{-14}
$k_j\ (A/m^2)$	$1,764 \times 10^{-11}$	6.667×10^{-11}
α_j	0.5	0.5
ϵ_j	0.5052	0.55
$Ea_{D,j}\ (J/mol)$	35×10^3	29×10^3
$Ea_{k,j}\ (J/mol)$	20×10^3	58×10^3
$c_e\ (mol/L)$	1	
$R_{cell}\ (m\Omega)$	9	
$F\ (C/mol)$	96487	
$R\ (J/(mol.K))$	8.3143	
$T\ (^\circ C)$	25	
$C_p\ (J/kg/K)$	750	
$\rho\ (kg/m^3)$	1626	
$h\ (m)$	65×10^{-3}	
$D\ (m)$	18×10^{-3}	
$h_{conv}\ (W/m^2/K)$	30	
$T_{amb}\ (K)$	298	

Appendix F

Degradation Parameters

Table F.1: Degradation parameters

Chemical degradation: SEI layer parameters	
$i_{o,s}$ (A/m)	1.5×10^{-6}
M_p (mol/kg)	7.3×104
ρ_p	2.1×103
κ_p	1
Mechanical degradation: SEI layer parameters	
E_s (GPa)	0.5
R_s (μm)	9.2
ν_s	0.2
σ_{Yield} (MPa)	8
Mechanical degradation: Active material parameters	
E_p (GPa)	15
R_p (μm)	9
ν_p	9
Ω_p (cm^3/mol)	3.1

Appendix G

MATLAB Code

Included are the MATLAB scripts of open-circuit potentials, first derivative of Lagrange polynomial (D1) and second derivative Lagrange polynomial (D2).

G.1 SPM: Open circuit potentials

```
function [ Urefp ] = Urefp( SOC )
% Urefp=open circuit potential in the positive %electrode
SOCrefp = [0.992123152271639,0.961428477754598,0.930733803237556,...
0.900039128720515,0.869344454203473,0.838649779686431,....
    0.807955105169390,0.777260430652348,0.746565756135307,....
    0.715871081618265,0.685176407101224,0.654481732584182,....
    0.623787058067141,0.593092383550099,0.562397709033058,....
    0.531703034516016,0.501008359998975,0.470313685481933,....
    0.439619010964892,0.408924336447850,0.378229661930808,....
    0.347534987413767,0.316840312896725,0.286145638379684,....
    0.255450963862642,0.224756289345601,0.194061614828559,....
    0.163366940311518,0.132672265794476,0.101977591277435,....
    0.0712829167603931,0.0405882422433516,0.00989356772630998];
Uref = [-4.45876377749985,-3.66831953352692,-0.249129283851055,....
2.12174572567703,2.14057442441444,2.47159584100923,....
    3.34866246217808,3.34394608303872,3.34841168770438,....
```

```
    3.35160559328864,3.35963353313868,3.36747935020219,....
    3.37087521183173,3.38027849184923,3.38132996606247,....
    3.37120971375446,3.36875990967536,3.37675078056148,....
    3.38496704178736,3.38769666176123,3.39181276529228,....
    3.39258441568394,3.39293700770407,3.39183949519156,...
    3.41963690307998,3.42305805055184,3.42807483745323,....
    3.44312061856383,3.51335858528314,3.57598548554532,...
    3.67964435876334,4.17754313798878,5.14938199709510];
Urefp = interp1(SOCrefp,Uref,SOC);\\
end


function [ Urefn ] = Urefn( SOC )
%Urefn=open circuit potential in the negative %electrode
SOCrefn =[0.0100000000000000,0.0406250000000000,0.0712500000000000,....
0.101875000000000,0.132500000000000,0.163125000000000,....
    0.193750000000000,0.224375000000000,0.255000000000000,....
    0.285625000000000,0.316250000000000,0.346875000000000,....
    0.377500000000000,0.408125000000000,0.438750000000000,....
    0.469375000000000,0.500000000000000,0.530625000000000,...
    0.561250000000000,0.591875000000000,0.622500000000000,....
    0.653125000000000,0.683750000000000,0.714375000000000,....
    0.745000000000000,0.775625000000000,0.806250000000000,....
    0.836875000000000,0.867500000000000,0.898125000000000,....
    0.928750000000000,0.959375000000000,0.990000000000000];
Uref  =[1.08545544531486,0.348896890836803,0.203508306925828,....
0.192449482034197,0.178134272244356,0.159829937500000,....
    0.141525602755644,0.118336422190100,0.110667417078689,....
    0.106673690182914,0.106619993356594,0.106566296530274,....
    0.106512599703954,0.101157410858862,0.0913232791296414,....
    0.0782548670679943,0.0738254314152955,0.0732014526802732,....
```

```
    0.0725774739452509,0.0719534952102286,0.0713295164752063,....
    0.0707055377401840,0.0692147878050884,0.0661528160500216,....
    0.0630908442949547,0.0592502518124915,0.0538044692230235,....
    0.0483586866335556,0.0431912482875277,0.0380457437188909,....
    0.0329002391502540,0.0247550516862416,0.0111486952560682];
Urefn = interp1(SOCrefn,Uref,SOC);
end
```

G.2 SPM-T: Open circuit potentials

```
function [OCP1,OCP3]=openCircuitPotential(x1,x3)
%  This function computes the open-circuit  %potential

% INPUTS:
% x1     stoichiometry of anode active material.
% x3   stoichiometry of cathode active material.
%T              battery temperature.

% OUTPUTS:
% OCP1            anode open-circuit potential.

% OCP3            cathode open-circuit potential.


   % ANODE (Graphite - LiC6)

    $OCP1   =  0.7222 + 0.1387*x1 + 0.0290*x1.^(1/2) - 0.0172./x1 + ...
            0.0019./(x1.^(1.5)) + 0.2808*exp(0.90-15*x1) - ...
            0.7984*exp(0.4465*x1-0.4108);
```

```
   %CATHODE (Cobalt oxide - LiCoO2)

    OCP3   = ( -4.656 + 88.669*x3.^2 - 401.119*x3.^4 + 342.909*x3.^6 - ...
           462.471*x3.^8 + 433.434*x3.^10)./...
           ( -1 + 18.933*x3.^2 - 79.532*x3.^4 + 37.311*x3.^6 - ...
           73.083*x3.^8 + 95.96*x3.^10);

end
```

G.3 Differential Matrices (D, D1 and D2)

Matrix D can be obtained from [74]

```
function [Dd1,Dg1,Dbar1] = D1(n)
% Function generates the first derivatives of lagrange polynomials
%  Gauss Pts
[x, w] = gauss_points(n);
%  Add initial point -1
 x = [x; -1];
x = sort(x);
n = n+1;

for j = 1:n
    for i = 1:n
        prod = 1;

        sump=0;
```

```
sum = 0;


if j == i
    for k = 1:1:n-1
        if k~=i
            for kk=k+1:1:n
                if kk~=i
                    sum1 =1/(x(i)-x(k));
                    sum2= 1/(x(i)x(kk));
                    sum=sum+(sum1*sum2);
                end
            end


        end
    end
    D(i,j) = 2*sum;
else
for k = 1:1:n-1
    if (k~=i)&&(k~=j)
        for kk=k+1:n
            if (kk~=i)&&(kk~=j)
              sump=sump(x(i)x(k))*((x(i)x(kk)));
            end
        end
    end
end
for k = 1:n
    if k~=j
        prod = prod/(x(j)-x(k));
    end
end
```

```
        D(i,j) = 2*sump*prod;
        end
    end
end
Dd1=D;
Dg1 = D(2:end,2:end);
Dbar1= D(2:end,1);
x = x(2:end);

end



function [Dd2,Dg2,Dbar2] = D2(n)
% Function generates the 2nd derivatives of lagrange polynomials

% Gauss Pts
[x, w] = gauss_points(n);
% Add initial point -1
 x = [x; -1];
x = sort(x);
n = n+1;

for j = 1:n
    for i = 1:n
        prod = 1;
        prods=1;
        sump=0;
        sum = 0;

        if j == i
```

```
            for k = 1:1:n
                if k~=i


                      sum=sum+(x(i)-x(k));
                      prods=prods/(x(i)-x(k));
                end
            end
            D(i,j) = 6*sum*prods;
        else
        for k = 1:1:n
            if (k~=i)&&(k~=j)



                sump= sump+ (x(i)-x(k));



            end
        end
        for k = 1:n
            if k~=j
                prod = prod/(x(j)-x(k));
            end
        end
        D(i,j) = 6*sump*prod;
        end
    end
end
Dd2=D;
Dg2 = D(2:end,2:end);
Dbar2 = D(2:end,1);
x = x(2:end);
```

```
end
```

Complete code will be available from 30-08-2021 on the following link

https://github.com/Sajjad-Malik/Differential-Flatness-Method.git